Escuela de Ingeniería Industrial de Vigo

Departamento de Diseño en la Ingeniería

PROYECTO FIN DE CARRERA

INHOMOGENEITIES IN MATRICES WITH GRAIN STRUCTURE

Alumno

Helena Benito Campos

Director
Prof. Helmut J. Böhm

Viena, Febrero 2014

Abstract

The analytical and numerical modeling of the thermomechanical behavior of composite materials has become important over the past decades due to the application of such materials in many fields. The models typically assume that the different length scales present in the composite and its constituents are sufficiently well spread that sequential homogenization can be applied without problems.

The present master thesis focusses on a special, highly idealized case in which two such length scales are only weakly separated, a polycrystalline matrix reinforced by fibers of similar size to the matrix grains being studied. On the one hand, the effective elastic behavior is described by one-step models, which concurrently account for the inhomogeneities and the resolved grain structure of the matrix. On the other hand, two-step approaches are used, in which the matrix is homogenized first and the overall response of the composites is described by fibers embedded in the resulting effective matrix material. The grains are idealized as regular hexagons, the fibers being positioned in their centers or in the triple points. Five different types of elastic, fiber-like inhomogeneities are studied by unit cell models and, in addition, Hashin-Strikman bounds are evaluated.

The phase geometries are modeled and meshed with ABAQUS/CAE, random orientations of the grains are generated by a Python script, boundary conditions of the model and load-cases are obtained with the program package MedTool, and linear finite element simulations are performed with finite element program ABAQUS/Standard. Finally, the elasticity tensors and elastic moduli of all cases are evaluated with MedTool and analyzed, typically in terms of ensemble averages.

The results show that the relative differences between the single-step and two-step macroscopic elasticity tensors are smaller in the “normal part” of the elasticity tensor whereas larger differences are present in its “shear part”. Ranges of the von Mises

stresses and first principal stresses in fibers and matrix are considerably larger for one-step than for two-step homogenization. As to the Hashin-Strikman bounds, effective moduli evaluated in this work with the isotropized, homogenized matrix behavior either fall within the bounds or closely approach the lower or the upper bounds, for composited reinforced by stiff fibers or composites reinforced by inhomogeneities more compliant than the matrix, respectively. The closest transversally isotropic elasticity tensors obtained from the ensemble averages of the one-step and two-step results, however, in many cases do not fulfill the bounds. Taken together, the results show that sequential homogenization entails a loss of accuracy in situations where length scales are weakly spread.

Resumen

La importancia del modelado analítico y numérico del comportamiento termomecánico de materiales compuestos se ha incrementado a lo largo de las últimas décadas debido a la aplicación de estos materiales a diversos campos. Se asume normalmente en los modelos que las diferentes longitudes de escala presentes en el material compuesto y sus constituyentes están bien diferenciadas, por lo que la homogeneización periódica puede ser aplicada sin problemas.

El presente proyecto se centra en un caso especial y altamente idealizado en el cual dos longitudes de escala están débilmente diferenciadas: una matriz policristalina reforzada por fibras de tamaño similar a los granos de la matriz estudiada. Por una parte, el comportamiento elástico efectivo se describe por modelos de un sólo paso, que se aplica a las inhomogeneidades y la estructura granular de la matriz. Por otra parte, se usan aproximaciones en dos pasos, en las cuales la matriz es primero homogeneizada y la respuesta global de los materiales compuestos se describe por fibras embebidas en el resultante material efectivo de la matriz. Los granos se idealizan como hexágonos regulares, situándose las fibras en sus centros o en los puntos triples. Cinco tipos diferentes de inhomogeneidades elásticas se estudian por medio de modelos de celda unidad y, además, se evalúan los límites de Hashin-Strikman.

Las geometrías de fase se modelaron y mallaron con ABAQUS/CAE, las orientaciones aleatorias de los granos se generaron mediante un script en Python, las condiciones de contorno del modelo y las hipótesis de carga se obtuvieron con el programa MedTool, y las simulaciones lineales de elementos finitos se realizaron con el programa de elementos finitos ABAQUS/Standard. Finalmente, los tensores de elasticidad y módulos de elasticidad de todas las hipótesis se evaluaron con MedTool y se analizaron, normalmente en términos de las medias de conjuntos.

Los resultados muestran que las diferencias relativas entre los tensores de elasticidad macroscópicos en un solo paso y en dos pasos son menores en la “parte del esfuerzo

normal” del tensor de elasticidad mientras que están presentes mayores diferencias en la “parte de cortadura”. Los rangos de las tensiones de von Mises y primera tensión principal en las fibras y la matriz son considerablemente mayores para la homogeneización en un solo paso que para la misma en dos pasos. En cuanto a los límites de Hashin-Strikman, los módulos eficaces evaluados en este trabajo con el comportamiento isotropizado y homogeneizado de la matriz o bien caen dentro de los límites o bien se aproximan muy de cerca a los límites inferior o superior, para materiales compuestos reforzados por fibras rígidas o materiales compuestos reforzados con inhomogeneidades menos rígidas que la matriz, respectivamente. Los tensores de elasticidad más aproximados a elasticidad transversalmente isotrópica obtenidos de las medias de conjuntos de los resultados de homogeneización en un solo paso y en dos pasos, no satisfacen sin embargo los límites en muchos casos. Tomado en conjunto, los resultados muestran que la homogeneización periódica conlleva una pérdida de precisión en situaciones en que las longitudes de escala son similares.

Palabras Clave

Homogeneización periódica, método de los grados de libertad macroscópicos, elementos finitos, modelo celda unitaria, isotropización, materiales compuestos.

Acknowledgements

First of all I would like to thank my thesis advisor, Professor Helmut Böhm for his support and inestimable help during this work. This work would not have be finished without his assistance and guidance.

Realizar mi proyecto fin de Carrera en Viena ha sido sin duda una gran oportunidad y me gustaría por tanto agradecer a mi tutor el profesor José Antonio Pérez de la Universidad de Vigo por haberme dado esta oportunidad, así como al programa de intercambio Erasmus por hacerlo posible.

Por último quiero agradecer a mi madre, a mi tía y a mis amigos su apoyo durante esta difícil etapa y a lo largo de mis estudios.

Contents

Chapter 1
Introduction

1.1. Continuous Fiber Reinforced Composites

Composites are combinations of two or more different constituent materials (or phases), usually having a recognizable interface between them. Typical composites consist of one constituent that is topologically contiguous, which is referred to as the matrix, whereas the other constituents show an inclusion topology and are called reinforcements. Hence, composites are multiphase materials obtained by the combination of different materials in order to attain improved properties, which the individual components by themselves cannot attain.

The reinforcement phase typically comes in the form of fibers, particles or platelets and in most cases it is stiffer and stronger than the continuous matrix phase. Many types of reinforcements also have good thermal and electrical conductivities, coefficients of thermal expansion that are lower than that of the matrix, and/or good wear resistance [1]. Many natural and artificial materials may be viewed as composites, such as reinforced rubber, concrete or alloys.

Composite materials are commonly divided according to different classifications. Thus, based on the reinforcement geometry, composites can be classified as fiber (fibrous) composites, particulate composites, flake composites and filler/skeletal composites [2]. Fiber-reinforced composites are also commonly divided into continuous fiber and short fiber reinforced composites, the continuous fibers typically being aligned whereas short fibers often are not aligned. This classification of composites is shown in Figure 1.1.

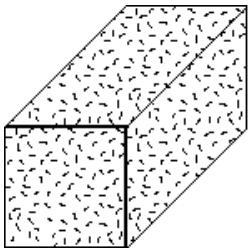

1) Random fiber (short fiber) reinforced composites

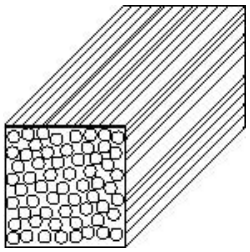

2) Continuous fiber (long fiber) reinforced composites

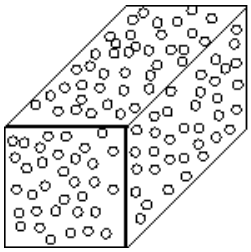

3) Particle reinforced composites (particulate composites)

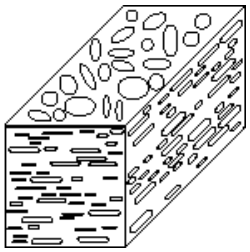

4) Composites reinforced by flat flakes (platelet composites)

Figure 1.1 Classification of composites with respect to the reinforcement geometry

The present report concentrates on fiber reinforced composites (FRC) and, in particular, on composites reinforced by continuous, aligned fibers. FRCs are widely used for application to diverse structures, such as aircraft, spacecraft, civil structures and automobile bodies. The embedding of strong, stiff fibers in parallel in a softer matrix material results in a fiber-reinforced composite with superior properties in the fiber direction, but the material properties perpendicular to the fiber direction are typically less favorable. Therefore, loading a continuously reinforced composite material perpendicularly to the fiber direction is to load it in the “soft” and weak direction the transverse direction. In addition, not all the loads are transmitted through the fiber in this case, but rather a portion of them is transmitted to the matrix material. Hence, stiffnesses and strengths transversal to the fiber direction are of the order of those of the matrix. Both the lower properties of the matrix and the poorer transverse properties of the fibers lead to poor properties of the composite in the directions perpendicular to the fibers [3], as shown in Figure 1.2 .

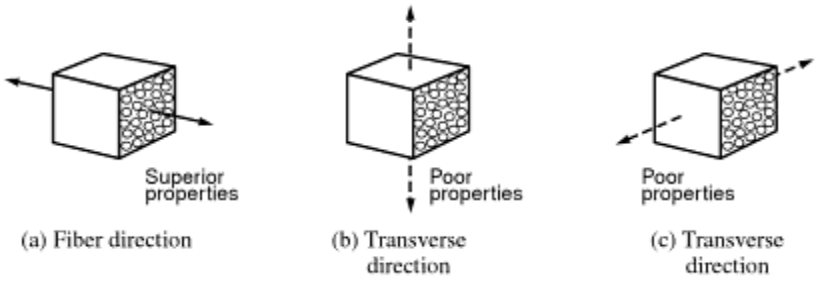

Figure 1.2 Poor transverse properties

Furthermore, the strength and stiffness properties of fiber-reinforced materials are limited by another important aspect: the strength of the composite depends critically upon the strength of the fiber-matrix interface, either in shear or in tension, see Figure 1.3. In spite of the poor transverse properties, however, the specific strength and the specific stiffness of composite materials are much greater than those of typical homogeneous materials. Hence, the structural weight required to provide a given level of strength and stiffness is reduced utilizing fiber reinforcement [4].

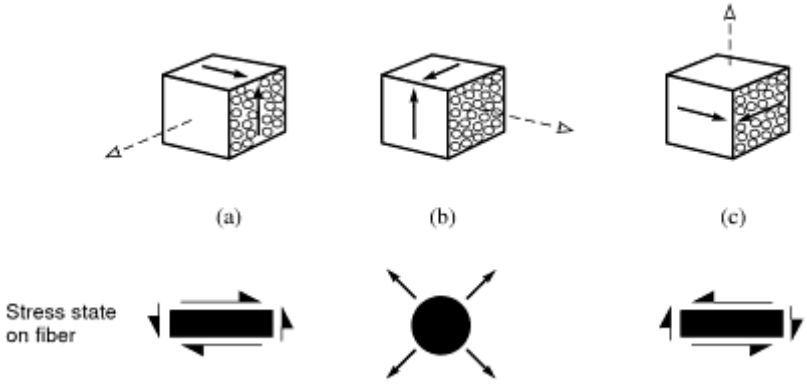

Figure 1.3 Poor shear properties

In the present work an idealized, fictitious continuous fiber reinforced composite is studied, the aim being to gain improved understanding of some technical aspects of micromechanical modeling of the elastic behavior of such materials.

1.2. General Considerations

The main tasks of micromechanical modeling are homogenization and localization. Homogenization is understood as estimating the behavior at some larger length scale by using information from a smaller length scale. Homogenization can provide microstructure-property relationships. Localization aims at deducing the local responses at the smaller length scale from the loading conditions on the larger length scale. In either case the main inputs are the geometrical arrangement and the material behaviors of the constituents at the smaller length scale.

It is important to mention that most micromechanical models are based on the assumption that the length scales in a given inhomogeneous material are well separated and that sequential homogenization in multi-scale settings requires the individual length scales to differ by at least an order of magnitude. However, in the present thesis, the matrix grains and the fibers of the modeled composites are purposely chosen to show similar length scales.

The concept of representative volume elements (RVEs), which are samples of a microstructure large enough to completely reflect the stochastic variations of material properties on the pertinent scale, forms the basis of most homogenization approaches. RVEs are used to deal with the fact that the microstructural configuration at individual levels is apparently disordered and does not comply with idealized geometries often found in the literature. It is necessary to define RVEs that are as small as possible in order to fit the requirements of computational practicality [5]. The use of RVEs implies that the composite to be modeled shows statistical homogeneity [3].

The present work is aimed at modeling composites reinforced by continuous, aligned fibers, which implies that the macroscopic elastic behavior is statistically transversely isotropic. Interfacial bonding between matrix and fibers is assumed to be perfect. Only elastic mechanical behavior is considered.

1.3. Scope of the present work

The purpose of the present work is to present an analysis of the macroscopic responses of highly idealized models of continuous fiber-reinforced composites in which the matrix is inhomogeneous, showing a grain structure with a length scale that is comparable to the fiber diameter and thus to the length scale of the reinforcements. The subject under consideration will be the analysis of the macroscopic (as well as selected microscopic) elastic responses obtained by periodic homogenization. One set of matrix properties will be combined with a range of inhomogeneity behaviors ranging from very stiff, anisotropic fibers to extremely compliant inhomogeneities that approach being aligned, cylindrical holes.

This task will be carried out using computational tools to analyze the elasticity tensors of suitable volume elements that are subjected to six linearly independent mechanical load cases. A total of five fictitious material combinations are studied, which use the same matrix. The individual matrix grains show cubic elastic symmetry, the material parameters approximating those of copper. As to the fibers, two sets of models describe transversally isotropic elastic responses similar to those of T-300 and P-100 carbon fibers. The three other data sets show isotropic elasticity, with one approximating Nextel 312 oxidic fibers and the other two describe fictitious behaviors that are more compliant than that of the matrix. Details of the material parameters used in the models are given in section3.6.

The modeling work is based on the Finite Element Method (FEM). The input of geometries and their meshing are carried out with the preprocessor ABAQUS/CAE 6.12 [6]. The random orientations of the matrix grains are generated by scripts in the Python programming language [7]. The periodicity boundary conditions for the volume elements are generated with the in-house code MedTool [8]. Analysis proper is carried out with the commercial FE code ABAQUS/Standard 6.12 [9]. For postprocessing the above programs ABAQUS/CAE and MedTool are used. 20 different sets of random material orientations at the grain level are considered, the results obtained from them being ensemble averaged.

After the introductory chapter, issues related to continuum micromechanics as a theoretical approach are presented in Chapter 2.

In Chapter 3, the modeling of the problem is presented in detail, as well as the means of its development.

Chapter 4 presents the results obtained from the analysis and their discussion.

Finally, a summary of the work done and conclusions to the thesis are presented in Chapter 5.

1.4. Relevant literature

Literature relevant to this thesis is presented in this section. Over the past 50 years a large body of literature on analytical and numerical models for describing the elastic behavior of composites in general and of continuously reinforced composites specifically has been published, which are not listed in detail here. An introduction to micromechanics of composite materials and to methods for their continuum mechanical analysis can be found in the report of Böhm [10], where also a number of relevant references are given.

To the author's knowledge there are no published works on the modeling of composites in which the matrix grains and the fibers show similar length scales.

Chapter 2
Theoretical Approach

2.1. Introduction

The following section has been extracted from the report written by Böhm [10], the main emphasis being put, on the one hand, on background information on continuum micromechanics and, on the other hand, on details of the approach used in the present work, periodic homogenization.

2.1.1. Inhomogeneous Materials

The behavior of inhomogeneous materials is determined, on the one hand, by the relevant material properties of the constituents and, on the other hand, by their geometry and topology (the "phase arrangement"). Obviously, the availability of information on these two counts determines the accuracy of any model or theoretical description.

An important aim of theoretical studies of multiphase materials lies in deducing their overall ("effective" or "apparent") behavior, from the corresponding material behavior of the constituents (and of the interfaces between them) and from the geometrical arrangement of the phases. The continuum methods discussed in the following are most suitable for handling scale transitions from length scales in the low micrometer range to macroscopic samples, components or structures with sizes of millimeters to meters.

The most basic classification criterion for inhomogeneous materials is based on the microscopic phase topology. In matrix–inclusion composites only the matrix shows a connected topology and the constituents play clearly distinct roles. In interpenetrating (interwoven) phase arrangements (as found, e.g., in open-cell foams or in some

functionally graded materials) and in typical polycrystals ("granular materials"), in contrast, the phases cannot be readily distinguished topologically.

Obviously, an important parameter in continuum micromechanics is the level of inhomogeneity of the constituents' behavior, which is often described by the phase contrast. For example, the elastic contrast of a two-phase composite takes the form

$$c_{el} = \frac{E^{(i)}}{E^{(m)}} \tag{2.1}$$

where E stands for the Young's modulus, (m) denotes the matrix and (i) the inhomogeneities (or reinforcement phase).

Length Scales

In the present context the lowest length scale described by a given micromechanical model is termed the microscale, the largest one the macroscale, and intermediate ones are called mesoscales. The fields describing the behavior of an inhomogeneous material, i.e., in mechanics the stresses $\boldsymbol{\sigma}(\mathbf{x})$, strains $\boldsymbol{\varepsilon}(\mathbf{x})$ and displacements $\mathbf{u}(\mathbf{x})$, are split into contributions corresponding to the different length scales, which are referred to as micro-, macro- and mesofields, respectively. The phase geometries on the meso- and microscales are denoted as meso- and microgeometries.

Most micromechanical models are based on the assumption that the length scales in a given material are well separated. This is understood to imply that for each micro-macro pair of scales, on the one hand, the fluctuating contributions to the fields at the smaller length scale ("fast variables") influence the behavior at the larger length scale only via their volume averages. On the other hand, gradients of the fields as well as compositional gradients at the larger length scale ("slow variables") are not significant at the smaller length scale, where these fields appear to be locally constant and can be described in terms of uniform "applied fields" or "far fields". Formally, this splitting of the strain and stress fields into slow and fast contributions can be written as

$$\boldsymbol{\varepsilon}(\mathbf{x}) = <\boldsymbol{\varepsilon}> + \boldsymbol{\varepsilon}'(\mathbf{x}) \qquad \text{and} \qquad \boldsymbol{\sigma}(\mathbf{x}) = <\boldsymbol{\sigma}> + \boldsymbol{\sigma}'(\mathbf{x}) \tag{2.2}$$

where $<\boldsymbol{\varepsilon}>$ and $<\boldsymbol{\sigma}>$ are the macroscopic (slow) fields, whereas $\boldsymbol{\varepsilon}'$ and $\boldsymbol{\sigma}'$ stand for the microscopic fluctuations.

In the present thesis, length scales are not as well separated as postulated in many micromechanical models, but the size of the matrix grains and the fibers' diameter are similar.

2.1.2. Homogenization

The "bridging of length scales", which constitutes the central issue of continuum micromechanics, involves two main tasks. On the one hand, the behavior at some larger length scale (the macroscale) must be estimated or bounded by using information from a smaller length scale (the microscale), i.e., homogenization or upscaling problems must be solved. Since homogenization links the phase arrangement at the microscale to the macroscopic behavior, it can provide microstructure–property relationships. On the other hand, the local responses at the smaller length scale may be deduced from the loading conditions on the larger length scale. This task is referred to as localization, downscaling or fine graining. In either case the main inputs are the geometrical arrangement and the material behaviors of the constituents at the microscale.

For a volume element Ω_s of an inhomogeneous material that is sufficiently large, contains no significant gradients of composition and shows no significant variations in the applied loads, homogenization relations take the form of volume averages of some variable $f(\mathbf{x})$,

$$<\boldsymbol{f}> = \frac{\mathbf{1}}{\boldsymbol{\Omega_s}} \int_{\Omega_s} \boldsymbol{f}(\mathbf{x}) \boldsymbol{d\Omega} \tag{2.3}$$

Accordingly, the homogenization relations for the stress and strain tensors can be given as

$$< \boldsymbol{\varepsilon} > = \frac{1}{\Omega s} \int_{\Omega s} \boldsymbol{\varepsilon}(\mathbf{x})\, d\,\Omega = \frac{1}{2\Omega s} \int_{\Gamma s} [\mathbf{u}(\mathbf{x}) \otimes \mathbf{n}_{\Gamma}(\mathbf{x}) + \mathbf{n}_{\Gamma}(\mathbf{x}) \otimes \mathbf{u}(\mathbf{x})]\, d\Gamma$$

$$< \boldsymbol{\sigma} > = \frac{1}{\Omega s} \int_{\Omega s} \boldsymbol{\sigma}(\mathbf{x})\, d\,\Omega = \frac{1}{2\Omega s} \int_{\Gamma s} \mathbf{t}(\mathbf{x}) \otimes \mathbf{x}\, d\Gamma, \qquad (2.4)$$

where Γs stands for surface of the volume element, **u**(**x**) is the deformation vector, **t**(**x**) =$\boldsymbol{\sigma}$(**x**) * $\mathbf{n}_{\Gamma}$(**x**) is the surface traction vector, and $\mathbf{n}_{\Gamma}$(**x**) is the surface normal vector. Equations (2.4) are known as the average strain and average stress theorems, and the surface integral formulation for $\boldsymbol{\varepsilon}$ given above pertains to the small strain regime and to continuous displacements. Under the latter condition the mean strains and stresses in a control volume, <$\boldsymbol{\varepsilon}$> and <$\boldsymbol{\sigma}$>, are fully determined by the surface displacements and tractions. In the absence of body forces the microstresses $\boldsymbol{\sigma}$(**x**) are self-equilibrated (but not necessarily zero). In the above form, eqn. (2.4) applies to linear elastic behavior.

The microscopic strain and stress fields, $\boldsymbol{\varepsilon}$(**x**) and $\boldsymbol{\sigma}$(**x**), in a given volume element Ωs are formally linked to the corresponding macroscopic responses, <$\boldsymbol{\varepsilon}$>and <$\boldsymbol{\sigma}$>, by localization (or projection) relations of the type

$$\boldsymbol{\varepsilon}(\mathbf{x}) = \mathbf{B}(\mathbf{x}) < \boldsymbol{\varepsilon} > \quad \text{and} \quad \boldsymbol{\sigma}(\mathbf{x}) = \mathbf{B}(\mathbf{x}) < \boldsymbol{\sigma} > \qquad (2.5)$$

A(**x**) and **B**(**x**) are known as mechanical strain and stress concentration tensors (or influence functions, see [11]), respectively. When they are known, localization tasks can be carried out.

2.1.3. Volume Elements

The microgeometries of real inhomogeneous materials are at least to some extent random and, in the majority of cases of practical relevance, their detailed phase arrangements are highly complex. As a consequence, exact expressions for **A**(**x**), **B**(**x**), $\boldsymbol{\varepsilon}$(**x**), $\boldsymbol{\sigma}$(**x**), etc., in general cannot be given with reasonable effort and approximations have to be introduced. Typically, these approximations are based on the ergodic hypothesis, i.e., the heterogeneous material is assumed to be statistically homogeneous. This implies that sufficiently large volume elements selected at random positions within

the sample have statistically equivalent phase arrangements and give rise to the same averaged material properties. Such material properties are referred to as the overall or effective material properties of the inhomogeneous material.

Ideally, the homogenization volume should be chosen to be a proper representative volume element (RVE), i.e., a subvolume of Ω_s that is of sufficient size to contain all information necessary for describing the behavior of the composite. Representative volume elements can be defined, on the one hand, by requiring them to be statistically representative of the microgeometry, the resulting "geometrical RVEs" being independent of the physical property to be studied. On the other hand, the definition can be based on the requirement that the overall responses with respect to some given physical behavior do not depend on the actual position and - in the case of macroscopic isotropy - orientation of the RVE nor on the boundary conditions applied to it [11].

An RVE must be sufficiently large to allow a meaningful sampling of the microfields and sufficiently small for the influence of macroscopic gradients to be negligible and for an analysis of the microfields to be possible.

The fields in a given constituent (p) can be split into phase averages and fluctuations by analogy to eqn. (2.2) as

$$\boldsymbol{\varepsilon}^{(p)}(\mathbf{x}) = \langle\boldsymbol{\varepsilon}\rangle^{(p)} + \boldsymbol{\varepsilon}^{(p)\prime}(\mathbf{x}) \quad \text{and} \quad \boldsymbol{\sigma}^{(p)}(\mathbf{x}) = \langle\boldsymbol{\sigma}\rangle^{(p)} + \boldsymbol{\sigma}^{(p)\prime}(\mathbf{x}) \tag{2.6}$$

In the case of materials with matrix–inclusion topology, i.e., for typical composites, analogous relations can be also be defined at the level of individual inhomogeneities. The variations of the (average) fields between individual particles or fibers are known as inter-particle or inter-fiber fluctuations, respectively, whereas field gradients within given inhomogeneities give rise to intra-particle and intra-fiber fluctuations.

Needless to say, volume elements should be chosen to be as simple possible in order to limit the modeling effort, but their level of complexity must be sufficient for covering the aspects of their behavior targeted by a given study, compare, e.g., the examples given by [12].

2.1.4. Overall Behavior, Material Symmetries

The homogenized strain and stress fields of an elastic inhomogeneous material as obtained by eqn. (2.4), can be linked by effective elastic tensors **E*** and **C*** as

$$\langle \boldsymbol{\sigma} \rangle = \mathbf{E}^* \langle \boldsymbol{\varepsilon} \rangle \quad \text{and} \quad \langle \boldsymbol{\varepsilon} \rangle = \mathbf{C}^* \langle \boldsymbol{\sigma} \rangle \tag{2.7}$$

which may be viewed as the elasticity and compliance tensors, respectively, of an appropriate equivalent homogeneous material, with $C^* = E^{*-1}$. Using eqns. (2.4) and (2.5) these effective elastic tensors can be obtained from the local elastic tensors, $\mathbf{E}(\mathbf{x})$ and $\mathbf{C}(\mathbf{x})$, and the concentration tensors, $\mathbf{A}(\mathbf{x})$ and $\mathbf{B}(\mathbf{x})$, as volume averages

$$\mathbf{E}^* = \frac{1}{\Omega s}\int_{\Omega s} \mathbf{E}(\mathbf{x})\mathbf{A}(\mathbf{x})\mathrm{d}\Omega$$

$$\mathbf{C}^* = \frac{1}{\Omega s}\int_{\Omega s} \mathbf{C}(\mathbf{x})\mathbf{B}(\mathbf{x})\mathrm{d}\Omega \tag{2.8}$$

The resulting homogenized behavior of many multi-phase materials can be idealized as being statistically isotropic, quasi-isotropic or statistically transversely isotropic (e.g., for composites reinforced with aligned fibers or platelets) [13].

Statistically isotropic multi-phase materials show the same overall behavior in all directions, and their effective elasticity tensors and thermal expansion tensors take the forms

$$\mathbf{E} = \begin{pmatrix} E_{11} & E_{12} & E_{12} & 0 & 0 & 0 \\ E_{12} & E_{11} & E_{12} & 0 & 0 & 0 \\ E_{12} & E_{12} & E_{11} & 0 & 0 & 0 \\ 0 & 0 & 0 & E_{44} & 0 & 0 \\ 0 & 0 & 0 & 0 & E_{44} & 0 \\ 0 & 0 & 0 & 0 & 0 & E_{44} = \frac{1}{2}(E_{11}E_{12}) \end{pmatrix} \qquad \boldsymbol{\alpha} = \begin{pmatrix} \alpha \\ \alpha \\ \alpha \\ 0 \\ 0 \\ 0 \end{pmatrix} \tag{2.9}$$

in Voigt/Nye notation. Two independent parameters are sufficient for describing isotropic overall linear elastic behavior (e.g., the effective Young's modulus $E^* = E^*_{11} - 2E^{*2}_{12} / (E^*_{11} + E^*_{12})$, the effective Poisson number $\nu^* = E^*_{12}/ (E^*_{11} + E^*_{12})$, the effective shear modulus $G^* = E^* /2 (1 + \nu^*)$, the effective bulk modulus $K^* = (E^*_{11} + 2E^*_{12})/ 3 = E^*/(3(1-2\nu^*))$, or the effective Lamé constants) and one is required for the

effective thermal expansion behavior in the linear range (the effective coefficient of thermal expansion $\alpha^* = \alpha^*_{11}$.

The effective elasticity and thermal expansion tensors for statistically transversely isotropic materials have the structure

$$\mathbf{E} = \begin{pmatrix} E_{11} & E_{12} & E_{12} & 0 & 0 & 0 \\ E_{12} & E_{22} & E_{23} & 0 & 0 & 0 \\ E_{12} & E_{23} & E_{22} & 0 & 0 & 0 \\ 0 & 0 & 0 & E_{44} & 0 & 0 \\ 0 & 0 & 0 & 0 & E_{44} & 0 \\ 0 & 0 & 0 & 0 & 0 & E_{66} = \frac{1}{2}(E_{22} - E_{23}) \end{pmatrix} \qquad \boldsymbol{\alpha} = \begin{pmatrix} \alpha_A \\ \alpha_T \\ \alpha_T \\ 0 \\ 0 \\ 0 \end{pmatrix} \tag{2.10}$$

where 1 is the axial direction and 2–3 is the transverse plane of isotropy. In the present thesis the definition of axis used is the one given by ABAQUS, where 1-2 is the transverse plane of isotropy and 3 the axial direction, as it is defined in section **3.6**. For more clarity, the elastic compliance tensor as used in the FE-code ABAQUS/Standard is given by

$$\begin{Bmatrix} \varepsilon_{11} \\ \varepsilon_{22} \\ \varepsilon_{33} \\ \gamma_{12} \\ \gamma_{13} \\ \gamma_{23} \end{Bmatrix} = \begin{bmatrix} 1/E_p & -\nu_p/E_p & -\nu_{tp}/E_t & 0 & 0 & 0 \\ -\nu_p/E_p & 1/E_p & -\nu_{tp}/E_t & 0 & 0 & 0 \\ -\nu_{pt}/E_p & -\nu_{pt}/E_p & 1/E_t & 0 & 0 & 0 \\ 0 & 0 & 0 & 1/G_p & 0 & 0 \\ 0 & 0 & 0 & 0 & 1/G_t & 0 \\ 0 & 0 & 0 & 0 & 0 & 1/G_t \end{bmatrix} \begin{Bmatrix} \sigma_{11} \\ \sigma_{22} \\ \sigma_{33} \\ \sigma_{12} \\ \sigma_{13} \\ \sigma_{23} \end{Bmatrix}$$

where $G_p = E_p / 2(1+ \nu_p)$. Transverse isotropy requires that $E_1 = E_2 = E_p$, $\nu_{31} = \nu_{32} = \nu_{tp}$, $\nu_{13} = \nu_{23} = \nu_{pt}$, and $G_{13} = G_{23} = G_t$, where *p* and *t* stand for "in-plane" and "transverse," respectively. Thus, while ν_{tp} has the physical interpretation of the Poisson's ratio that characterizes the strain in the plane of isotropy resulting from stress normal to it, ν_{pt} characterizes the transverse strain in the direction normal to the plane of isotropy resulting from stress in the plane of isotropy. In general, the quantities ν_{tp} and ν_{pt} are not equal and are related by $\nu_{tp}/E_t = \nu_{pt}/E_p$.

Appropriate elasticity parameters in this context are, e.g., the axial and transverse effective Young's moduli, $E^*_A = E^*_{11} - 2E_{12}^2 /(E_{22}+E_{23})$ and $E^*_T = E^*_{22} - (E^*_{11}E^*_{23}{}^2 + E^*_{22}E^*_{12}{}^2 - 2E^*_{23}E^*_{12}{}^2)/(E^*_{11}E^*_{22} - E^*_{12}{}^2)$, the axial and transverse effective shear moduli, $G^*_A = E^*_{44}$ and $G^*_T = E^*_{66}$, the axial and transverse effective Poisson numbers,

$v^*_A = E^*_{12}E^*_{22}+E^*_{23}$ and $v^*_T = E^*_{11}E^*_{23} - E^{*2}_{12}\ E^*_{11}E^*_{22} - E^{*2}_{12}$, as well as the effective transverse (plane strain) bulk modulus $K^*_T = (E^*_{22} + E^*_{23})/2 = E^*_A/2[(1 - v^*_T)(E^*_A/E^*_T) - 2v^{*2}_A]$. The transverse ("in-plane") properties are related via $G^*_T = E^*_T/2(1 + v^*_T)$, but there is no general linkage between the axial properties E^*_A, G^*_A and v^*_A beyond the above definition of K^*_T. For the special case of materials reinforced by aligned continuous fibers, however, the connections [14]

$$E_{\mathbb{A}} = \xi E_{\mathbb{A}}^{(f)} + (1-\xi)E^{(m)} + \frac{4(v_{\mathbb{A}}^{(f)} - v^{(m)})^2}{(1/K_{\mathbb{T}}^{(f)} - 1/K_{\mathbb{T}}^{(m)})^2}\left(\frac{\xi}{K_{\mathbb{T}}^{(f)}} + \frac{1-\xi}{K_{\mathbb{T}}^{(m)}} - \frac{1}{K_{\mathbb{T}}}\right)$$

$$v_{\mathbb{A}} = \xi v_{\mathbb{A}}^{(f)} + (1-\xi)v^{(m)} + \frac{v_{\mathbb{A}}^{(f)} - v^{(m)}}{1/K_{\mathbb{T}}^{(f)} - 1/K_{\mathbb{T}}^{(m)}}\left(\frac{\xi}{K_{\mathbb{T}}^{(f)}} + \frac{1-\xi}{K_{\mathbb{T}}^{(m)}} - \frac{1}{K_{\mathbb{T}}}\right) \qquad (2.11)$$

allow the effective moduli E^*_A and v^*_A to be expressed by K^*_T, some constituent properties, and the fiber volume fraction ξ; see also [15]. Equations (2.11)can be used for reducing the number of independent effective elastic parameters required for describing the behavior of unidirectional continuously reinforced composites to three.

The overall material symmetries of inhomogeneous materials and their effect on various physical properties can be treated in full analogy to the symmetries of crystals as discussed, e.g., by [16].

In many cases deviations of predicted elastic tensors from macroscopically isotropic elastic symmetry can be assessed via a Zener parameter, $Z = 2\ E^*_{11}/(E^*_{11} - E^*_{12})$.

The influence of the overall symmetry of the phase arrangement on the overall mechanical behavior of inhomogeneous materials can be marked.

2.1.5. Major Modeling Strategies in Continuum Micromechanics of Materials

All micromechanical methods can be used to carry out materials characterization, i.e., for simulating the overall material response under simple loading conditions such as uniaxial tensile tests.

Because for realistic phase distributions the analysis of the spatial variations of the microfields in sufficiently large volume elements tends to be beyond present capabilities, approximations have to be used. For convenience, the majority of the resulting modeling approaches may be treated as falling into two groups. The first of these comprises methods that describe interactions, e.g., between phases or between individual reinforcements, in a collective way in terms of phase-wise uniform fields and comprises

- Mean Field Approaches (MFAs) and related methods: The microfields within each constituent of an inhomogeneous material are approximated by their phase averages $\langle \boldsymbol{\varepsilon} \rangle^{(p)}$ and $\langle \boldsymbol{\sigma} \rangle^{(p)}$, i.e., piecewise (phase-wise) uniform stress and strain fields are employed. The phase geometry enters these models via statistical descriptors.

  Mean field approaches tend to be formulated in terms of the phase concentration tensors, they pose low computational requirements, and they have been highly successful in describing the thermoelastic response of inhomogeneous materials.

- Variational Bounding Methods: Variational principles are used to obtain upper and (in many cases) lower bounds on the overall elastic tensors, elastic moduli, secant moduli, and other physical properties of inhomogeneous materials the microgeometries of which are described by statistical parameters.

Because they do not explicitly account for *n*-particle interactions Mean Field Approaches are sometimes referred to as "non-interacting approximations" in the literature. They postulate the existence of an RVE and typically assume some idealized statistics of the phase arrangement at the microscale.

The second group of approximations is based on studying discrete microgeometries, for which they aim at fully accounting for the interactions between phases. It includes

- Periodic Microfield Approaches (PMAs), also referred to as periodic homogenization schemes or unit cell methods, see section2.2. In these methods the inhomogeneous material is approximated by an infinitely extended model material with a periodic phase arrangement. The resulting periodic microfields are usually evaluated by analyzing repeating unit cells (which may describe

microgeometries ranging from rather simplistic to highly complex ones) via analytical or numerical methods. Unit cell approaches are often used for performing materials characterization of inhomogeneous materials in the nonlinear range, but they can also be employed as micromechanically based constitutive models. The high resolution of the microfields provided by PMAs can be very useful in studying the initiation of damage at the microscale. Periodic microfield approaches can give detailed information on the local stress and strain fields within a given unit cell, but they tend to be computationally expensive.

- Windowing Approaches: Subregions ("windows") — usually of rectangular or hexahedral shape — are randomly chosen from a given phase arrangement and subjected to boundary conditions that guarantee energy equivalence between the micro- and macroscales. Accordingly, windowing methods describe the behavior of individual inhomogeneous samples rather than of inhomogeneous materials and give rise to apparent rather than effective macroscopic responses.
- Embedded Cell or Embedding Approaches: The inhomogeneous material is approximated by a model consisting of a "core" containing a discrete phase arrangement that is embedded within some outer region to which far field loads are applied. The material properties of this outer region may be described by some macroscopic constitutive law. Like PMAs, embedded cell approaches can resolve local stress and strain fields in the core region at high detail, but tend to be computationally expensive.
- Other homogenization approaches employing discrete microgeometries.

Because this group of methods explicitly study mesodomains as defined by [13] they are sometimes referred to as "mesoscale approaches". Figure 2.1shows a sketch of a volume element as well as PMA, ECA and windowing approaches applied to it.

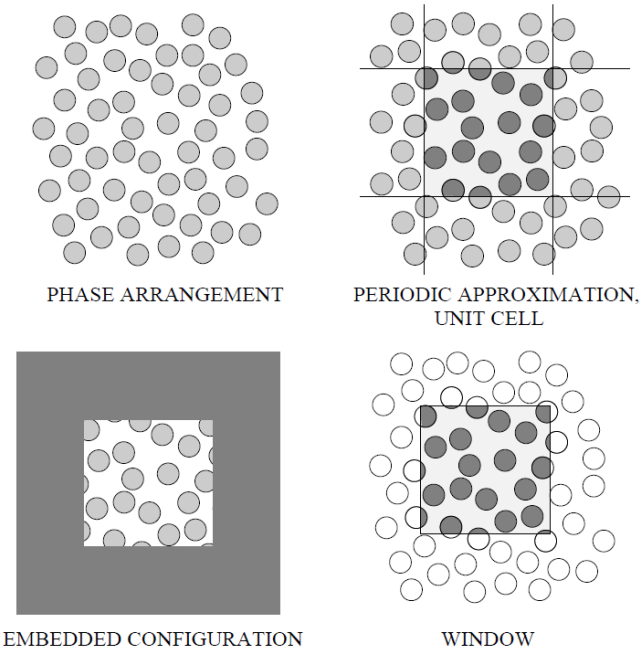

Figure 2.1 Schematic sketch of a random matrix–inclusion microstructure and of the volume elements used by a periodic microfield method (which employs a slightly different periodic "model" microstructure), an embedding scheme and a windowing approach to studying this inhomogeneous material **[10]**.

2.2. Periodic Microfield Models

Periodic Microfield Approaches (PMAs), which form the basis of the work done during the present project, are discussed in some detail in this section. PMAs aim at approximating the macroscopic and microscopic behavior of inhomogeneous materials by studying model materials that have periodic microstructures.

2.2.1. Basic Concepts of Unit Cell Models

Periodic microfield approaches analyze the behavior of infinite (one, two- or three-dimensional) periodic phase arrangements under the action of far field mechanical loads or uniform temperature fields. The most common approach to studying the stress and

strain fields in such periodic configurations is based on describing the microgeometry by a periodically repeating unit cell (RUC).

In periodic homogenization the strain and stress fields are decomposed into constant macroscopic strain and stress contributions ("slow variables"), $<\boldsymbol{\varepsilon}>$and $<\boldsymbol{\sigma}>$, and periodically varying microscopic fluctuations ("fast variables"), $\boldsymbol{\varepsilon}'(\mathrm{z})$ and $\boldsymbol{\sigma}'(\mathbf{z})$, by analogy to eqn.(2.2). Here **z** is a "microscopic coordinate" that has sufficient resolution for describing the variations on the microscale. In the small strain regime, the corresponding expression for the displacements takes the form [17]

$$\mathbf{u}(\mathbf{z}) = <\boldsymbol{\varepsilon}>\mathbf{z} + \mathbf{u}'(\mathbf{z}). \tag{2.12}$$

Volume integrals for obtaining averages, eqns.(2.4) and (2.6), must, of course, be solved over the volume of the unit cell, Ω_{UC}. Formal derivations of the above relationships for periodically varying microstrains and microstresses show that the work done by the fluctuating stress and strain contributions vanishes, compare [18].

Evidently, in periodic microfield approaches each unit of periodicity (unit cell) contributes the same increment of the displacement vector $\Delta\mathbf{u}$ so that the homogenized displacements vary (multi)linearly. An idealized depiction of such a situation is presented in Figure 2.2, which shows the variations of the strains $\varepsilon_s(s) = <\varepsilon_s> + \varepsilon'_s(s)$ and of the corresponding displacements $u_s(s) = <\varepsilon_s>\, s + u'_s(s)$ along some line s in a hypothetical periodic two-phase material consisting of constituents A and B. Obviously, the relation $<\varepsilon_s> = \Delta u_s/c_{\mathrm{u}}$ holds for linear displacement-strain relations, where c_{u} stands for the length of a unit cell in direction s and Δu_s for the corresponding displacement increment. The periodicity of the strains and of the displacements is immediately apparent.

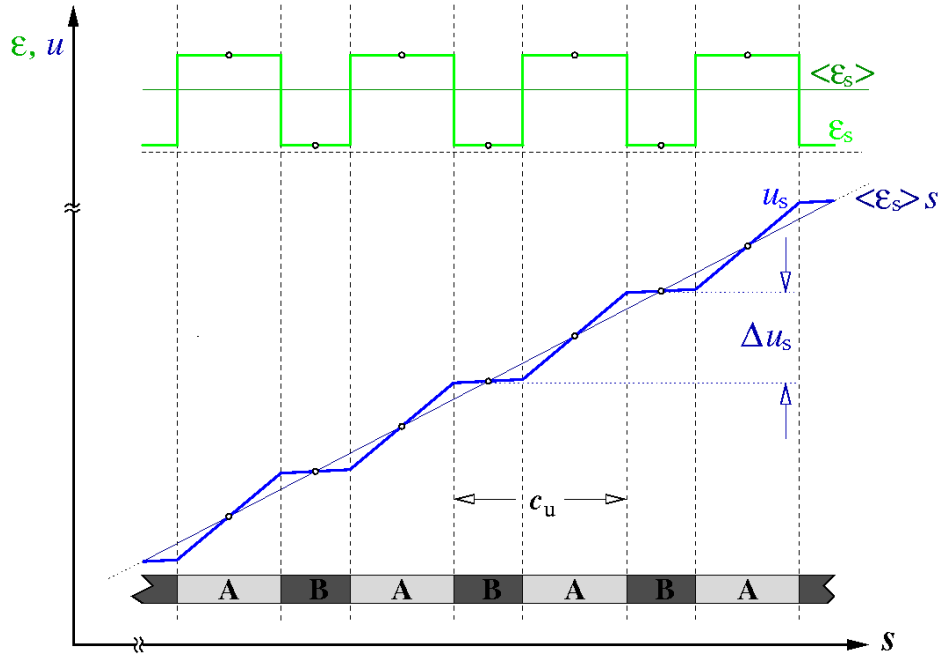

Figure 2.2 Schematic depiction of the variation of the strains $\varepsilon_s(s)$ and the displacements $u_s(s)$ along a generic "one-dimensional composite" (coordinate s) consisting of constituents A and B. Symmetry points of $\varepsilon_s(s)$ and $u_s(s)$ are indicated by small circles **[10]**.

2.2.2. Boundary Conditions

Unit cells together with the boundary conditions (B.C.s) prescribed on them must generate valid tilings both of the undeformed geometry and for all deformed states pertinent to a given micromechanical problem. Accordingly, the cells must be geometrically compatible. In order to achieve this, the boundary conditions for the unit cells must be specified in such a way that all deformation modes appropriate for the load cases to be studied can be attained. The three major types of boundary conditions used in periodic microfield analysis are periodicity, symmetry, and antisymmetry (or point symmetry) B.C.s. In PMA models one of these three types of boundary conditions (or a combination of them) must be used.

Figure 2.3 depicts a (two-dimensional) periodic hexagonal array of circular inhomogeneities (e.g., fibers oriented normally to the plane) and some of the unit cells that can be used to study aspects of the behavior of this phase arrangement.

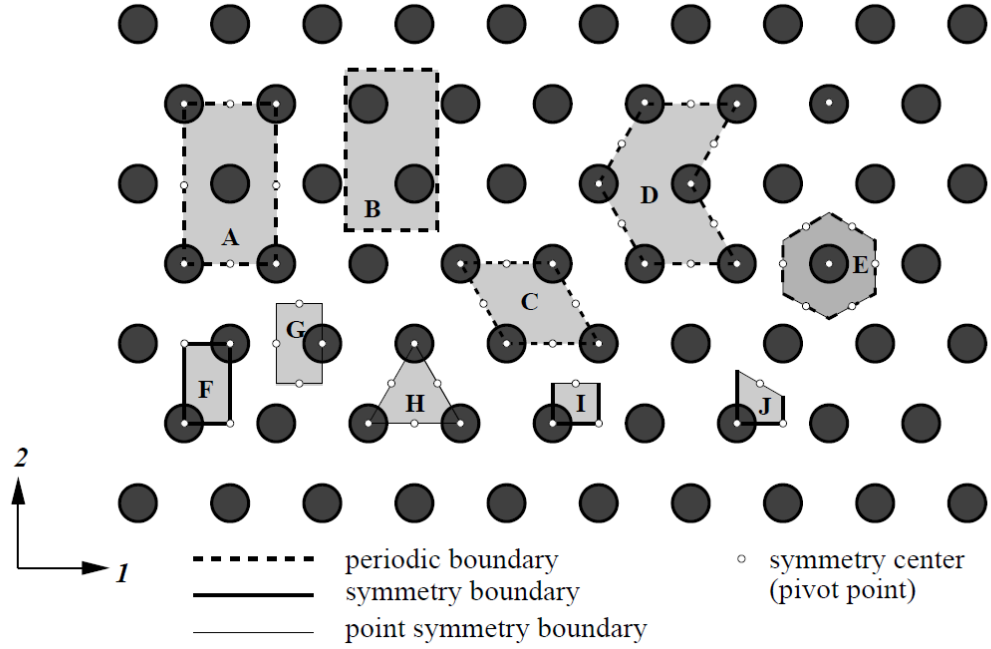

Figure 2.3 Periodic hexagonal array of circular inhomogeneities in a matrix and 10 unit cells that can be used to describe the mechanical responses of this arrangement under loads acting parallel to the coordinate axes **[10]**.

In the following a nomenclature is used in which the faces of two-dimensional quadrilateral unit cells are denoted as N, S, E and W (for North, South, East, and West), vertices being named according to the adjoining cell faces, compare Figure 2.6, Figure 2.7 and Figure 2.8**¡Error! No se encuentra el origen de la referencia.**. The faces of three-dimensional cells of hexahedral shape are, by analogy, referred to as N, S, E, W, B and T (the latter standing for bottom and top), and edges as well as vertices are referred to by the adjoining faces (e.g., SE or SWB), see Figure 2.5.

In the following, only periodicity boundary conditions will be discussed in detail.

Periodicity Boundary Conditions

The most general boundary conditions for unit cells in continuum micromechanics are periodicity (“toroidal”, “cyclic”) B.C.s. Periodicity boundary conditions make use of translatoric symmetries of a given geometry; in Figure 2.3cells A to E belong to this group.

Periodic phase arrangements are characterized by sets of periodicity vectors $\mathbf{p}_n$. For any given periodic microgeometry the minimum volume of pertinent unit cells is well defined, but such "minimum unit cells" can take a wide range of shapes as is shown for a simple two-dimensional case in Figure 2.4. The surface of any unit cell to be used with periodicity boundary conditions must consist of at least N pairs of faces (or pairs of parts of faces) Γ_k, and the surface elements making up a given pair, $k^-$and k^+, must be identical but shifted relative to each other by "shift vectors" $\mathbf{c}_k$. Each shift vector, in turn, must be a linear combination of the periodicity vectors, i.e., $\mathbf{c}_k=\Sigma_l c_l^k \mathbf{p}_l$, where the c_l^k are integer numbers. In Figure 2.4pairs of faces (or, in the case of some cells, parts of faces) Γ_k are marked by being drawn in the same line style.

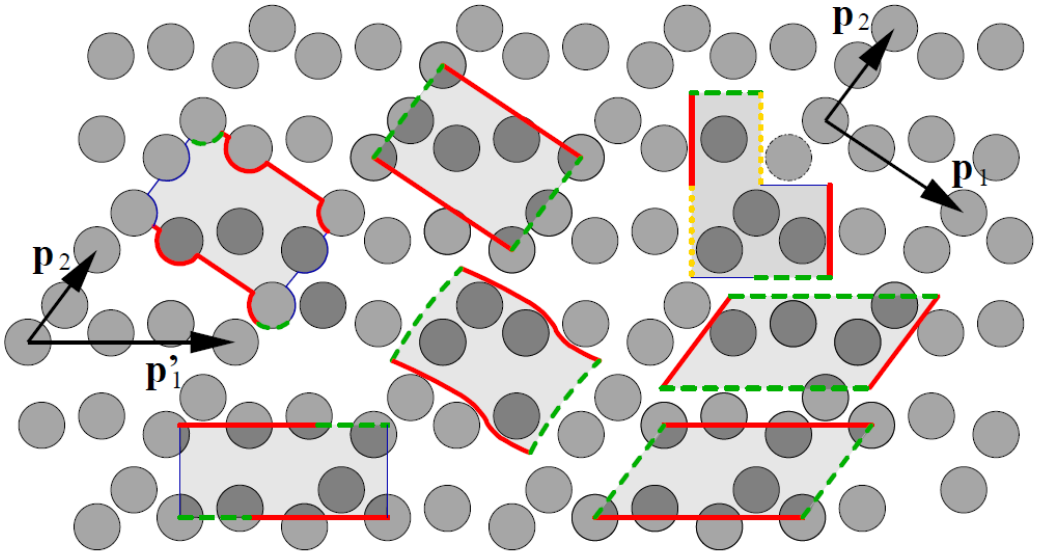

Figure 2.4 Seven different but equivalent periodic minimum-size unit cells for a two-dimensional periodic matrix–inclusion medium with two (slightly) non-orthogonal translation vectors $\mathbf{p}_1$ and $\mathbf{p}_2$. Paired faces (or parts of faces) Γk are marked by identical line styles and regions belonging to one of the cells are highlighted by shading **[10]**.

Unit cells of simple shape to some extent facilitate the application of periodicity boundary conditions.

Because the unit cells tile the computational space by translation, neighboring cells must fit into each other in both undeformed and deformed states. For each pair of surface elements, Γ_k, eqn. (2.12) allows to express periodicity boundary conditions for the mechanical problem in the small strain regime as

$$\Delta \mathbf{u}_k = \mathbf{u}_{k+} - \mathbf{u}_{k-} = \mathbf{u}(\mathbf{s}_k + \mathbf{c}_k) - \mathbf{u}(\mathbf{s}_k) = \langle \boldsymbol{\varepsilon} \rangle * \mathbf{c}_k, \qquad (2.13)$$

where $\mathbf{u}_{k-}$ and $\mathbf{u}_{k+}$ are the displacements at pairs of "homologous" points $s_k$and $s_k + c_k$ on the surface elements $k^-$and k^+(which may, e.g., correspond to faces N and S in Figure 2.5 and Figure 2.6), respectively;"*" denotes the contraction operation between the rank-2 tensor $\boldsymbol{\varepsilon}$ and the vector $\mathbf{c}$. The vector linking such pairs of points is in a deformed state is$\hat{\mathbf{c}}_k = \mathbf{c}_k + \Delta \mathbf{u}_k$. The macroscopic strain $\langle \boldsymbol{\varepsilon} \rangle$is prescribed in displacement controlled analysis and must be determined in load controlled analysis. These conditions enforce a seamless fit between neighboring unit cells for all possible deformed states.

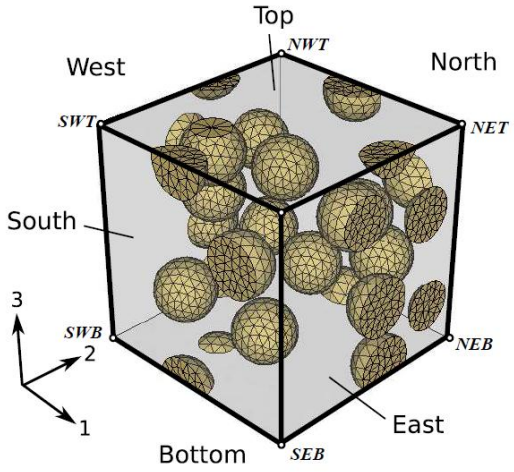

Figure 2.5 Cube-shaped periodic unit cell containing 15 randomly positioned spherical particles of equal size at a volume fraction of ξ(i)=0.15. Designators of the six faces (East, West, North, South, Top, Bottom) and of the vertices are given **[19]**

For the special case of initially rectangular two-dimensional unit cells, such as the one shown in Figure 2.6, eqns. (2.13) lead to the expressions

$$\mathbf{u}_N(\tilde{s}_1) = \mathbf{u}_N(\tilde{s}_1) + \mathbf{u}_{NW} \qquad \mathbf{u}_E(\tilde{s}_2) = \mathbf{u}_W(\tilde{s}_2) + \mathbf{u}_{SE} \qquad (2.14)$$

where vertex SW is assumed to be fixed and $\tilde{s}_k$ are local "face coordinates" that are used to denote homologous points on pairs of faces. Equations (2.14) directly imply that

$$\mathbf{u}_{NE} = \mathbf{u}_{NW} + \mathbf{u}_{SE}.$$

Conditions analogous to eqn. (2.14) can be specified for any periodic, space-filling and regular two-dimensional cell that has an even number of sides or three-dimensional

cell that has an even number of faces (cubes, hexahedra...). Compared to other discrete microstructure approaches, periodic homogenization typically shows the fastest convergence in terms of sizes of volume elements, see, e.g., [20].

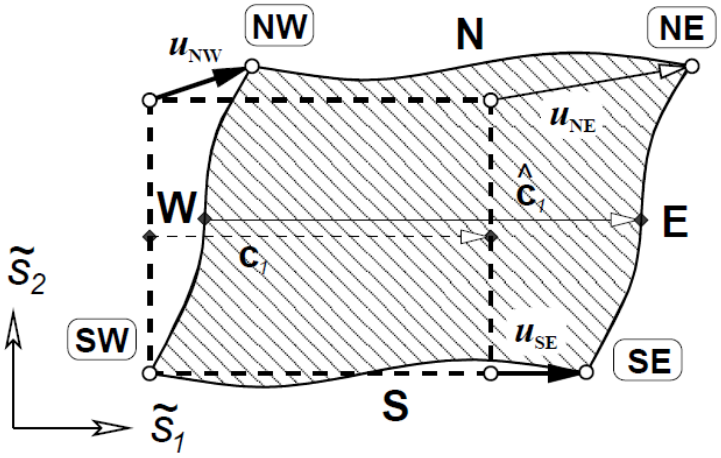

Figure 2.6 Sketch of periodicity boundary conditions as used with an initially rectangular two-dimensional unit cell.

2.2.3. Application of Loads and Evaluation of Fields

Once suitable unit cells have been defined and appropriate boundary conditions applied, the volume elements must be subjected to appropriate loads in the form of uniform macroscopic stresses as well as strains and/or homogeneous temperature excursions, i.e., the microscopic and macroscopic fields must be linked. There are two major approaches to implementing the micro–macro linkage: Asymptotic Homogenization and the Method of Macroscopic Degrees of Freedom. Because the present work uses the latter approach, it is discussed in some detail.

Method of Macroscopic Degrees of Freedom

Far field stresses (in the case of load controlled analysis) or strains (in the case of displacement control) can be applied to a given unit cell via concentrated nodal forces or prescribed displacements, respectively, at the master nodes. This approach was termed the “method of macroscopic degrees of freedom” by [17].

For the configuration of Figure 2.6 the concentrated forces acting on the master nodes SE and NW of a two-dimensional unit cell, $\mathbf{f}_{SE}$ and $\mathbf{f}_{NW}$, can be shown to be given by the surface integrals

$$\mathbf{f}_{SE} = \int_{\Gamma_E} \mathbf{t}^a(\mathbf{z}) d\Gamma \qquad \text{and} \qquad \mathbf{f}_{NW} = \int_{\Gamma_W} \mathbf{t}^a(\mathbf{z}) d\Gamma \qquad (2.15)$$

Here $\mathbf{t}^a(s) = \boldsymbol{\sigma}^a * \mathbf{n}_\Gamma(\mathbf{s})$ stands for the homogeneous surface traction vector corresponding to the macroscopic (applied, far field) stress field at some given point **s**on the cell's surface Γ_{UC}, and $\mathbf{n}_\Gamma(\mathbf{s})$ is the local normal vector of the appropriate face. Equation (2.15)can be generalized to require that each master node is loaded by a force corresponding to the surface integral of the surface traction vectors over the face slaved to it via an equivalent of eqns. (2.15).

In the case of rectangular or hexahedral unit cells that are aligned with the coordinate axes, averaged engineering stress and strain components can, of course, be evaluated by dividing the applied or reaction forces at the master nodes by the appropriate surface areas and by dividing the displacements of the master nodes by the appropriate cell lengths, respectively.

In order to obtain three-dimensional homogenized elastic tensors with the method of macroscopic degrees of freedom six suitable, linearly independent load cases must be solved for.

2.2.4. Unit Cell Models for Composites Reinforced by Continuous Fibers

Composites Reinforced by Unidirectional Continuous Fibers

Composites reinforced by continuous aligned fibers typically show a statistically transversely isotropic overall behavior and can be studied well with periodic homogenization.

Materials characterization with the exception of the overall axial shear behavior can be carried out with two-dimensional unit cell models employing generalized plane strain

elements that use a global degree of freedom for describing the axial deformation of the whole model. For handling the overall axial shear response special generalized plane strain elements [21]; [22] or three-dimensional models with appropriate periodicity boundary conditions [23] are required. Basic generalized plane strain models of continuously reinforced composites make use of simple periodic fiber arrangements as shown in Figure 2.7, all of which can be described by rather small unit cells using symmetry and/or antisymmetry B.Cs. The simplest among these arrangements are the periodic hexagonal (PH0) and periodic square (PS0) arrays.

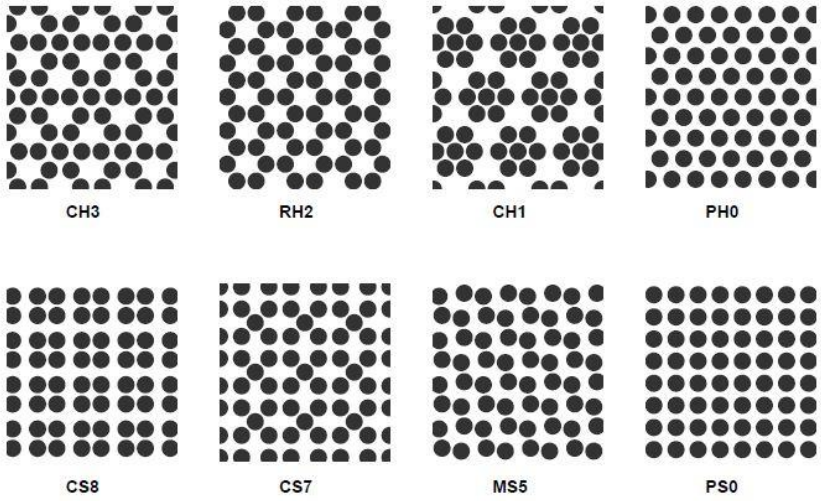

Figure 2.7 Eight simple periodic fiber arrangements of fiber volume fraction ξ=0.475 for modeling continuously fiber reinforced composites **[24]**.

Models with hexagonal symmetry (PH0,CH1,RH2,CH3) give rise to transversely isotropic thermoelastic overall behavior, whereas the other fiber arrangements shown in Figure 2.7 give rise to elastic tensors of tetragonal or lower symmetry. In the elastoplastic range the macroscopic symmetries of the fiber arrangements are degraded for most load cases, see Figure 2.8. This behavior is due to the low symmetry of the distributions of the material state fields in the matrix, which depend on the load history a given point has undergone.

Much improved models can be obtained by periodic multi-fiber unit cells that employ quasi-random fiber positions. Such models can either use symmetry B.C.s, compare the unit cell shown in Figure 2.9, which is based on the work of [25], or periodicity B.C.s ([26]; [27]; [28]).

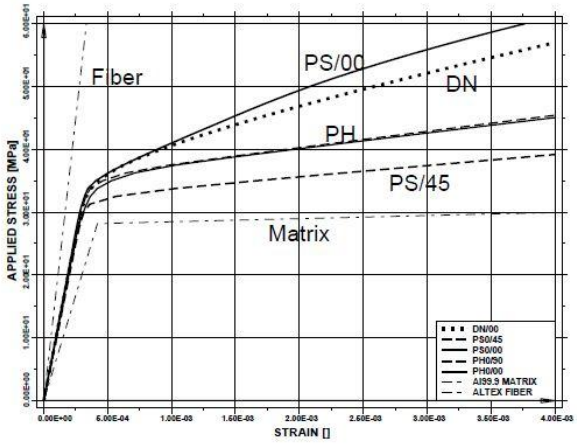

Figure 2.8 Transverse elastoplastic response of a unidirectional continuously reinforced ALTEX/Al MMC (ξ=0.453, elastoplastic matrix with linear hardening) to transverse uniaxial loading as predicted by unit cell models PH0, PS0 and DN **[10]**.

The overall behavior under transverse mechanical loading depends markedly on the phase arrangement, see Figure 2.8. Multi-fiber unit cells that approach statistical transverse isotropy (such as the one shown in Figure 2.9) tend to show noticeably stronger macroscopic strain hardening compared to periodic hexagonal arrangements of the same fiber volume fraction, compare [26].

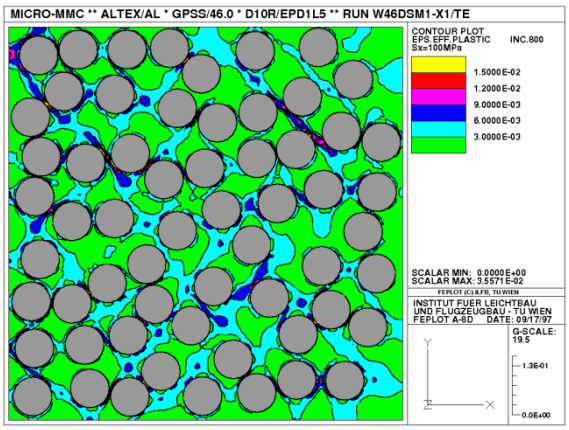

Figure 2.9 Microscopic distributions of the accumulated equivalent plastic strain in the matrix of a transversely loaded unidirectional continuously reinforced ALTEX/Al MMC (ξ=0.453) as predicted by a multi-fiber unit cell (arrangement DN) **[10]**.

The distributions of microstresses and microstrains in fibers and matrix typically depend strongly on the fiber arrangement, especially under thermal and transverse mechanical loading.

2.3. Isotropization

The present work makes use of the concept of isotropization, which consists in obtaining the closest isotropic elasticity tensor to some given elasticity tensor, which may be defined on the basis of one of three definitions of "elastic distance" [29]: the standard Frobenius or Euclidean norm, the Riemannian distance of tensors and the log-Euclidean norm.

The Euclidean distance function is not invariant under inversion (i.e., in the present case, considering compliance instead of elasticity) so it does not lead to a unique answer to the closest isotropic elasticity tensor. On the contrary, the closest elastic tensors (and, thus, the "closest elastic moduli") are unique for the Riemannian [30] and the log-Euclidean metrics [31]. These, accordingly, provide suitable means for defining the distance between any two elasticity tensors. In addition to finding the closest isotropic tensors, these norms can also be used to obtain the closest transversally isotropic tensors, or, in fact, the closest elastic tensor of any symmetry, to some given elasticity tensor.

Because the present work uses the log-Euclidian metric for evaluating the closest isotropic or transversally isotropic elastic tensors to ensemble averaged tensors from unit cell models, its definition is discussed in some detail. For further information about the other distance functions, see, e.g., [32], [33].

Minimum log-Euclidean distance

The log-Euclidean distance between two tensors, d_L, [31] is defined as

$$\mathrm{d}_L(\mathbf{A}, \mathbf{B}) = \|\mathrm{Log}(\mathbf{A}) - \mathrm{Log}(\mathbf{B})\|, \qquad (2)$$

where $\mathbf{A}$ and $\mathbf{B}$ are any pair of positive definite symmetric matrices in $\mathrm{M}^{n \times n}$, the space n x n of real matrices. In the present work $n = 6$ due to the application to elasticity tensors in Kelvin (matrix) representation.

The notation used for isotropic matrices defines the matrices $\hat{\mathbf{J}}, \hat{\mathbf{K}}, \hat{\mathbf{L}}$ and $\hat{\mathbf{M}}$ by

$$\widehat{\mathbf{K}} = \hat{\mathbf{I}} - \hat{\mathbf{J}}, \quad \hat{\mathbf{J}} = \boldsymbol{u}\boldsymbol{u}^T, \quad \text{where } \boldsymbol{u} = \left(\tfrac{1}{\sqrt{3}}, \tfrac{1}{\sqrt{3}}, \tfrac{1}{\sqrt{3}}, 0,0,0\right)^T \tag{2}$$

Here, $\hat{\mathbf{J}}$ and $\widehat{\mathbf{K}}$ denote the volumetric and deviatoric basis tensors. The closest isotropic elastic moduli obviously must be of general isotropic form ($\hat{\mathbf{C}}_{\boldsymbol{iso}}(3\kappa, 2\mu)$). In the following $\hat{\mathbf{C}}$ is a given elasticity tensor and $\hat{\mathbf{C}}_{\boldsymbol{iso}}$ the closest isotropic stiffness tensor and

$$\mathrm{Log}\left(\hat{\mathbf{C}}_{\boldsymbol{iso}}(3\kappa, 2\mu)\right) = \mathrm{Log}\left(3\kappa\hat{\mathbf{J}} + 2\mu\widehat{\mathbf{K}}\right) \qquad \kappa, \mu > 0, \tag{2}$$

where κ and μ are the bulk modulus and the shear modulus, respectively, which together with the volumetric and deviatoric basis tensors, $\hat{\mathbf{J}}$ and $\widehat{\mathbf{K}}$, uniquely describe the closest isotropic elastic tensor.

These bulk and shear moduli are found by minimizing $\mathrm{d}_L(\widehat{\mathbf{C}}, \hat{\mathbf{C}}_{\boldsymbol{iso}})$, which implies

$$\log(3\kappa_L) = \mathrm{tr}\,\hat{\mathbf{J}}\,\mathrm{Log}(\hat{\mathbf{C}}), \qquad 5\log(2\mu_L) = \mathrm{tr}\,\widehat{\mathbf{K}}\,\mathrm{Log}(\hat{\mathbf{C}}). \tag{2}$$

The formulae for the closest isotropic moduli to the anisotropic elastic tensor $\widehat{\boldsymbol{C}}$ can then be found as

$$\kappa_L = \tfrac{1}{3}\exp(\mathrm{tr}\,\hat{\mathbf{J}}\,\mathrm{Log}(\hat{\mathbf{C}})), \qquad \mu_L = \tfrac{1}{2}\exp(\tfrac{1}{5}\mathrm{tr}\,\widehat{\mathbf{K}}\,\mathrm{Log}(\hat{\mathbf{C}})), \tag{2}$$

the logarithm and exponent of the elastic tensors being evaluated in terms of logarithms and exponents of their eigenvalues, i.e., in spectral notation. An analogous procedure can be used for evaluating the closest transversally isotropic tensors [34].

Chapter 3
Modeling

In this chapter, issues regarding geometry and material properties are discussed, e.g., the selection of elements and the modeling of the orientations of the grains making up the matrix. The major part of the geometry modeling was done with ABAQUS/CAE. Python scripts and the in-house code MedTool were used for setting up the material orientations and the periodicity boundary conditions.

Two model geometries were used for studying continuously reinforced composites:

I. A matrix formed of an arrangement of columnar, regular hexahedral grains of random material orientations with the fibers set in the center of the grains, as shown in Figure 3.4.

II. A matrix formed of an arrangement of columnar, regular hexahedral grains of random material orientations with the fibers at the triple points of the grains, as shown in Figure 3.5.

In both cases the fibers were taken to be aligned with the “long" direction of the columnar grains.

Identical sets of grain orientations were used for both composite geometries, giving rise to the following set of homogenization runs:

- Model 0: Inhomogeneous matrix alone, i.e., without fibers; 20 different sets of random grain orientations were used, and an estimate for the effective elastic behavior of the inhomogeneous matrix was obtained by ensemble averaging over the resulting 20 homogenized elasticity tensors.

For each of the above composite models, two different models are studied.

- Model 1: The fibers were embedded in the same 20 inhomogeneous matrix configurations, the macroscopic responses of the composite being evaluated by single step homogenization. Estimates for the effective elastic responses were then obtained by ensemble averaging over the 20 configurations.

- Model 2: The fibers were embedded in a uniform matrix with the ensemble averaged, effective behavior evaluated from configuration 1), which constitutes a two-step homogenization procedure.

In addition, the closest isotropic elasticity tensor to the ensemble averaged, homogenized results for the pure matrix, model 0, was evaluated and used in analytical and numerical homogenization schemes. In analogy to model 2 the resulting descriptions are two-step homogenization procedures.

3.1. Geometry modeling

Since the main objective of this work is comparing single-step and two-step homogenization procedures based on periodic homogenization, the first step is to define suitable model geometries for carrying out the analyses.

This being a pilot study, the simplest model geometries suitable for the purpose were chosen, viz., continuous, aligned fibers embedded in a matrix, which can be described by essentially two-dimensional models, compare section 2.2.4, and are, accordingly, much simpler to handle than, say, models of particle reinforced composites, which require fully three-dimensional descriptions. The selected phase geometries are synthetic, periodic arrays of continuous aligned fibers in regular hexagonal arrangements corresponding to geometries PH0 and RH2 in Figure 2.7Figure 2.8 Transverse elastoplastic response of a unidirectional continuously reinforced ALTEX/Al MMC (ξ=0.453, elastoplastic matrix with linear hardening) to transverse uniaxial loading as predicted by unit cell models PH0, PS0 and DN.. These fiber arrangements, on the one hand, can be easily combined with regular hexagonal, columnar grains in the matrix and, on the other hand, give rise to transversally isotropic elastic behavior when combined with a homogeneous matrix.

In order to approach isotropic matrix behavior, three-dimensionally randomly oriented grains had to be used, implying three-dimensional analysis. Taking advantage of the two-dimensional nature of the geometries normal to the direction of the fibers and the columnar matrix grains, the Finite Element models took the form of "thin plates" consisting of a single layer of three-dimensional continuum elements in the fiber direction. The high symmetry of the selected arrangements allowed to build up the geometries of the multi-fiber unit cells, which are based on a matrix formed of a number of reinforced grains, from a number of identical, hexahedral units. Accordingly, meshing was based on processing a quarter of a regular, hexagonal shape with an edge length of 1 unit. This planar part was meshed with ABAQUS/CAE and extruded in the normal direction for obtaining a three-dimensional hexahedral model, the thickness of which was chosen such that the single layer of elements showed reasonable aspect ratios.

The above hexahedron was partitioned into matrix and fiber regions such that the chosen fiber volume fraction of $\xi = 0.25$ was obtained. The corresponding fiber radii are $r = 0.455$ edge lengths for grains with fibers at their centers and $r = 0.321$ for grains with fibers at the triple points, compare Figure 3.4 and Figure 3.5, respectively. The "matrix only" models, type 0, used the same meshes as the "fibers at centers" models.

3.2. Mesh definition

This section describes the meshing used for each model and issues relating to it. The mesh is built in the meshing module of ABAQUS/CAE, and the types of elements used are described below.

Meshing was based on quarter grains ("hexahedral base parts"), from which the mesh of the full hexagon can be generated by mirroring operations. To define the mesh and its elements size, the hexahedral "quarter grains" are split into 3 or 5 regions depending on the configuration, compare Figures 3.1 and 3.2. Node seeds are positioned at the edges of these regions in such manner that the mesh conforms to requirements and makes the analyses as computationally light as possible. Both the mesh density along the boundaries of the regions and the mesh density in their interiors are determined by the

seeds (or nodes) along the edges. For both configurations, seeds are positioned uniformly along the edges of all regions, see Figure 3.1 and Figure 3.2.

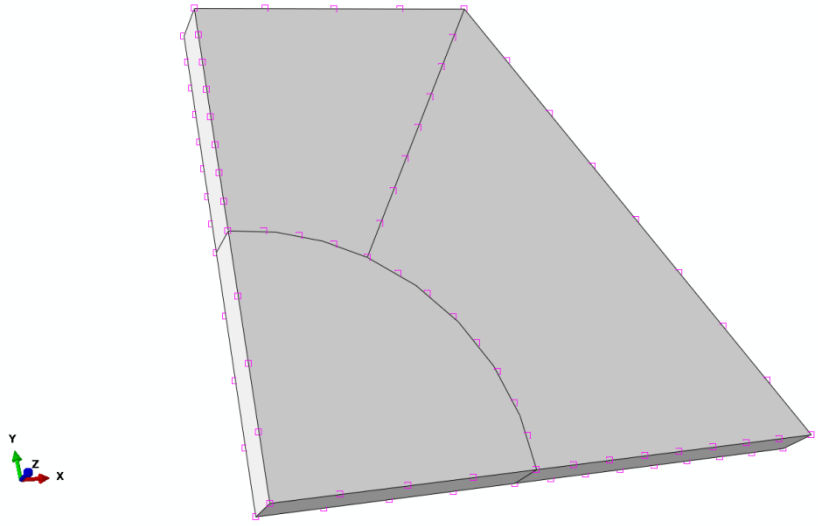

Figure 3.1 Seeds along edges. Configuration with fibers at centers of grains (I)

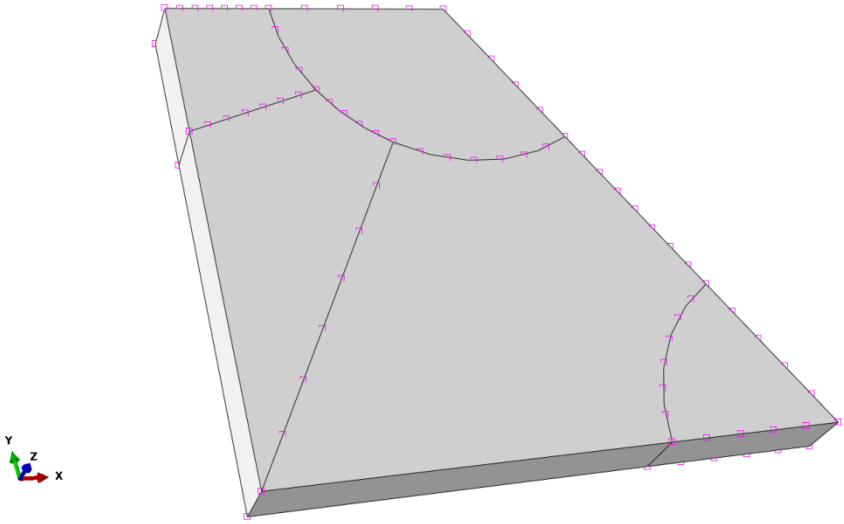

Figure 3.2 Seeds along edges. Configuration with fibers at triple points of grains (II)

In defining the node seeds account must be taken of the requirement that the base hexahedra after suitable rotation operations must fit together to build up the whole model. This requirement is most easily fulfilled by uniformly spreading the seeds along the edges, so that, when the hexahedra are joined to their neighbors, as explained in section 3.3, their nodes fit together perfectly.

Elements with quadratic interpolation are employed throughout the project, the element types being C3D15 “wedges” (15-node quadratic triangular prisms) for the fibers and C3D20 “hex elements” (20-node quadratic bricks) for the matrix.

Once the edges are seeded and the element types are set, the mesh is generated. Figure 3.3shows the meshed quarter grains for both configurations.

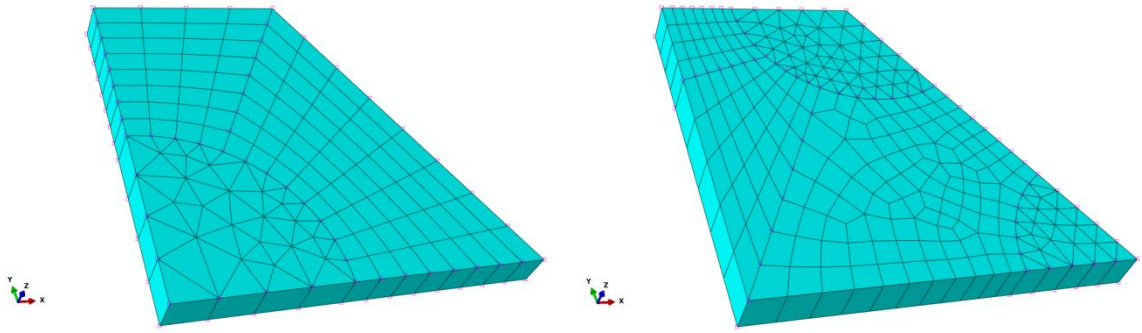

a) **b)**

Figure 3.3Hexahedral base part meshed, for a) fibers in the center (I) and b) fibers in the triple points of the grains (II)

3.3. Assembly modeling

Once the base hexahedron is built and meshed, as explained above, the mesh of a hexahedral grain is generated from the base hexahedra representing quarter grains by operations such as copying and rotating them in the Assembly module of ABAQUS/CAE. Thereupon, the whole model is assembled to comprise a total of 18 grains, some of which are split into halves and quarters to account for the models’ periodicity. The finished geometry configurations are shown in Figure 3.4 and Figure 3.5, for configurations of fibers at the centers of the matrix grains and fibers at their triple points, respectively.

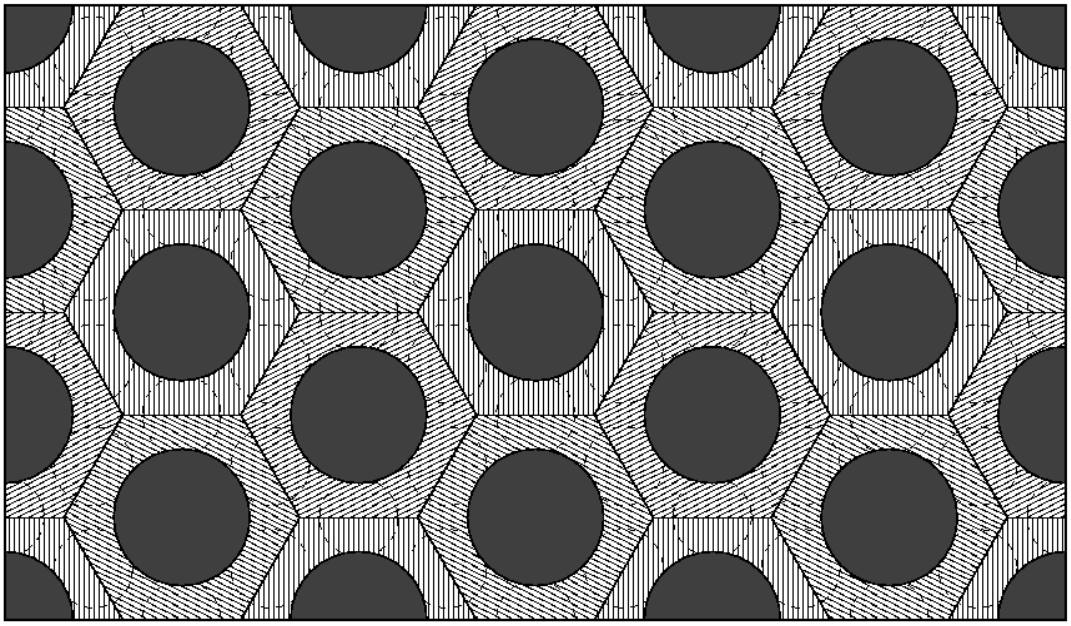

Figure 3.4 Model consisting of hexagonal matrix grains with fibers at their center (I)

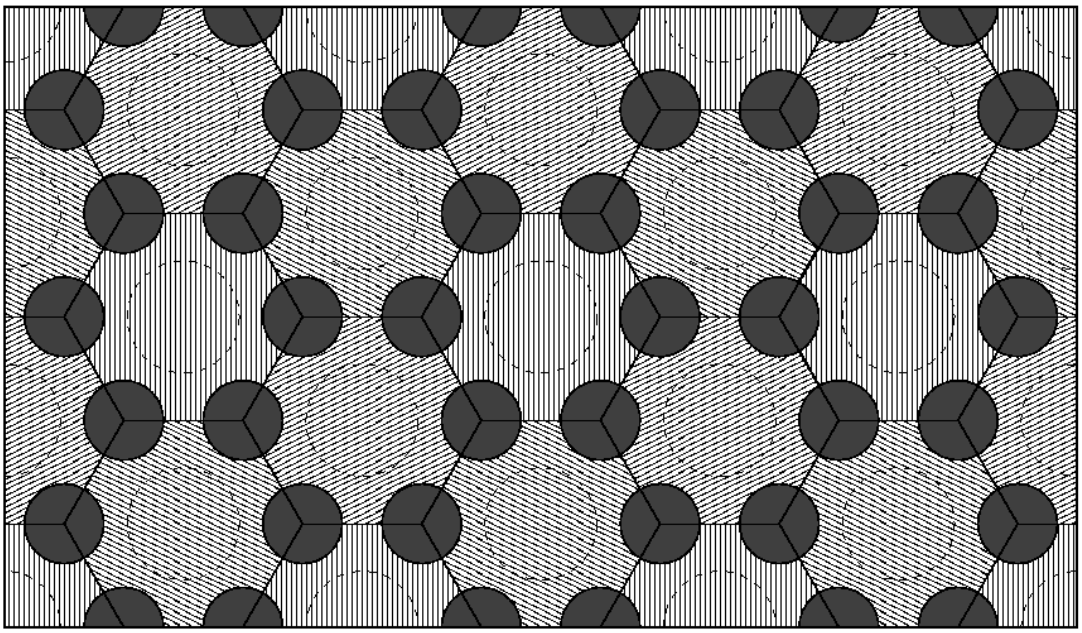

Figure 3.5 Model consisting of hexagonal matrix grains with fibers at their triple points (II)

In both models, sets of elements are defined from the sections to distinguish matrix and fiber regions in order to establish their properties in the material definition step, detailed in section 3.6. Those sets are numbered as “Set-i”, where the range of “i” depends on the constituent and on the phase geometry.

When creating the whole configuration, all the properties assigned to the base hexahedron are retained, such as the different sections and the mesh. Figure 3.6 and Figure 3.7 show the whole mesh assembly for both configurations studied in the present work.

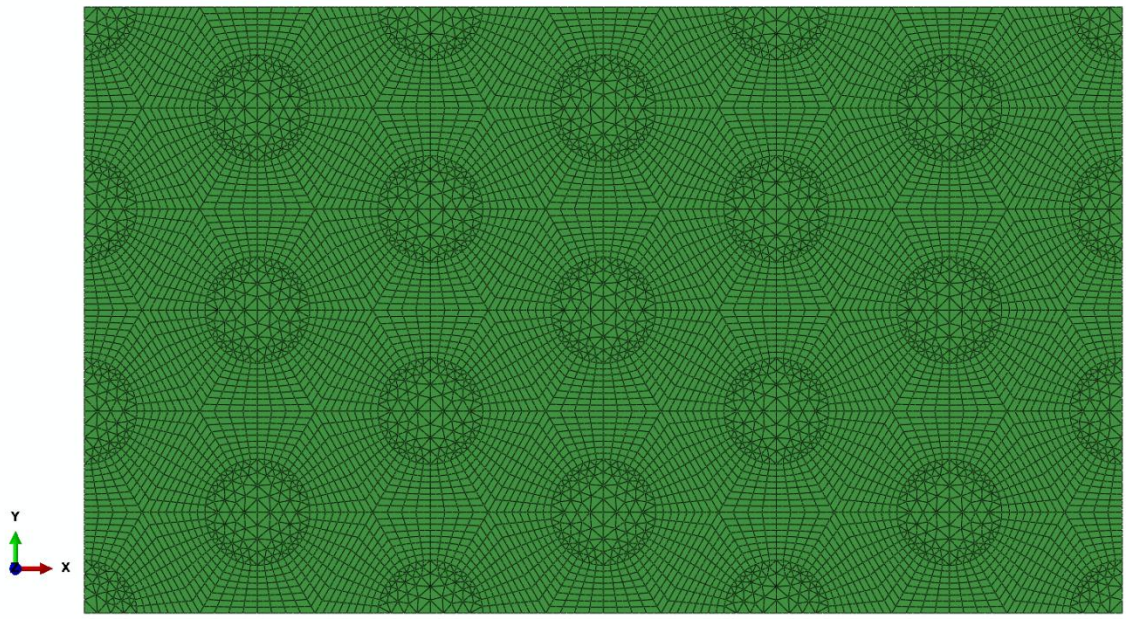

Figure 3.6 Meshed assembly with fibers at centers of grains (I)

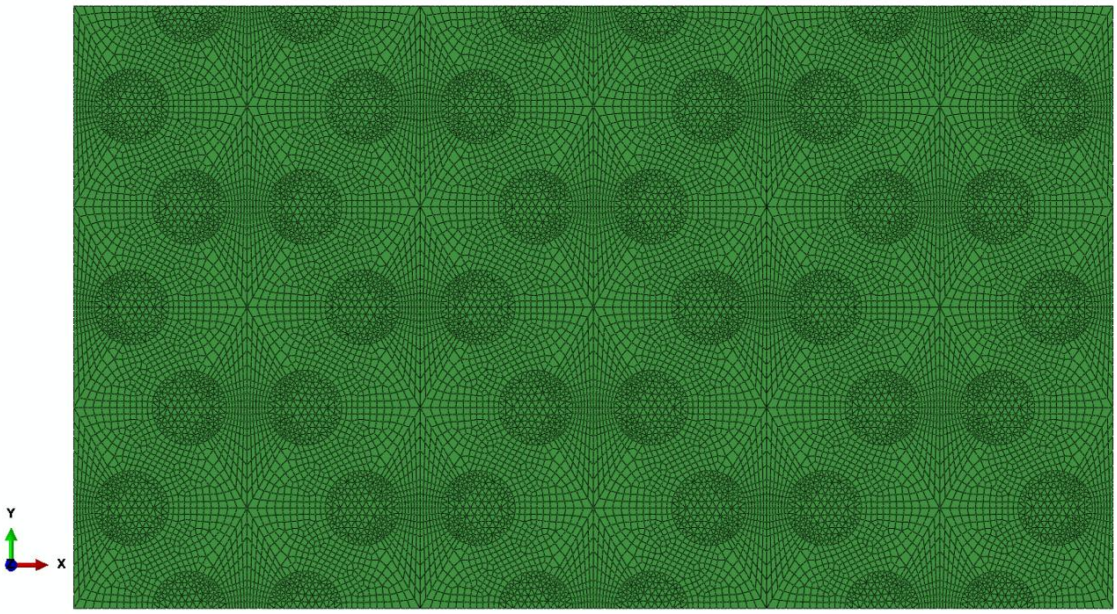

Figure 3.7 Meshed assembly with fibers at triple points of grains (II)

3.4. Material orientations

The matrix material used in this work is highly idealized, inhomogeneous and anisotropic at the grain level. The model for it is obtained by defining different random orientation systems for the grains making up the matrix, whereas all fibers use the same material orientation.

These random material orientation systems are generated by a script written in the programming language Python, which is included with the main ABAQUS input file using the *INCLUDE option.

The script gives each of the 18 hexahedra a different random local coordinate system for each run and a total of 20 such runs or sets of random material orientations are used in the study. The same 20 sets of matrix orientations were used with the first two sets of configurations defined at the start of chapter 3. For the homogenized matrix the material orientation was set equal to the geometry's coordinate system.

3.5. Boundary Conditions and Loads

The periodicity boundary conditions for the volume elements are generated with the ILSB in-house code MedTool [**8**]. The program, on the one hand, assigns names to the master nodes and other vertex nodes of the hexahedral unit cell in order to reference nodes for the application of loads, as shown in Figure 3.8 and as used in Figure 2.5.

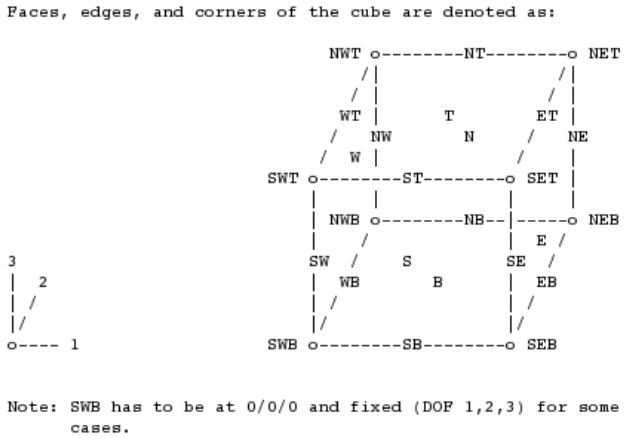

Figure 3.8 Designators of unit cell vertices, edges and faces as used in MedTool [8]

Here N, S, E, W, B and T stand for North, South, East, West, Bottom and Top, respectively. As indicated in Figure 3.8, the SWB node has to be at (0, 0, 0), at the origin of the global coordinate system.

Because only linear elastic material behavior was considered, the superposition principle holds and six linearly independent mechanical load cases are sufficient for evaluating the effective elasticity and compliance tensors of the inhomogeneous material. The six load cases applied to the volume element are three macroscopic normal stresses σ_{11}, σ_{22} and σ_{33} and three macroscopic shear stresses τ_{12}, τ_{13} and τ_{23}. These loads are applied via concentrated nodal forces acting on the master nodes as defined in Table 1, where the third line represents the master node to which the load is applied, the direction of application and the magnitude of the concentrated force. It also shows that the choice of load controlled analysis allowed PERTURBATION steps to be used, i.e., ABAQUS inverted the stiffness matrix only once and then evaluated the vector of displacement components by inserting the appropriate vectors of nodal forces.

Table 1 Loads applied in the ABAQUS analysis

*STEP, PERTURBATION	*STEP, PERTURBATION	*STEP, PERTURBATION	*STEP, PERTURBATION	*STEP, PERTURBATION	*STEP, PERTURBATION
Tensile 1	Tensile 2	Tensile 3	Shear 12	Shear 13	Shear 23
*STATIC	*STATIC	*STATIC	*STATIC	*STATIC	*STATIC
*CLOAD	*CLOAD	*CLOAD	*CLOAD	*CLOAD	*CLOAD
SEB, 1, 6.0	NWB, 2, 8.0	SWT, 3, 12.0	SEB, 2, 6.0	SWT, 1, 12.0	SWT, 2, 12.0

3.6. Material definition

The constituent material properties used in the present work for fibers and matrix do not correspond (and are not intended to correspond) to any real composite. Nevertheless, the constituent material data were chosen to approach existing materials to a reasonable extent. This section describes these material parameters. As mentioned above, thermo-mechanical and inelastic material behaviors, such as thermal expansion, plasticity or damage, are not taken into account.

For defining material properties and assigning them to the matrix grains and fibers, scripts in the Python programming language were written and then added to the main input file ABAQUS input file, assigning the properties to the appropriate sets of elements.

For each of the two geometry configurations described as I and II at the beginning of this chapter a range of five behaviors of fibers and one set of matrix properties are employed. The behaviors of the fibers correspond to a range of very stiff to extremely compliant inhomogeneities, the latter approaching cylindrical holes. Figure 3.9 and Figure 3.10 show matrix and fibers in different colors for configurations I and II, respectively.

The individual matrix grains are modeled with cubic elastic symmetry, the material parameters used being chosen to be one tenth of the ones of copper in order to reach high elastic contrasts when reinforced with typical carbon fibers. The corresponding material parameters for the matrix are listed in Table 2, where E stands for the Young's modulus, ν for the Poisson number, G for the shear modulus and M for the tetrahedral shear modulus, which differs from G in cubic materials. E_{11}, E_{12} and E_{44} are the values of the elements of the elasticity tensor.

As to the fibers, two sets of models describe transversely isotropic elastic responses similar to those of T-300 and P-100 carbon fibers, parameters being shown in Table 3 and Table 4, respectively. In these tables E_A stands for the axial Young's modulus, E_T for the transverse Young's modulus, ν_A and ν_T for the axial and transverse Poisson ratios, respectively, and G_A and G_T for the axial and transverse shear moduli, respectively. The three other fiber data sets show isotropic elasticity, with one approximating Nextel 312 oxidic fibers and the other two describing fictitious behaviors that are more compliant than that of the matrix. These properties are detailed in Table 5, Table 6 and Table 7.

The elastic phase contrast, which describes the level of inhomogeneity of the constituents' behavior given by equation (2.1), is also given in tables Table 3 Transversely isotropic T-300 carbon fibers (inhomogeneity a).Table 3 toTable 5 with respect to the matrix.

Table 2 Cubically elastic matrix

Elastic parameters for matrix grains			
E = 6.67 GPa	v = 0.42	G = 7.50 GPa	M = 2.35 GPa
E_{11} = 16.8 GPa	E_{12} = 12.1 GPa	E_{44} = 7.5 GPa	

Table 3 Transversely isotropic T-300 carbon fibers (inhomogeneity a).

T-300 Carbon Fibers			
E_A = 231.0 GPa	E_T = 13.8 GPa	v_A = 0.20	v_T = 0.25
G_A = 12.4 GPa	G_T = 5.52 GPa		
$c_{el} = \frac{E_A^{(i)}}{E^{(m)}} = \frac{231.0\ \text{GPa}}{6.67\ \text{GPa}} = 34.63$			
$c_{el} = \frac{E_T^{(i)}}{E^{(m)}} = \frac{13.8\ \text{GPa}}{6.67\ \text{GPa}} = 2.07$			

Table 4 Transversely isotropic P-100 carbon fibers (inhomogeneity b)

P-100 Carbon Fibers			
E_A = 758.0 GPa	E_T = 6.07 GPa	v_A = 0.41	v_T = 0.47
G_A = 15.5 GPa	G_T = 2.07 GPa		
$c_{el} = \frac{E_A^{(i)}}{E^{(m)}} = \frac{758.0\ \text{GPa}}{6.67\ \text{GPa}} = 113.64$			
$c_{el} = \frac{E_T^{(i)}}{E^{(m)}} = \frac{6.07\ \text{GPa}}{6.67\ \text{GPa}} = 0.91$			

Table 5 Isotropic Nextel 312 oxidic fibers (inhomogeneity c)

Nextel 312 Oxidic Fibers		
E = 151.7 GPa	v = 0.26	G = 60.2 GPa
$c_{el} = \frac{E^{(i)}}{E^{(m)}} = \frac{151.7\ \text{GPa}}{6.67\ \text{GPa}} = 22.74$		

Table 6 Isotropic fibers: hypothetical compliant inhomogeneities (inhomogeneity d)

Hypothetical Compliant Inhomogeneities		
E = 0.66 GPa	v = 0.1	G = 0.3 GPa
$c_{el} = \frac{E^{(i)}}{E^{(m)}} = \frac{0.66\ \text{GPa}}{6.67\ \text{GPa}} = 0.09$		

Table 7 Isotropic fibers: quasi-pores (inhomogeneity e)

Quasi- Pores		
E = 250 Pa	v = 0.25	G = 100 Pa
$c_{el} = \frac{E^{(i)}}{E^{(m)}} = \frac{250\ \text{Pa}}{6.67\text{GPa}} = 3.75\text{x}10^{-8}$		

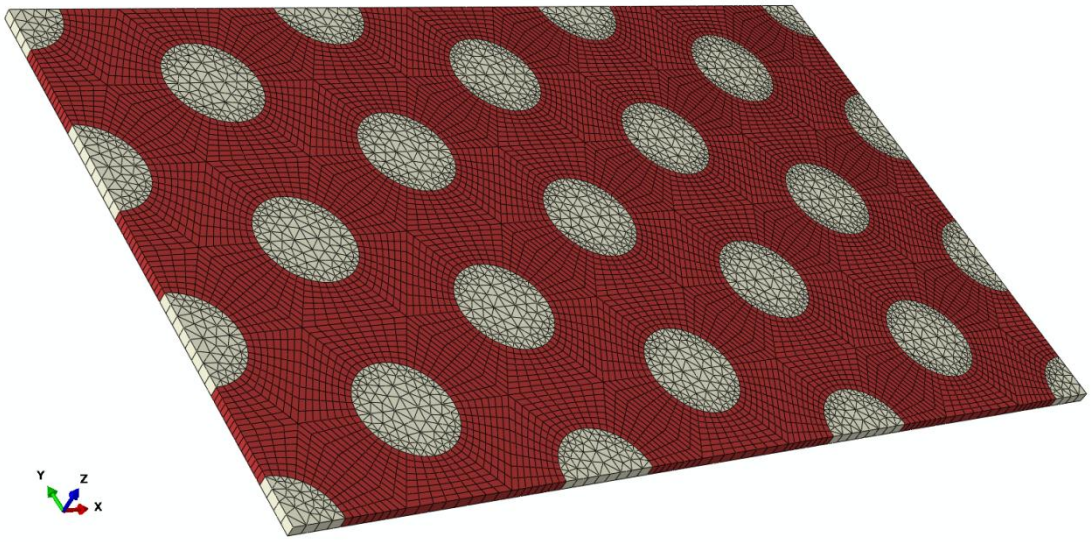

Figure 3.9 Constituents: fibers at the centers of matrix grains (I).

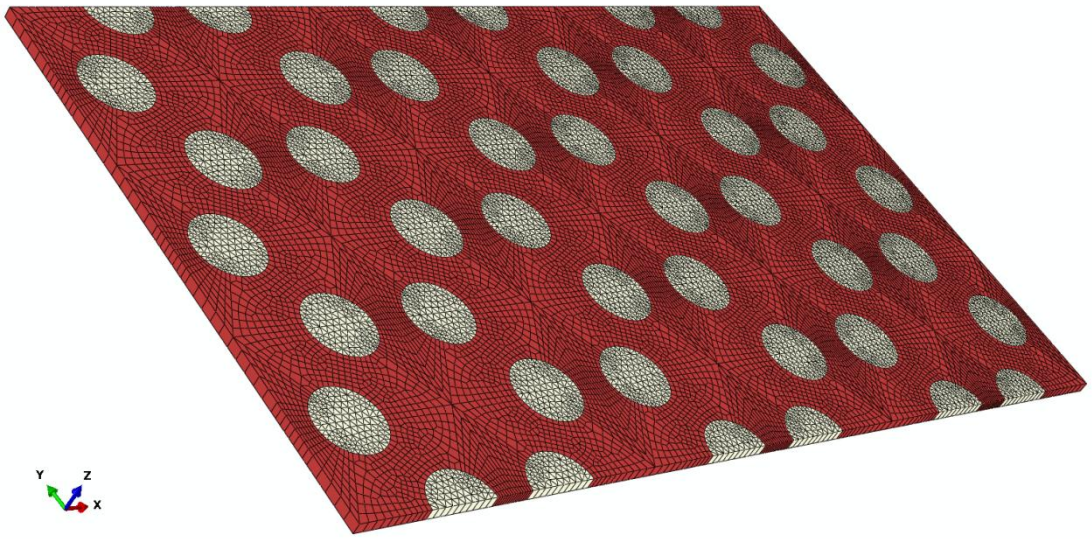

Figure 3.10 Constituents: fibers at triple points of matrix grains (II)

Chapter 4
Analysis and Results

As the aim of this thesis is to compare the macroscopic responses of different models of continuously fiber-reinforced composites in which the matrix is inhomogeneous, the main idea under consideration is the analysis of the macroscopic (and some microscopic) elastic responses obtained by periodic homogenization. Two different analysis strategies are used: one-step homogenization and two-step homogenization.

In both cases, the effective elastic properties of the composite are evaluated for one set of matrix elastic properties and configurations, but for five different elastic behaviors of the inhomogeneities, as defined in section 3.6. These results are presented in sections 4.2 to 4.6.

In addition, the ranges of the von Mises stresses and the first principal stresses are evaluated for the single step and two-step homogenization runs, only for the stiffer and the more compliant fibers, see sections 4.2 and 4.6, respectively.

This chapter is organized to account for the different materials, i.e., combinations of constituents, for ease of comparison. Section 4.1 contains results pertaining to the homogenized pure matrix. Sections 4.2 to 4.6 present results obtained for the five different fiber materials. Each of these sections is divided into 3 parts:

- A subsection on the **Ix configuration**, which contains results for the "fiber at grain center" models. These comprise the "direct" one-step and two-step results in the form of the 1E and 2E elasticity tensors, the relative differences between these tensors, and the transversally isotropic elasticity tensor (1ET) that is closest to the ensemble averaged one-step (1E) results. Furthermore, results on the ranges of the predicted phase level von Mises and first principal stress fields are provided for materials (a) and (e).

- A subsection on the **IIx configuration,** which presents results for the "fibers at triple points" models in the form of the 1E, 2E and 2ET elasticity tensors plus data on the ranges of stress fields for materials (a) and (e).

- A subsection on **effective moduli**, in which the transversally isotropic elastic moduli pertaining to the above configurations are listed together with analytical bounds in order to allow a direct comparison of these results.

Finally, some plots of microfields for selected configurations are shown in the final section of the chapter.

4.1. Homogenization and "isotropization" of the elastic behavior of the pure matrix

The ensemble averaged effective elasticity tensor, which describes the elastic behavior of the homogenized matrix used in the analyses using one-step homogenization, is presented here.

For obtaining this homogenized matrix behavior, the effective elastic responses pertaining to 20 sets of orientations of the anisotropic elastic tensors of the 18 grains making up the model of the pure matrix are evaluated with the FE-code ABAQUS/Standard. From each configuration the effective elasticity tensor is obtained and from these 20 tensors the ensemble averaged elasticity tensor is evaluated. This elasticity tensor, shown in Table 8, is anisotropic due to the limited number of configurations underlying the ensemble average and the relatively small number of grains per configuration. Since the anisotropic behavior closely approaches orthotropy, elastic moduli corresponding to this elastic symmetry are also listed. The ensemble averaged (0E) elasticity tensor is used for describing the matrix behavior in the two-step homogenization scheme for the effective elastic behavior of the composite.

Table 8 Ensemble averaged elasticity tensor and elastic constants of the matrix without fibers (configuration 0E, units of GPa)

Ensemble averaged effective elasticity tensor

$$\begin{pmatrix} 19{,}900 & 10{,}561 & 10{,}540 & -0{,}054 & -0{,}080 & 0{,}034 \\ 10{,}561 & 19{,}784 & 10{,}655 & 0{,}176 & 0{,}054 & 0{,}018 \\ 10{,}540 & 10{,}655 & 19{,}806 & -0{,}121 & 0{,}027 & -0{,}051 \\ -0{,}054 & 0{,}176 & -0{,}121 & 5{,}170 & -0{,}036 & 0{,}048 \\ -0{,}080 & 0{,}054 & 0{,}027 & -0{,}036 & 5{,}033 & -0{,}053 \\ 0{,}034 & 0{,}018 & -0{,}051 & 0{,}048 & -0{,}053 & 4{,}796 \end{pmatrix}$$

Engineering constants corresponding to the ensemble averaged, orthotropized effective elasticity tensor

E_1	12,585GPa	G_{23}	5,170GPa	ν_{23}	0.3561
E_2	12,366GPa	G_{13}	5,033GPa	ν_{13}	0.3447
E_3	12,410GPa	G_{12}	4,796GPa	ν_{12}	0.3483

In order to establish the accuracy of the tests carried out, the standard deviations of the components of the ensemble averaged elasticity tensor are calculated and presented in Table 9. Due to the limited number of grains and configurations these standard deviations are fairly high. Interestingly, the homogenized and ensemble averaged matrix behavior shows only moderate anisotropy in spite of the columnar grain structure used in the model.

Table 9 Homogenized, ensemble averaged elasticity tensor of the matrix with standard deviations (configuration 0E, units of GPa)

$$\begin{pmatrix} 19{,}900 \pm 0{,}473 & 10{,}561 \pm 0{,}325 & 10{,}540 \pm 0{,}296 & -0{,}054 \pm 0{,}295 & -0{,}080 \pm 0{,}366 & 0{,}034 \pm 0{,}514 \\ 10{,}561 \pm 0{,}325 & 19{,}784 \pm 0{,}468 & 10{,}655 \pm 0{,}286 & 0{,}176 \pm 0{,}365 & 0{,}054 \pm 0{,}196 & 0{,}018 \pm 0{,}492 \\ 10{,}540 \pm 0{,}296 & 10{,}655 \pm 0{,}286 & 19{,}806 \pm 0{,}370 & -0{,}121 \pm 0{,}297 & 0{,}027 \pm 0{,}397 & -0{,}051 \pm 0{,}216 \\ -0{,}054 \pm 0{,}295 & 0{,}176 \pm 0{,}365 & -0{,}121 \pm 0{,}297 & 5{,}170 \pm 0{,}326 & -0{,}036 \pm 0{,}197 & 0{,}048 \pm 0{,}223 \\ -0{,}080 \pm 0{,}366 & 0{,}054 \pm 0{,}196 & 0{,}027 \pm 0{,}397 & -0{,}036 \pm 0{,}197 & 5{,}033 \pm 0{,}291 & -0{,}053 \pm 0{,}280 \\ 0{,}034 \pm 0{,}514 & 0{,}018 \pm 0{,}492 & -0{,}051 \pm 0{,}216 & 0{,}048 \pm 0{,}223 & -0{,}053 \pm 0{,}280 & 4{,}796 \pm 0{,}346 \end{pmatrix}$$

Isotropized Matrix Behavior

The isotropic elasticity tensor closest to the (anisotropic) homogenized elasticity tensor presented in Table 2 was evaluated with the algorithm discussed in section 2.3. This isotropized matrix elasticity tensor and four of the corresponding moduli (of which, of course, only two are independent) are shown in Table 10.

Table 10 Isotropized, ensemble averaged elasticity tensor and elastic moduli of the matrix (configuration 0EI, units of GPa).

Isotropized, ensemble averaged effective elasticity tensor of the matrix

$$\begin{pmatrix} 20{,}123 & 10{,}439 & 10{,}439 & 0{,}000 & 0{,}000 & 0{,}000 \\ 10{,}439 & 20{,}123 & 10{,}439 & 0{,}000 & 0{,}000 & 0{,}000 \\ 10{,}439 & 10{,}439 & 20{,}123 & 0{,}000 & 0{,}000 & 0{,}000 \\ 0{,}000 & 0{,}000 & 0{,}000 & 4{,}842 & 0{,}000 & 0{,}000 \\ 0{,}000 & 0{,}000 & 0{,}000 & 0000 & 4{,}842 & 0{,}000 \\ 0{,}000 & 0{,}000 & 0{,}000 & 0{,}000 & 0{,}000 & 4{,}842 \end{pmatrix}$$

Effective elastic moduli corresponding to isotropized, ensemble averaged effective elasticity tensor

E	*ν*	*G*	*K*
12,992 GPa	0,342	4.842 GPa	13,667 GPa

Even though the model corresponds to very long, aligned, columnar grains the effective elastic moduli corresponding to the isotropized, ensemble averaged elasticity tensor are in good agreement with one tenth of typical values for polycrystalline copper found in the literature, see, e.g., [35].

Ranges of microfields in the pure matrix

Whereas tables 1 to 3 concentrate on the effective macroscopic behavior of the matrix, the present subsection provides data on the local stress fields in the form of the ranges of the effective (von Misses) stresses, σ_{vm} and the first principal stresses, σ_I. In order to find the range of the effective and first principal stresses for the ensemble of the 20 data sets, first the minimum and maximum values of the above fields for each data set are extracted at the integration point level, and then the minimum and maximum values of each within the ensemble are evaluated. Evaluating stress-like variables at the integration points has the advantage of not requiring special consideration of phase boundaries and the surfaces of unit cells, but tends to give rise to some mesh dependence of the results.

It is also worth noting that, being integration point values, this data may differ from the values shown in figures, which are results extrapolated to the nodes and then averaged over all elements containing a given node (“averaged at nodes” stresses in

ABAQUS parlance). Since six linearly independent load cases are required for evaluating the effective elasticity tensors, six different fields of stress tensors are available per model configuration. The load cases used in the analysis were uniaxial tensile stresses acting in the 1-, 2- and 3- directions (labeled as σ_{11}, σ_{22} and σ_{33} in the following) and simple shear loading in the 12-, 13- and 23-planes (referred to as τ_{12}, τ_{13} and τ_{23}). In order to make the resulting fields comparable, an appropriate normalization is required, which was done by referring the local stresses to the norms of the applied stress tensors. Table 11 shows the force, area and the applied stress pertaining to these six load cases.

Table 11 Data for normalization of local stress results

Force (value)	Plane of application (area)	$\boldsymbol{\sigma}$ applied (Force / area)	Load case
6	**yz** (5,19615·0,1)	11,54701	$\boldsymbol{\sigma_{11}}$
8	**xz** (9·0,1)	8,888889	$\boldsymbol{\sigma_{22}}$
12	**xy** (9·5,19615)	0,2566	$\boldsymbol{\sigma_{33}}$
6	**yz**(5,19615·0,1)	11,54701	$\boldsymbol{\tau_{12}}$
12	**xy** (9·0,1)	0,2566	$\boldsymbol{\tau_{13}}$
12	**xy**(9·0,1)	0,2566	$\boldsymbol{\tau_{23}}$

Table 12 lists the ranges of the normalized effective and first principal stresses in the matrix evaluated from the ensemble of all 20 sets of grain orientations considered. For an infinitely big, isotropic sample, the values for the three normal load cases, σ_{11}, σ_{22} and σ_{33}, would have to be identical, and the same holds for the three shear load cases. The clear differences within each set of load cases again clearly point out the fact that, due to the relatively small size and fairly small number of volume elements considered, the present work provides approximations only. The range of approximately 4 in terms of the effective stresses and of roughly 10 in terms of the first principal stresses predicted for the three normal stress load cases points out that the local stress fields in the matrix are strongly inhomogeneous due to its grain structure and the anisotropy of the individual grains. A similar picture emerges from the predictions pertaining to the shear load cases. Here, however, the ranges of the normalized stresses tend to be greater, especially for the von Mises equivalent stress, and first principal stresses of the

opposite sign to that corresponding to the applied stress can be seen to occur locally. These results, of course, dovetail with the markedly inhomogeneous microfields evident in Figure 4.15.

Table 12 Minimum and maximum values of integration point von Mises and first principal stresses in runs for matrix alone (configuration 0), normalized with respect to applied stresses

Load Case	Variable	Min/Max
σ_{11}	σ_{vm}	0,47/2,08
	σ_{I}	0,23/2,19
σ_{22}	σ_{vm}	0,44/2,20
	σ_{I}	0,14/2,27
σ_{33}	σ_{vm}	0,47/2,02
	σ_{I}	0,21/1,91
τ_{12}	σ_{vm}	0,78/3,43
	σ_{I}	-0,58/2,97
τ_{13}	σ_{vm}	0,60/4,42
	σ_{I}	-0,25/3,54
τ_{23}	σ_{vm}	0,60/4,54
	σ_{I}	-0,16/3,04

4.2. Material set (a) – T300 carbon fibers

The first set of results pertains to the matrix reinforced with aligned, continuous T-300 carbon fibers. Due to the markedly transversally isotropic behavior of the fibers, the elastic contrasts between them and the isotropized matrix are approximately 18 for the axial Young's modulus, 3 for the axial shear modulus and approximately unity for the transverse Young's and shear moduli.

4.2.1. Configuration Ia

Homogenized elasticity tensors

Table 13 presents the effective elasticity tensors predicted by one-step and by two-step homogenization for fibers positioned at the centers of the matrix grains, configuration

Ia. In order to facilitate comparisons between the results of the one-step and two-step models the component-wise relative differences $(E_{ij}^{1E}-E_{ij}^{2E})/E_{ij}^{1E}$ are also evaluated for the "transversally isotropic terms" of the elasticity tensor. Finally, the transversally isotropic elasticity tensor (1ET) closest to the ensemble averaged homogenized result (1E) is given.

Table 13 Elasticity tensors predicted for T-300 fibers embedded at the centers of the matrix grains (configuration Ia, units of GPa)

Ensemble averaged effective elasticity tensor (1E: 1-step homogenization, fibers in inhomogeneous matrix)

$$\begin{pmatrix} 18{,}170 & 8{,}470 & 8{,}317 & -0{,}057 & -0{,}069 & 0{,}020 \\ 8{,}470 & 18{,}090 & 8{,}408 & 0{,}148 & 0{,}045 & 0{,}014 \\ 8{,}317 & 8{,}408 & 72{,}382 & -0{,}113 & 0{,}030 & -0{,}040 \\ -0{,}057 & 0{,}148 & -0{,}113 & 6{,}327 & -0{,}037 & 0{,}039 \\ -0{,}069 & 0{,}045 & 0{,}030 & -0{,}037 & 6{,}202 & -0{,}045 \\ 0{,}020 & 0{,}014 & -0{,}040 & 0{,}039 & -0{,}045 & 4{,}961 \end{pmatrix}$$

Effective elasticity tensor (2E: 2-step homogenization, fibers in homogenized matrix)

$$\begin{pmatrix} 18{,}174 & 8{,}449 & 8{,}335 & 0{,}027 & -0{,}067 & -0{,}048 \\ 8{,}449 & 18{,}097 & 8{,}431 & 0{,}013 & 0{,}048 & 0{,}131 \\ 8{,}335 & 8{,}430 & 72{,}404 & -0{,}045 & 0{,}024 & -0{,}097 \\ 0{,}027 & 0{,}013 & -0{,}045 & 5{,}994 & -0{,}050 & 0{,}041 \\ -0{,}067 & 0{,}048 & 0{,}024 & -0{,}050 & 6{,}217 & -0{,}030 \\ -0{,}048 & 0{,}131 & -0{,}097 & 0{,}041 & -0{,}030 & 5{,}254 \end{pmatrix}$$

Relative difference: $(E_{ij}^{1E}-E_{ij}^{2E})/E_{ij}^{1E}$

$$\begin{pmatrix} -0{,}000 & 0{,}002 & -0{,}002 & - & - & - \\ 0{,}002 & -0{,}000 & -0{,}003 & - & - & - \\ -0{,}002 & -0{,}003 & -0{,}000 & - & - & - \\ - & - & - & 0{,}053 & - & - \\ - & - & - & - & -0{,}002 & - \\ - & - & - & - & - & -0{,}059 \end{pmatrix}$$

Closest transversally isotropic elasticity tensor to ensemble averaged effective elasticity tensor (1ET)

$$\begin{pmatrix} 18{,}194 & 8{,}406 & 8{,}363 & 0 & 0 & 0 \\ 8{,}406 & 18{,}194 & 8{,}363 & 0 & 0 & 0 \\ 8{,}363 & 8{,}363 & 72{,}382 & 0 & 0 & 0 \\ 0 & 0 & 0 & 6{,}263 & 0 & 0 \\ 0 & 0 & 0 & 0 & 6{,}263 & 0 \\ 0 & 0 & 0 & 0 & 0 & 4{,}894 \end{pmatrix}$$

As expected on the basis of the phase geometry and of the fibers' material behavior, the predicted macroscopic elasticity tensors fairly closely approach transverse isotropy, the E_{33} (axial) component having approximately 4 times the value of the E_{11} and E_{22} (transverse) components. The shear components show much smaller differences on account of the low elastic contrast in shear. The relative differences between the single-step and two-step results can be seen to be less than 6% for the tensor elements connected by transversally isotropic behavior and they are very small for the upper left-hand sub-matrix describing normal loading.

Ranges of microfields in matrix and fibers

Obviously, large amounts of data on the microfields of volume elements can be generated by and extracted from the unit cell models. For the present configuration, T-300 fibers at the centers of the matrix grains, the ranges of the predicted von Mises stresses, $\sigma_{vm,}$ and first principal stresses, $\sigma_{I,}$ in fiber and matrix were evaluated at the integration points; the results are juxtaposed for one-step and two-step homogenization models.

Table 14 Minimum and maximum values of integration point von Mises and first principal stresses predicted by one-step (configuration Ia/1) and two-step (configuration Ia/2) models with T-300 fibers at grain centers

Load Case	Variable	Min/Max one-step	Min/Max two-step
σ_{11}	σ_{vm} fiber	1,40/1,88	1,61/1,62
	σ_{I} fiber	0,74/1,23	0,97/0,98
	σ_{vm} matrix	0,36/1,89	0,73/0,97
	σ_{I} matrix	0,37/2,11	0,97/1,05
σ_{22}	σ_{vm} fiber	1,41/1,96	1,64/1,66
	σ_{I} fiber	0,75/1,23	0,97/0,98
	σ_{vm} matrix	0,35/1,95	0,74/0,96
	σ_{I} matrix	0,30/2,17	0,96/1,06
σ_{33}	σ_{vm} fiber	3,39/3,52	3,45/3,45
	σ_{I} fiber	3,39/3,51	3,44/3,44
	σ_{vm} matrix	0,09/0,34	0,18/0,19
	σ_{I} matrix	0,05/0.33	0,19/0,19

τ_{12}	σ_{vm} fiber	1,42/2,35	1,76/1,78
	σ_I fiber	0,62/1,61	1,01/1,02
	σ_{vm} matrix	0,59/3,59	1,68/1,77
	σ_I matrix	-0,41/3,01	0,92/1,04
τ_{13}	σ_{vm} fiber	1,57/2,94	2,21/2,23
	σ_I fiber	0,80/1,90	1,27/1,28
	σ_{vm} matrix	0,36/3,56	0,92/2,19
	σ_I matrix	-0,12/2,85	0,52/1,27
τ_{23}	σ_{vm} fiber	1,56/2,90	2,25/2,27
	σ_I fiber	0,83/1,80	1,31/1,33
	σ_{vm} matrix	0,42/3,70	0,90/2,24
	σ_I matrix	-0,14/2,45	0,52/1,29

The above data shows a clear tendency for the ranges of the predicted, normalized von Mises and first principal stresses to be much larger for one-step than for two-step homogenization, a behavior that is most marked for the case of axial unidirectional loading, for which the stress fluctuations in homogeneous phases (and thus for the two-step procedure) nearly vanish. Similar, though less extreme, effects are evident for axial shear loading. In both these cases, the inhomogeneous matrix behavior accounted for in the one-step, but not in the two-step models also induces fluctuations in the stress fields in the fibers. As a consequence, when damage mechanisms are assumed to act at a local level, two-step model will underestimate the susceptibility of composites to damage.

4.2.2. Configuration IIa

Homogenized elasticity tensors

Results on the effective behavior of configuration IIa, in which T-300 fibers are positioned at the triple points of the matrix grains, comprise the effective elasticity tensors obtained with one-step and two-step homogenization as well as the closest transversally isotropic elasticity tensor to the former one and are shown in Table 15. The results are in fairly good agreement with the ones given in Table 13 for the fibers in

the “centers of the grain” configuration. This agreement is closer for the results of two-step homogenization than for the one-step predictions.

Table 15 Elasticity tensors predicted for T-300 fibers embedded at the triple points of the matrix grains (configuration IIa, units of GPa)

Ensemble averaged effective elasticity tensor (1E: 1-step homogenization, fibers in inhomogeneous matrix)

$$\begin{pmatrix} 18{,}169 & 8{,}459 & 8{,}321 & -0{,}039 & -0{,}042 & 0{,}050 \\ 8{,}459 & 18{,}093 & 8{,}409 & 0{,}156 & 0{,}045 & -0{,}010 \\ 8{,}321 & 8{,}409 & 72{,}399 & -0{,}143 & -0{,}002 & -0{,}046 \\ -0{,}039 & 0{,}156 & -0{,}143 & 6{,}378 & -0{,}032 & 0{,}044 \\ -0{,}042 & 0{,}045 & -0{,}002 & -0{,}032 & 6{,}263 & -0{,}021 \\ 0{,}050 & -0{,}010 & -0{,}046 & 0{,}044 & -0{,}021 & 4{,}965 \end{pmatrix}$$

Effective elasticity tensor (2E: 2-step, fibers in homogenized matrix)

$$\begin{pmatrix} 18{,}176 & 8{,}450 & 8{,}336 & 0{,}027 & -0{,}068 & -0{,}048 \\ 8{,}450 & 18{,}095 & 8{,}430 & 0{,}013 & 0{,}048 & 0{,}131 \\ 8{,}336 & 8{,}430 & 72{,}405 & -0{,}045 & 0{,}024 & -0{,}097 \\ 0{,}027 & 0{,}013 & -0{,}045 & 5{,}998 & -0{,}050 & 0{,}041 \\ -0{,}068 & 0{,}048 & 0{,}024 & -0{,}050 & 6{,}221 & -0{,}030 \\ -0{,}048 & 0{,}131 & -0{,}097 & 0{,}041 & -0{,}030 & 5{,}254 \end{pmatrix}$$

Closest transversally isotropic elasticity tensor to ensemble averaged effective elasticity tensor (1ET)

$$\begin{pmatrix} 18{,}194 & 8{,}395 & 8{,}366 & 0 & 0 & 0 \\ 8{,}395 & 18{,}194 & 8{,}366 & 0 & 0 & 0 \\ 8{,}366 & 8{,}366 & 72{,}398 & 0 & 0 & 0 \\ 0 & 0 & 0 & 6{,}319 & 0 & 0 \\ 0 & 0 & 0 & 0 & 6{,}319 & 0 \\ 0 & 0 & 0 & 0 & 0 & 4{,}899 \end{pmatrix}$$

Ranges of microfields in matrix and fibers

Table 16 lists the minimum and maximum values of the von Mises and first principal stresses evaluated at the integration points of matrix and T-300 fibers for configuration IIa. Comparing tables Table 14 and Table 16 shows that these predictions – like the ones for the macroscopic elastic responses – do not differ markedly for the two positions of the fibers considered here. Especially the results obtained by two-step homogenization for the two configurations are close, which is not surprising because differences in this case may be expected to be mainly due to meshing effects. As in the case of configuration Ia, the ranges obtained by two-step homogenization are sub-

intervals of the ones predicted by the one-step model, i.e., the one-step models predict considerably higher fluctuations of the local fields, which is not surprising in view of the fluctuations in the matrix induced by the resolved grain-level behavior.

Table 16 Maximum and minimum values of integration point von Mises and first principal stresses predicted by one-step (configuration IIa/1) and two-step (configuration IIa/2) models with T-300 fibers at grain centers

Load Case	Variable	Min/Max one-step	Min/Max two-step
σ_{11}	σ_{vm} fiber	1,22/2,08	1,60/1,63
	σ_I fiber	0,43/1,60	0,96/0,99
	σ_{vm} matrix	0,36/1,74	0,71/0,98
	σ_I matrix	0,19/2,03	0,97/1,06
σ_{22}	σ_{vm} fiber	1,21/2,20	1,65/1,66
	σ_I fiber	0,42/1,69	0,97/0,99
	σ_{vm} matrix	0,35/1,77	0,73/0,98
	σ_I matrix	0,10/1,95	0,97/1,06
σ_{33}	σ_{vm} fiber	3,37/3,55	3,45/3,45
	σ_I fiber	3,37/3,52	3,44/3,44
	σ_{vm} matrix	0,09/0,36	0,18/0,19
	σ_I matrix	0,04/0,34	0,18/0,19
τ_{12}	σ_{vm} fiber	1,26/3,06	1,75/1,78
	σ_I fiber	0,07/2,41	1,00/1,03
	σ_{vm} matrix	0,88/3,28	1,67/1,77
	σ_I matrix	-0,53/2,92	0,91/1,04
τ_{13}	σ_{vm} fiber	1,02/4,44	2,07/2,41
	σ_I fiber	0,36/3,00	1,19/1,39
	σ_{vm} matrix	0,44/5,90	0,94/2,41
	σ_I matrix	-0,19/4,30	0,54/1,40
τ_{23}	σ_{vm} fiber	1,15/4,36	2,07/2,43
	σ_I fiber	0,45/2,93	1,21/1,42
	σ_{vm} matrix	0,30/5,79	0,81/2,27
	σ_I matrix	-0,17/3,41	0,46/1,30

4.2.3. Effective moduli

A compact comparison between the different models can be given by considering transversally isotropic macroscopic responses. For the one-step homogenization scheme these can be extracted from the closest transversally isotropic elasticity tensors, compare tables Table 13 and Table 15 (results **Ia/1ET** and **IIa/1ET**). Transversally isotropic moduli can be obtained in an analogous way from the transversally isotropic tensors closest to the two-step elasticity tensors listed in the above tables, giving rise to results **Ia/2ET** and **IIa/2ET**. In addition, two-step homogenization may be carried out with the isotropized matrix behavior listed in Table 10, leading to the sets of moduli **Ia/2E**I and **IIa/2EI**. Finally, the isotropized elastic moduli of the matrix can also be inserted into the Hashin-Shtrikman, bounds for composites reinforced by continuous aligned fibers to give lower (**HSL/EI**) and upper (**HSH/EI**) bounds, see [36], [37].

Table 17 Effective, transversally isotropic moduli predicted for models with T-300 fibers

	E_A	E_T	ν_A	ν_T	G_A	G_T
HSL/EI	67.544	14.258	0.310	0.425	6.032	5.000
HSH/EI	67.548	14.275	0.311	0.426	6.263	5.001
Ia/1ET	67.123	14.015	0.314	0.432	6.263	4.894
IIa/1ET	67.133	14.024	0.315	0.431	6.319	4.899
Ia/2ET	67.117	14.314	0.315	0.419	6.104	5.042
IIa/2ET	67.117	14.314	0.315	0.419	6.108	5.043
Ia/2EI	67.543	14.255	0.310	0.425	6.034	5.001
IIa/2EI	67.544	14.255	0.310	0.425	6.038	5.001

The Hashin-Shtrikman bounds given here pertain only to results Ia/2EI and IIa/2EI, which can be seen to either lie within the bounds, or, in the case of E_T, to very closely approach the lower bound. The moduli corresponding to the closest transversally isotropic tensors from the one-step and two-step results obtained for the inhomogeneous matrix mostly fall outside the bounds, the largest relative difference of some 2,2% occurring for the transverse shear modulus of configuration Ia/1ET. Interestingly, the overall axial Young's moduli predicted by models Ia/1ET, IIa/1ET, Ia/2ET and IIa/2ET all lie below the Hashin-Shtrikman bounds obtained with the isotropized matrix. The macroscopic transverse Young's and shear moduli obtained with the one-step models lie

below the corresponding lower Hashin-Shtrikman bounds, whereas those extracted from the two-step models are above the upper bounds.

4.3. Material set (b) – P-100 carbon fibers

On account of the marked anisotropy of the P-100 fibers, the elastic contrasts between them and the isotropized matrix are approximately 58, 0,5, 1,3, and 0,4 for the axial Young's modulus, the transverse Young's modulus, the axial shear modulus and the transverse shear modulus, respectively.

4.3.1. Configuration Ib

Homogenized elasticity tensors

As expected, the effective elasticity tensors predicted for this combination of constituents by both the one-step and the two-step models are highly anisotropic, as can be seen from Table 18. Qualitatively, they are quite similar to the predictions obtained for configuration Ia.

Table 18 Elasticity tensors predicted for P-100 fibers embedded at the centers of the matrix grains (configuration Ib, units of GPa)

Ensemble averaged effective elasticity tensor (1E: 1-step homogenization, fibers in inhomogeneous matrix)

$$\begin{pmatrix} 17{,}987 & 10{,}505 & 9{,}371 & -0{,}041 & -0{,}069 & 0{,}020 \\ 10{,}505 & 17{,}924 & 9{,}448 & 0{,}137 & 0{,}038 & 0{,}015 \\ 9{,}371 & 9{,}448 & 205{,}283 & -0{,}115 & 0{,}031 & -0{,}033 \\ -0{,}041 & 0{,}137 & -0{,}115 & 6{,}889 & -0{,}041 & 0{,}037 \\ -0{,}069 & 0{,}038 & 0{,}031 & -0{,}041 & 6{,}755 & -0{,}037 \\ 0{,}020 & 0{,}015 & -0{,}033 & 0{,}037 & -0{,}037 & 3{,}819 \end{pmatrix}$$

Effective elasticity tensor (2E: 2-step homogenization, fibers in homogenized matrix)

$$\begin{pmatrix} 18{,}477 & 10{,}960 & 9{,}576 & 0{,}029 & -0{,}065 & -0{,}027 \\ 10{,}960 & 18{,}398 & 9{,}650 & 0{,}015 & 0{,}043 & 0{,}103 \\ 9{,}576 & 9{,}650 & 205{,}370 & -0{,}046 & 0{,}024 & -0{,}081 \\ 0{,}029 & 0{,}015 & -0{,}046 & 6{,}580 & -0{,}056 & 0{,}039 \\ -0{,}065 & 0{,}043 & 0{,}024 & -0{,}056 & 6{,}828 & -0{,}027 \\ -0{,}027 & 0{,}103 & -0{,}081 & 0{,}039 & -0{,}027 & 4{,}038 \end{pmatrix}$$

Relative difference: $(E_{ij}^{1E}-E_{ij}^{2E})/E_{ij}^{1E}$

$$\begin{pmatrix} -0{,}027 & -0{,}043 & -0{,}022 & - & - & - \\ -0{,}043 & -0{,}026 & -0{,}021 & - & - & - \\ -0{,}022 & -0{,}021 & -0{,}000 & - & - & - \\ - & - & - & 0{,}045 & - & - \\ - & - & - & - & -0{,}010 & - \\ - & - & - & - & - & -0{,}057 \end{pmatrix}$$

Closest transversally isotropic elasticity tensor to ensemble averaged effective elasticity tensor (1ET)

$$\begin{pmatrix} 18{,}002 & 10{,}459 & 9{,}410 & 0 & 0 & 0 \\ 10{,}459 & 18{,}002 & 9{,}410 & 0 & 0 & 0 \\ 9{,}410 & 9{,}410 & 205{,}283 & 0 & 0 & 0 \\ 0 & 0 & 0 & 6{,}821 & 0 & 0 \\ 0 & 0 & 0 & 0 & 6{,}821 & 0 \\ 0 & 0 & 0 & 0 & 0 & 3{,}771 \end{pmatrix}$$

4.3.2. Configuration IIb

Homogenized elasticity tensors

Table 19 presents the one-step and two-step predictions obtained for the elastic tensors of the unit cells describing fibers positioned at the triple points of the grains. Comparing these elasticity tensors with those obtained for the "fibers at grain centers" models (Table 18) indicates a trend towards somewhat lower stiffness for the former model.

Table 19 Elasticity tensors predicted for P-100 fibers embedded at the triple points of the matrix grains (configuration IIb, units of GPa)

Ensemble averaged effective elasticity tensor (1E: 1-step homogenization, fibers in inhomogeneous matrix)

$$\begin{pmatrix} 15{,}320 & 7{,}779 & 8{,}248 & -0{,}053 & -0{,}059 & 0{,}019 \\ 7{,}779 & 15{,}256 & 8{,}330 & 0{,}129 & 0{,}043 & 0{,}011 \\ 8{,}248 & 8{,}330 & 204{,}817 & -0{,}109 & 0{,}025 & -0{,}036 \\ -0{,}053 & 0{,}129 & -0{,}109 & 6{,}645 & -0{,}034 & 0{,}036 \\ -0{,}059 & 0{,}043 & 0{,}025 & -0{,}034 & 6{,}514 & -0{,}040 \\ 0{,}019 & 0{,}011 & -0{,}036 & 0{,}036 & -0{,}040 & 3{,}850 \end{pmatrix}$$

Effective elasticity tensor (2E: 2-step homogenization, fibers in homogenized matrix)

$$\begin{pmatrix} 15{,}350 & 7{,}771 & 8{,}281 & 0{,}026 & -0{,}059 & -0{,}033 \\ 7{,}771 & 15{,}290 & 8{,}364 & 0{,}013 & 0{,}043 & 0{,}100 \\ 8{,}281 & 8{,}364 & 204{,}82 & -0{,}045 & 0{,}024 & -0{,}082 \\ 0{,}026 & 0{,}013 & -0{,}045 & 6{,}269 & -0{,}052 & 0{,}036 \\ -0{,}059 & 0{,}043 & 0{,}024 & -0{,}052 & 6{,}503 & -0{,}027 \\ -0{,}033 & 0{,}100 & -0{,}082 & 0{,}036 & -0{,}027 & 4{,}081 \end{pmatrix}$$

Closest transversally isotropic elasticity tensor to ensemble averaged effective elasticity tensor (1ET)

$$\begin{pmatrix} 15{,}335 & 7{,}733 & 8{,}290 & 0 & 0 & 0 \\ 7{,}733 & 15{,}335 & 8{,}290 & 0 & 0 & 0 \\ 8{,}290 & 8{,}290 & 204{,}817 & 0 & 0 & 0 \\ 0 & 0 & 0 & 6{,}579 & 0 & 0 \\ 0 & 0 & 0 & 0 & 6{,}578 & 0 \\ 0 & 0 & 0 & 0 & 0 & 3{,}801 \end{pmatrix}$$

4.3.3. Effective moduli

Table 20 provides comparisons between the elastic moduli corresponding to the transversally isotropic tensors closest to the one-step and two-step results listed in tables Table 18 and Table 19 (Ib/1ET, Ib/2ET, IIb/1ET, IIb/2ET) as well as to two-step results (Ib/2EI, IIb/2EI) and Hashin-Shtrikman bounds (HSL/EI, HSH/EI) obtained with isotropized homogenized matrix properties.

Table 20 Effective, transversally isotropic moduli predicted for models with P-100 fibers

	E_A	E_T	ν_A	ν_T	G_A	G_T
HSL/EI	199.25	11.486	0.355	0.456	6.300	3.894
HSH/EI	199.25	12.004	0.357	0.587	6.754	4.089
Ib/1ET	199.06	11.847	0.331	0.571	6.821	3.771
IIb/1ET	198.86	11.351	0.359	0.493	6.578	3.801
Ib/2ET	199.08	12.209	0.327	0.571	6.703	3.885
IIb/2ET	198.82	11.625	0.360	0.481	6.384	3.924
Ib/2EI	199.51	12.146	0.322	0.576	6.621	3.854
IIb/2EI	199.25	11.569	0.355	0.486	6.309	3.893

The agreement between the results obtained with the “fibers at grain centers” and the “fibers at triple points” geometries is not quite as close as for the composites reinforced by T-300 fibers (Table 17), and the two-step results obtained with the isotropized matrix behavior (Ib/2EI, IIb/2EI) show stronger violations of the Hashin-Shtrikman bounds.

The differences between one-step and two-step predictions for the elastic moduli exceed 3% in the cases of the transverse Young's and shear moduli.

4.4. Material set (c) – Nextel fibers

The elastic contrasts between the isotropic Nextel 312 fibers and the homogenized, isotropized matrix are 11,7 in terms of the Young's moduli and 12,5 in terms of the shear moduli.

4.4.1. Configuration Ic

Homogenized elasticity tensors

Table 21 gives the elastic tensors predicted for the "fibers at grain centers" case. As expected, the Nextel fibers lead to a less anisotropic behavior than the carbon fibers underlying sections 4.2 and 4.3, the ratio between the predicted diagonal elements of the elasticity tensor, E_{33}/E_{11}, being of the order two rather than exceeding ten, as in Table 18. The relative difference in the transversally isotropic elements of the elasticity tensor, exceeds 6% in the axial shear component E_{44}. The latter behavior is due to considerable deviation of the shear terms from transverse isotropy in the two-step result Ic/2E.

Table 21 Elasticity tensors predicted for Nextel fibers embedded at the centers of the matrix grains (configuration Ic, units of GPa)

Ensemble averaged effective elasticity tensor (1E: 1-step homogenization, fibers in inhomogeneous matrix)

$$\begin{pmatrix} 27{,}466 & 13{,}690 & 13{,}189 & -0{,}070 & -0{,}097 & 0{,}036 \\ 13{,}690 & 27{,}304 & 13{,}285 & 0{,}243 & 0{,}055 & 0{,}026 \\ 13{,}189 & 13{,}285 & 55{,}880 & -0{,}105 & 0{,}028 & -0{,}044 \\ -0{,}070 & 0{,}243 & -0{,}105 & 7{,}929 & -0{,}045 & 0{,}051 \\ -0{,}097 & 0{,}055 & 0{,}028 & -0{,}045 & 7{,}749 & -0{,}073 \\ 0{,}036 & 0{,}026 & -0{,}044 & 0{,}051 & -0{,}073 & 7{,}051 \end{pmatrix}$$

Effective elasticity tensor (2E: 2-step homogenization, fibers in homogenized matrix)

$$\begin{pmatrix} 27{,}516 & 13{,}789 & 13{,}229 & 0{,}033 & -0{,}095 & -0{,}074 \\ 13{,}789 & 27{,}268 & 13{,}306 & 0{,}019 & 0{,}059 & 0{,}205 \\ 13{,}229 & 13{,}306 & 55{,}814 & -0{,}048 & 0{,}022 & -0{,}113 \\ 0{,}033 & 0{,}019 & -0{,}048 & 7{,}419 & -0{,}064 & 0{,}052 \\ -0{,}095 & 0{,}059 & 0{,}022 & -0{,}064 & 7{,}706 & -0{,}043 \\ -0{,}074 & 0{,}205 & -0{,}113 & 0{,}052 & -0{,}043 & 7{,}454 \end{pmatrix}$$

Relative difference: $(E_{ij}^{1E}-E_{ij}^{2E})/E_{ij}^{1E}$

$$\begin{pmatrix} -0{,}002 & -0{,}007 & -0{,}003 & - & - & - \\ -0{,}007 & 0{,}001 & -0{,}002 & - & - & - \\ -0{,}003 & -0{,}002 & 0{,}001 & - & - & - \\ - & - & - & 0{,}064 & - & - \\ - & - & - & - & 0{,}006 & - \\ - & - & - & - & - & -0{,}057 \end{pmatrix}$$

Closest transversally isotropic elasticity tensor to ensemble averaged effective elasticity tensor (1ET)

$$\begin{pmatrix} 27{,}485 & 13{,}590 & 13{,}238 & 0 & 0 & 0 \\ 13{,}590 & 27{,}485 & 13{,}238 & 0 & 0 & 0 \\ 13{,}238 & 13{,}238 & 55{,}879 & 0 & 0 & 0 \\ 0 & 0 & 0 & 7{,}837 & 0 & 0 \\ 0 & 0 & 0 & 0 & 7{,}837 & 0 \\ 0 & 0 & 0 & 0 & 0 & 6{,}947 \end{pmatrix}$$

4.4.2. Configuration IIc

Homogenized elasticity tensors

The results obtained for the "fibers at triple points" geometry with the Nextel fibers, which are listed in Table 22, show a qualitatively very similar behavior to the predictions given in Table 21, albeit with slightly different numerical values.

Table 22 Elasticity tensors predicted for Nextel fibers embedded at the triple points of the matrix grains (configuration IIc, units of GPa)

Ensemble averaged effective elasticity tensor (1E: 1-step homogenization, fibers in inhomogeneous matrix)

$$\begin{pmatrix} 27{,}630 & 13{,}677 & 13{,}169 & -0{,}093 & -0{,}104 & -0{,}040 \\ 13{,}677 & 27{,}476 & 13{,}282 & 0{,}228 & 0{,}071 & 0{,}098 \\ 13{,}169 & 13{,}282 & 55{,}910 & -0{,}086 & 0{,}018 & -0{,}040 \\ -0{,}093 & 0{,}228 & -0{,}086 & 8{,}106 & -0{,}031 & 0{,}064 \\ -0{,}104 & 0{,}071 & 0{,}018 & -0{,}031 & 7{,}949 & -0{,}097 \\ -0{,}040 & 0{,}098 & -0{,}040 & 0{,}064 & -0{,}097 & 7{,}132 \end{pmatrix}$$

Effective elasticity tensor (2E: 2-step homogenization, fibers in homogenized matrix)

$$\begin{pmatrix} 27{,}528 & 13{,}801 & 13{,}235 & 0{,}035 & -0{,}102 & -0{,}064 \\ 13{,}801 & 27{,}395 & 13{,}341 & 0{,}018 & 0{,}065 & 0{,}020 \\ 13{,}235 & 13{,}341 & 55{,}824 & -0{,}048 & 0{,}022 & -0{,}106 \\ 0{,}035 & 0{,}018 & -0{,}048 & 7{,}461 & -0{,}064 & 0{,}059 \\ -0{,}102 & 0{,}065 & 0{,}022 & -0{,}064 & 7{,}747 & -0{,}042 \\ -0{,}064 & 0{,}020 & -0{,}106 & 0{,}059 & -0{,}042 & 7{,}480 \end{pmatrix}$$

Closest transversally isotropic elasticity tensor to ensemble averaged effective elasticity tensor (1ET)

$$\begin{pmatrix} 27{,}647 & 13{,}582 & 13{,}226 & 0 & 0 & 0 \\ 13{,}582 & 27{,}647 & 13{,}226 & 0 & 0 & 0 \\ 13{,}226 & 13{,}226 & 55{,}909 & 0 & 0 & 0 \\ 0 & 0 & 0 & 8{,}025 & 0 & 0 \\ 0 & 0 & 0 & 0 & 8{,}025 & 0 \\ 0 & 0 & 0 & 0 & 0 & 7{,}032 \end{pmatrix}$$

4.4.3. Effective moduli

The effective, transversally isotropic moduli predicted for composites reinforced by Nextel fibers are presented in Table 23. In analogy to tables Table 17 and Table 20, results pertain to the closest transversally isotropic tensors to the one-step and two-step models for both geometrical configurations as well as to unit cell results and bounds obtained on the basis of the isotropized matrix behavior.

Table 23 Effective, transversally isotropic moduli predicted for models with Nextel fibers

	E_A	E_T	ν_A	ν_T	G_A	G_T
HSL/EI	47.691	20.104	0.299	0.222	7.457	7.031
HSH/EI	47.799	30.374	0.318	0.539	13.288	11.225
Ic/1ET	47.347	19.860	0.322	0.429	7.837	6.947
IIc/1ET	47.423	20.061	0.321	0.426	8.025	7.032
Ic/2ET	47.726	20.022	0.322	0.422	7.561	7.118
IIc/2ET	47.264	20.286	0.322	0.419	7.602	7.146
Ic/2EI	47.691	20.131	0.317	0.428	7.460	7.048
IIc/2EI	47.691	20.197	0.317	0.427	7.501	7.075

The relative difference between the one-step and two-step results reaches 5% in the predictions for the axial shear moduli of configuration IIc, with the two-step models giving higher effective properties in all transverse properties. The numerical results evaluated for isotropized matrix behavior all fall within the Hashin-Shtrikman bounds.

The one-step results, Ic/1ET and, less clearly, IIc/1ET, show a tendency to be on the low side for E_A, E_T and G_T, and on the high side for G_A.

4.5. Material set (d) – compliant inhomogeneities

The elastic contrasts between the hypothetical compliant inhomogeneities and the isotropized matrix are 0,05 for the Young's moduli and 0,06 for the shear moduli.

4.5.1. Configuration Id

Homogenized elasticity tensors

The compliant inhomogeneities lead to an increased influence of the matrix behavior on the overall elastic response, compare Table 24. The maximum relative difference between one-step and two-step results occurs in the transverse shear components of the tensors and reaches 8%, and the components of the one-step tensor tend to be smaller than the corresponding ones of the two-step tensor.

Table 24 Elasticity tensors predicted for compliant inhomogeneities embedded at the centers of the matrix grains (configuration Id, units of GPa)

Ensemble averaged effective elasticity tensor (1E: 1-step homogenization, compliant inhomogeneities with inhomogeneous matrix)

$$\begin{pmatrix} 9{,}446 & 4{,}099 & 4{,}531 & -0{,}031 & -0{,}036 & 0{,}010 \\ 4{,}099 & 9{,}357 & 4{,}585 & 0{,}090 & 0{,}019 & 0{,}007 \\ 4{,}531 & 4{,}585 & 12{,}441 & -0{,}079 & 0{,}020 & -0{,}032 \\ -0{,}031 & 0{,}090 & -0{,}079 & 3{,}255 & -0{,}018 & 0{,}018 \\ -0{,}036 & 0{,}019 & 0{,}020 & -0{,}018 & 3{,}183 & -0{,}026 \\ 0{,}010 & 0{,}007 & -0{,}032 & 0{,}018 & -0{,}026 & 2{,}714 \end{pmatrix}$$

Effective elasticity tensor (2E: 2-step homogenization, compliant inhomogeneities in homogenized matrix)

$$\begin{pmatrix} 9{,}720 & 4{,}176 & 4{,}696 & 0{,}007 & -0{,}035 & -0{,}039 \\ 4{,}176 & 9{,}533 & 4{,}718 & 0{,}002 & 0{,}020 & 0{,}050 \\ 4{,}696 & 4{,}718 & 12{,}708 & -0{,}039 & 0{,}016 & -0{,}085 \\ 0{,}007 & 0{,}002 & -0{,}039 & 3{,}074 & -0{,}027 & 0{,}017 \\ -0{,}035 & 0{,}020 & 0{,}016 & -0{,}027 & 3{,}193 & -0{,}016 \\ -0{,}039 & 0{,}050 & -0{,}085 & 0{,}017 & -0{,}016 & 2{,}941 \end{pmatrix}$$

Relative difference: $(E_{ij}^{1E}-E_{ij}^{2E})/E_{ij}^{1E}$

$$\begin{pmatrix} -0{,}029 & -0{,}019 & -0{,}036 & - & - & - \\ -0{,}019 & -0{,}019 & -0{,}029 & - & - & - \\ -0{,}036 & -0{,}029 & -0{,}021 & - & - & - \\ - & - & - & 0{,}056 & - & - \\ - & - & - & - & -0{,}003 & - \\ - & - & - & - & - & -0{,}084 \end{pmatrix}$$

Closest transversally isotropic elasticity tensor to ensemble averaged effective elasticity tensor (1ET)

$$\begin{pmatrix} 9{,}432 & 4{,}069 & 4{,}559 & 0 & 0 & 0 \\ 4{,}069 & 9{,}432 & 4{,}559 & 0 & 0 & 0 \\ 4{,}559 & 4{,}559 & 12{,}440 & 0 & 0 & 0 \\ 0 & 0 & 0 & 3{,}218 & 0 & 0 \\ 0 & 0 & 0 & 0 & 3{,}218 & 0 \\ 0 & 0 & 0 & 0 & 0 & 2{,}682 \end{pmatrix}$$

4.5.2. Configuration IId

Homogenized elasticity tensors

The effective elasticity tensors obtained by placing the compliant inhomogeneities at the triple points of the matrix grains, which are given in Table 25, show the expected qualitatively similar behavior to Table 24.

Table 25 Elasticity tensors predicted for compliant inhomogeneities embedded at the triple points of the matrix grains (configuration IId, units of GPa)

Ensemble averaged effective elasticity tensor (1E: 1-step homogenization, inhomogeneities in inhomogeneous matrix)

$$\begin{pmatrix} 9{,}251 & 4{,}007 & 4{,}490 & -0{,}024 & -0{,}039 & 0{,}012 \\ 4{,}007 & 9{,}220 & 4{,}572 & 0{,}086 & 0{,}025 & 0{,}007 \\ 4{,}490 & 4{,}572 & 12{,}303 & -0{,}083 & 0{,}022 & -0{,}033 \\ -0{,}024 & 0{,}086 & -0{,}083 & 3{,}170 & -0{,}018 & 0{,}021 \\ -0{,}039 & 0{,}025 & 0{,}022 & -0{,}018 & 3{,}103 & -0{,}020 \\ 0{,}012 & 0{,}007 & -0{,}033 & 0{,}021 & -0{,}020 & 2{,}678 \end{pmatrix}$$

Effective elasticity tensor (2E: 2-step homogenization, inhomogeneities in homogenized matrix)

$$\begin{pmatrix} 9{,}531 & 4{,}088 & 4{,}598 & 0{,}007 & -0{,}038 & -0{,}022 \\ 4{,}088 & 9{,}505 & 4{,}677 & 0{,}001 & 0{,}024 & 0{,}072 \\ 4{,}598 & 4{,}677 & 12{,}659 & -0{,}039 & 0{,}016 & -0{,}071 \\ 0{,}007 & 0{,}001 & -0{,}039 & 3{,}055 & -0{,}026 & 0{,}021 \\ -0{,}038 & 0{,}024 & 0{,}016 & -0{,}026 & 3{,}173 & -0{,}015 \\ -0{,}022 & 0{,}072 & -0{,}071 & 0{,}021 & -0{,}015 & 2{,}927 \end{pmatrix}$$

Closest transversally isotropic elasticity tensor to ensemble averaged effective elasticity tensor (1ET)

$$\begin{pmatrix} 9{,}267 & 3{,}976 & 4{,}532 & 0 & 0 & 0 \\ 3{,}976 & 9{,}267 & 4{,}532 & 0 & 0 & 0 \\ 4{,}532 & 4{,}532 & 12{,}302 & 0 & 0 & 0 \\ 0 & 0 & 0 & 3{,}189 & 0 & 0 \\ 0 & 0 & 0 & 0 & 3{,}189 & 0 \\ 0 & 0 & 0 & 0 & 0 & 2{,}645 \end{pmatrix}$$

4.5.3. Effective moduli

Table 26 lists the predictions obtained for the transversally isotropic effective moduli of material combination (d).

Table 26 Effective, transversally isotropic moduli predicted for models with compliant inhomogeneities

	E_A	E_T	ν_A	ν_T	G_A	G_T
HSL/EI	9,917	2,966	0,304	---	1,478	1,212
HSH/EI	9,929	7,467	0,335	---	3,089	2,827
Id/1ET	9,361	7,021	0,338	0,309	3,218	2,682
IId/1ET	9,201	6,898	0,342	0,304	3,135	2,645
Id/2ET	9,496	7,310	0,341	0,291	3,132	2,830
IId/1ET	9,496	7,262	0,311	0,282	3,113	2,818
Id/2EI	9,929	7,322	0,334	0,304	3,090	2,807
IId/2EI	9,929	7,275	0,334	0,301	3,071	2,795

Due to the low stiffness of the inhomogeneities the Hashin-Shtrikman bounds are rather slack for E_T, G_A and G_T, and the numerical predictions obtained with the isotropized matrix behavior are close to the upper bounds. The predictions for the transverse Young's and shear moduli obtained from the one-step models are clearly lower than the corresponding results of the two step models, the relative differences being of the order or in excess of 5%. The differences in the effective axial moduli are much smaller.

4.6. Material set (e) – quasi-voids

Although these inhomogeneities are not voids in the strict sense of the word, the elastic contrast between them and the isotropized matrix is approximately $4x10^{-8}$, which definitely provides a close approximation to proper pores.

4.6.1. Configuration Ie

Homogenized elasticity tensors

The effective elasticity tensors obtained for quasi-voids positioned at the grain centers are listed in Table 27. For this configuration the maximum difference between elasticity components evaluated with the one-step and two-step approaches exceeds 9%.

Table 27 Elasticity tensors predicted for quasi-voids embedded at the centers of the matrix grains (configuration Ie, units of GPa)

Ensemble averaged elasticity tensor (1E: 1-step homogenization, quasi-voids in inhomogeneous matrix)

$$\begin{pmatrix} 8{,}670 & 3{,}845 & 4{,}282 & -0{,}030 & -0{,}033 & 0{,}010 \\ 3{,}845 & 8{,}575 & 4{,}330 & 0{,}089 & 0{,}017 & 0{,}007 \\ 4{,}282 & 4{,}330 & 12{,}132 & -0{,}076 & 0{,}019 & -0{,}031 \\ -0{,}030 & 0{,}089 & -0{,}076 & 3{,}059 & -0{,}016 & 0{,}016 \\ -0{,}033 & 0{,}017 & 0{,}019 & -0{,}016 & 2{,}988 & -0{,}025 \\ 0{,}010 & 0{,}007 & -0{,}031 & 0{,}016 & -0{,}025 & 2{,}445 \end{pmatrix}$$

Effective elasticity tensor (2E: 2-step homogenization, quasi-voids in homogenized matrix)

$$\begin{pmatrix} 8{,}997 & 3{,}942 & 4{,}468 & 0{,}005 & -0{,}032 & -0{,}038 \\ 3{,}942 & 8{,}784 & 4{,}478 & 0{,}001 & 0{,}017 & 0{,}042 \\ 4{,}468 & 4{,}478 & 12{,}430 & -0{,}039 & 0{,}015 & -0{,}083 \\ 0{,}005 & 0{,}001 & -0{,}039 & 2{,}891 & -0{,}025 & 0{,}015 \\ -0{,}032 & 0{,}017 & 0{,}015 & -0{,}025 & 3{,}005 & -0{,}015 \\ -0{,}038 & 0{,}042 & -0{,}083 & 0{,}015 & -0{,}015 & 2{,}671 \end{pmatrix}$$

Relative difference: $(E_{ij}^{1E}-E_{ij}^{2E})/E_{ij}^{1E}$

$$\begin{pmatrix} -0{,}038 & -0{,}025 & -0{,}043 & - & - & - \\ -0{,}025 & -0{,}024 & -0{,}034 & - & - & - \\ -0{,}043 & -0{,}034 & -0{,}024 & - & - & - \\ - & - & - & 0{,}055 & - & - \\ - & - & - & - & -0{,}005 & - \\ - & - & - & - & - & -0{,}093 \end{pmatrix}$$

Closest transversally isotropic elasticity tensor to ensemble averaged effective elasticity tensor (1ET)

$$\begin{pmatrix} 8{,}649 & 3{,}817 & 4{,}306 & 0 & 0 & 0 \\ 3{,}817 & 8{,}649 & 4{,}306 & 0 & 0 & 0 \\ 4{,}306 & 4{,}306 & 12{,}131 & 0 & 0 & 0 \\ 0 & 0 & 0 & 3{,}023 & 0 & 0 \\ 0 & 0 & 0 & 0 & 3{,}023 & 0 \\ 0 & 0 & 0 & 0 & 0 & 2{,}416 \end{pmatrix}$$

Ranges of microfields in the matrix

Table 28 lists the ranges of the microscopic von Mises and first principal stresses in the matrix evaluated for the six load cases with the one-step and two-step models.

Table 28 Maximum and minimum values of integration point von Mises and first principal stresses predicted by one-step (configuration Ie/ 1) and two-step (configuration Ie/2) models with quasi-voids at grain centers

Load Case	Variable	Min/Max one-step	Min/Max two-step
σ_{11}	σ_{vm}	0,23/4,90	0,48/2,96
	σ_I	-0,18/5,70	-0,10/3,28
σ_{22}	σ_{vm}	0,21/6,02	0,45/3,91
	σ_I	-0,17/6,65	-0,07/4,44
σ_{33}	σ_{vm}	0,65/2,61	1,33/1,33
	σ_I	0,33/2,51	1,33/1,33
τ_{12}	σ_{vm}	0,08/8,00	0,17/4,94
	σ_I	-0,80/8,70	-0,43/5,75
τ_{13}	σ_{vm}	0,09/8,75	0,09/4,65
	σ_I	-0,21/6,01	0,05/2,67
τ_{23}	σ_{vm}	0,05/8,39	0,08/4,44
	σ_I	-0,26/5,55	0,06/2,56

As in the case of reinforcement by T-300 fibers, tables Table 14 and Table 16, the stress ranges predicted by the two-step models are always sub-intervals of the corresponding one-step results. The maximum local stress levels reached in the one-step results tend to be significantly higher compared to the two-step results, indicating that

one-step models may considerably underestimate the susceptibility to brittle or ductile damage in porous media in which the length scales of the matrix grains is comparable to that of the voids.

4.6.2. Configuration IIe

Homogenized elasticity tensors

Table 29 presents the predictions for the effective elasticity tensors pertaining to quasi-voids at the triple points of the matrix grains. Differences in the values of the tensor components compared to the "fibers at grain centers" case, although not very big, are evident.

Table 29 Elasticity tensors predicted for quasi-voids embedded at the triple points of the matrix grains (configuration IIe, units of GPa)

Ensemble averaged effective elasticity tensor (1E: 1-step homogenization, quasi-voids in inhomogeneous matrix)

$$\begin{pmatrix} 8{,}444 & 3{,}724 & 4{,}222 & -0{,}021 & -0{,}037 & 0{,}011 \\ 3{,}724 & 8{,}418 & 4{,}302 & 0{,}082 & 0{,}023 & 0{,}007 \\ 4{,}222 & 4{,}302 & 11{,}968 & -0{,}080 & 0{,}021 & -0{,}031 \\ -0{,}021 & 0{,}082 & -0{,}080 & 2{,}963 & -0{,}016 & 0{,}019 \\ -0{,}037 & 0{,}023 & 0{,}021 & -0{,}016 & 2{,}898 & -0{,}017 \\ 0{,}011 & 0{,}007 & -0{,}031 & 0{,}019 & -0{,}017 & 2{,}411 \end{pmatrix}$$

Effective elasticity tensor (2E: 2-step homogenization, quasi-voids in homogenized matrix)

$$\begin{pmatrix} 8{,}763 & 3{,}831 & 4{,}348 & 0{,}006 & -0{,}036 & -0{,}018 \\ 3{,}831 & 8{,}743 & 4{,}425 & 0{,}000 & 0{,}022 & 0{,}067 \\ 4{,}348 & 4{,}425 & 12{,}367 & -0{,}039 & 0{,}016 & -0{,}067 \\ 0{,}006 & 0{,}000 & -0{,}039 & 2{,}865 & -0{,}025 & 0{,}020 \\ -0{,}036 & 0{,}022 & 0{,}016 & -0{,}025 & 2{,}977 & -0{,}013 \\ -0{,}018 & 0{,}067 & -0{,}067 & 0{,}020 & -0{,}013 & 2{,}653 \end{pmatrix}$$

Closest transversally isotropic elasticity tensor to ensemble averaged effective elasticity tensor (1ET)

$$\begin{pmatrix} 8{,}458 & 3{,}695 & 4{,}263 & 0 & 0 & 0 \\ 3{,}695 & 8{,}458 & 4{,}263 & 0 & 0 & 0 \\ 4{,}263 & 4{,}263 & 11{,}967 & 0 & 0 & 0 \\ 0 & 0 & 0 & 2{,}929 & 0 & 0 \\ 0 & 0 & 0 & 0 & 2{,}929 & 0 \\ 0 & 0 & 0 & 0 & 0 & 2{,}382 \end{pmatrix}$$

Ranges of microfields in the matrix

The predicted ranges of the local stress fields for configuration IIe, pseudo-voids at the grains' triple points, are presented in Table 30.

Table 30 Maximum and minimum values of integration point von Mises and first principal stresses predicted by one-step (configuration IIe/ 1) and two-step (configuration IIe/2) models with quasi-voids at triple points of grains

Load case	Variable	Min/Max one-step	Min/Max two-step
σ_{11}	σ_{vm}	0,20/6,43	0,42/3,99
	σ_I	-0,55/6,95	-0,16/4,51
σ_{22}	σ_{vm}	0,25/6,92	0,50/3,93
	σ_I	-0,20/7,48	-0,11/4,40
σ_{33}	σ_{vm}	0,67/3,32	1,33/1,33
	σ_I	0,37/3,00	1,33/1,33
τ_{12}	σ_{vm}	0,07/8,35	0,28/5,42
	σ_I	-1,93/9,52	-0,56/6,35
τ_{13}	σ_{vm}	0,04/11,63	0,04/5,03
	σ_I	-0,32/7,98	0,01/2,92
τ_{23}	σ_{vm}	0,06/13,41	0,15/5,60
	σ_I	-0,10/9,98	0,10/3,22

Compared to the "inhomogeneities at the grain centers" case, a tendency towards higher stress maxima is present for the one-step models, concentration factors in excess of ten being reached for the shear load cases. Clear differences in the stress ranges are evident for the σ_{11} and σ_{22} load cases, as well as the τ_{12} and τ_{13} load cases, respectively. These do not necessarily imply the presence of meshing effects: although the 0° and 90° loading directions give the same effective response in hexagonal two-phase arrangements, the microfields only have to be identical only in terms of their phase averages. Accordingly, it is not clear to what extent the differences in the stress ranges predicted for the Ie and IIe configurations are discretization effects and how much they are consequences of the larger size of grains compared to the pseudo-voids in the latter set of geometries.

4.6.3. Effective moduli

Table 31 lists the effective moduli corresponding to the transversally isotropic tensors closest to the effective elasticity tensors obtained by one-step and two-step procedures (Ie/1ET, IIe/1ET, Ie/2ET, IIe/2ET), and to the one-step and two-step models using the isotropized matrix behavior (Ie/2EI, IIe/2EI), plus the Hashin-Shtrikman upper bounds for isotropized matrix behavior (HSH/EI). Because the elastic contrast approaches zero, the lower bounds form most moduli become trivial and are not given.

Table 31 Effective, transversally isotropic moduli predicted for models with quasi-voids

	E_A	E_T	ν_A	ν_T	G_A	G_T
HSH/EI	9,744	6,812	0,342	---	2,904	2,578
Ie/1ET	9,156	6,385	0,345	0,321	3,023	2,416
IIe/1ET	8,977	6,257	0,351	0,314	2,929	2,382
Ie/2ET	9,310	6,698	0,349	0,303	2,947	2,570
IIe/2ET	9,310	6,638	0,349	0,229	2,920	2,555
Ie/2EI	9,744	6,707	0,342	0,316	2,905	2,549
IIe/2EI	9,744	6,645	0,342	0,312	2,879	2,533

Because material combination (e) is the most “extreme” among the ones covered here, it gives rise to the highest differences between one-step and two-step predictions, which approach or exceed 5% for all transverse moduli and reach 7% for the transverse shear moduli. Among the cases considered here, it is also the only one for which differences in the one-step and two-step predictions for the axial Young’s modulus exceed 1%.

4.7. Plots of microfields

This section presents plots of the microfields predicted by single-step homogenization for selected configurations. To keep the number of plots at a manageable level, stress distributions are presented only for one set of grain orientation distributions. Due to the difficulties in scaling the displacements and fringe levels for these load cases in such a way that they are both consistent and readable for all configurations considered, no attempt has been made to achieve such consistency.

Figure 4.1 shows the von Mises effective stresses in matrix and T-300 carbon fibers (configuration Ia) obtained for one of the models under transverse uniaxial tensile loading in the horizontal direction. Due to their higher in-plane stiffness the fibers show elevated levels of effective stress. Stress patterns in the matrix are clearly influenced by local material orientations and allow discerning the individual grains. The fibers show somewhat inhomogeneous stress fields, with the fluctuations reflecting material orientation in the grains rather than the hexagonal fiber arrangement. Similar remarks hold for Figure 4.2, which presents the distributions of the von Mises stresses under transverse uniaxial tension in the vertical direction. Due to the combination of high heterogeneity and relatively small numbers of grains in the models, the purely normal macroscopic stress leads to some clearly visible shear deformations in addition to the dominant normal deformations in these matrix dominated modes. No such effects are evident in Figure 4.3, which shows the straightforward microstress response to longitudinal normal loading. This behavior is due, on the one hand, to the orientation of the fibers and, on the other hand, to their very high stiffness in the axial direction. Local fluctuations of the von Mises stress in this fiber dominated mode, although present, are not of sufficient magnitude to be resolved at the fringe scaling shown.

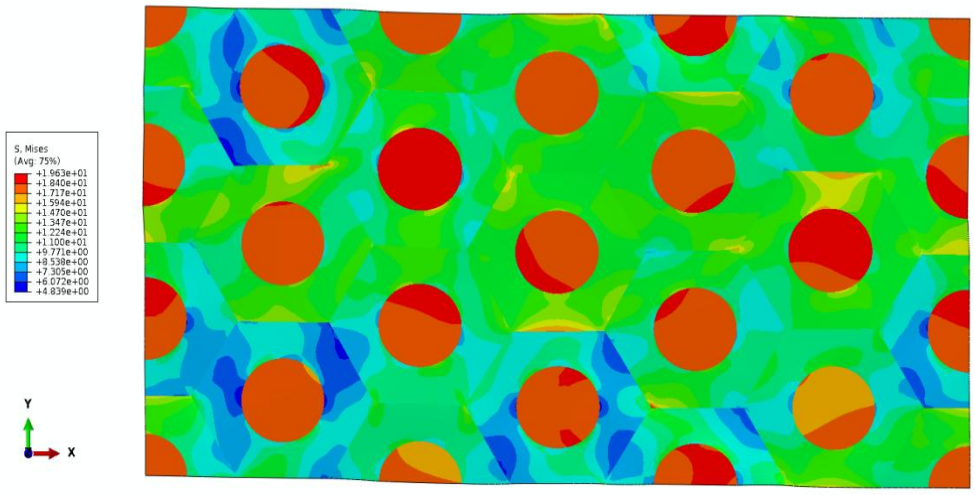

Figure 4.1 Distribution of von Mises stress predicted for a model employingT-300 carbon fibers in the centers of the matrix grains (configuration Ia/1) subjected to transverse uniaxial tensile loading in the *x*-direction.

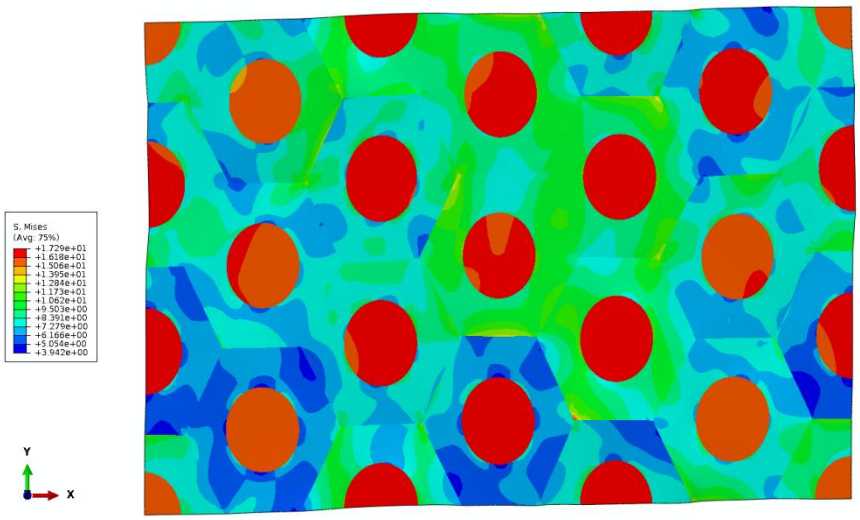

Figure 4.2Distribution of von Mises stress predicted for a model employing T-300 carbon fibers in the centers of the matrix grains (configuration Ia/1) subjected to transverse uniaxial tensile loading in the *y*-direction.

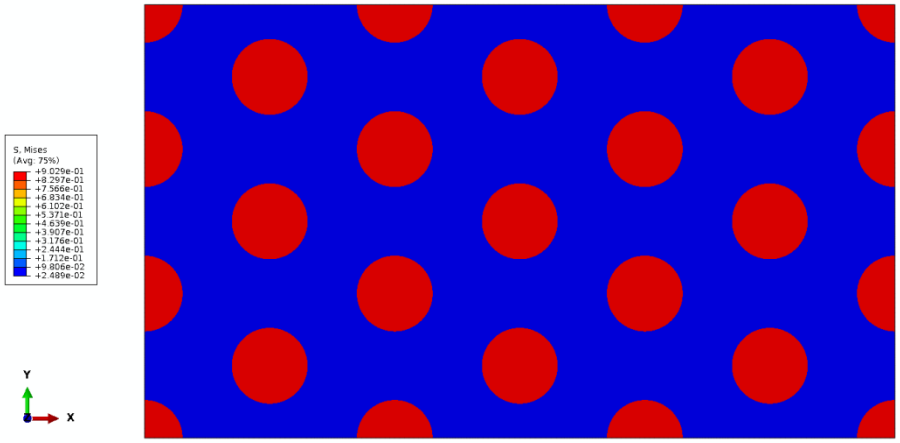

Figure 4.3Distribution of von Mises stress predicted for a model employing T-300 carbon fibers in the centers of the matrix grains (configuration Ia/1) subjected to longitudinal uniaxial tensile loading in the *z*-direction.

The relatively small difference in elastic in-plane shear stiffness between the constituents leads to fairly similar levels of the von Mises stress in matrix and fibers under transverse shear loading for the present combination of phase properties, see Figure 4.4.

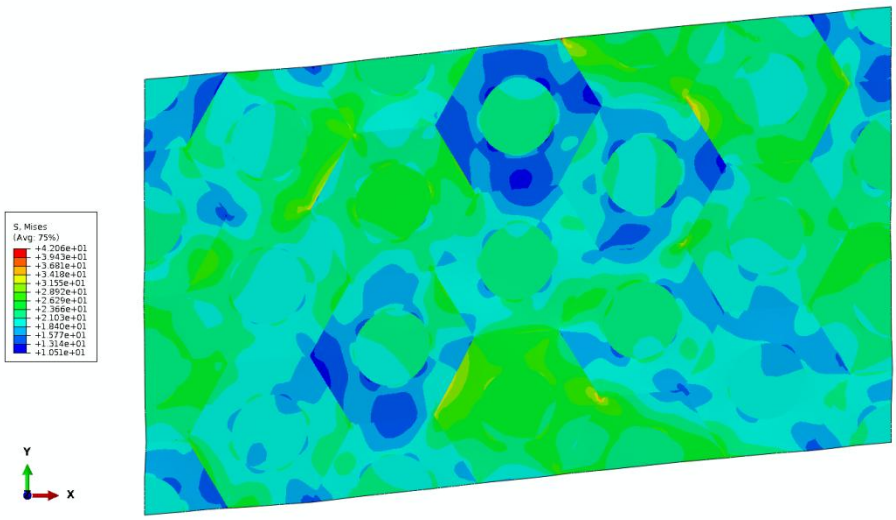

Figure 4.4 Distribution of von Mises stress predicted for a model employing T-300 carbon fibers in the centers of the matrix grains (configuration Ia/1) subjected to transverse shear loading in the *x*-*y*-plane.

For the two longitudinal shear load cases, shown in figures Figure 4.5 and Figure 4.6, the magnitudes of the von Mises stresses are considerably higher in the T-300 fibers than in the matrix. Here it is interesting to note that some orientations of the matrix crystallites lead to very low local stress levels.

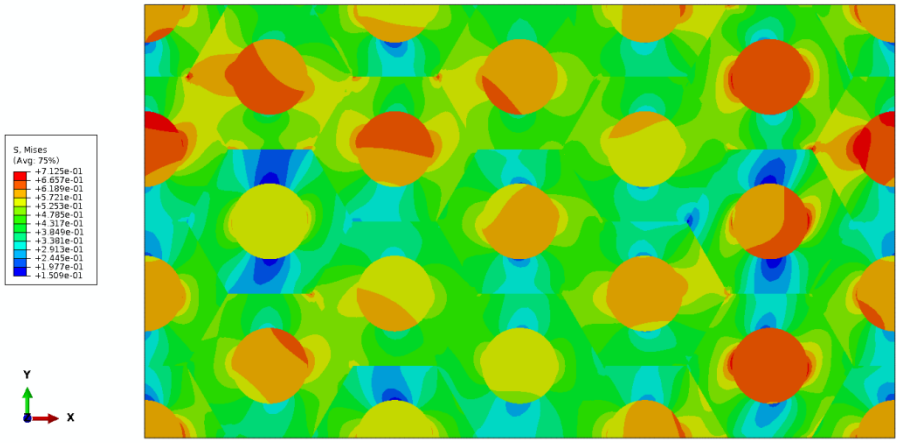

Figure 4.5 Distribution of von Mises stress predicted for a model employing T-300 carbon fibers in the centers of the matrix grains (configuration Ia/1) subjected to longitudinal shear loading in the *y*-*z*-plane.

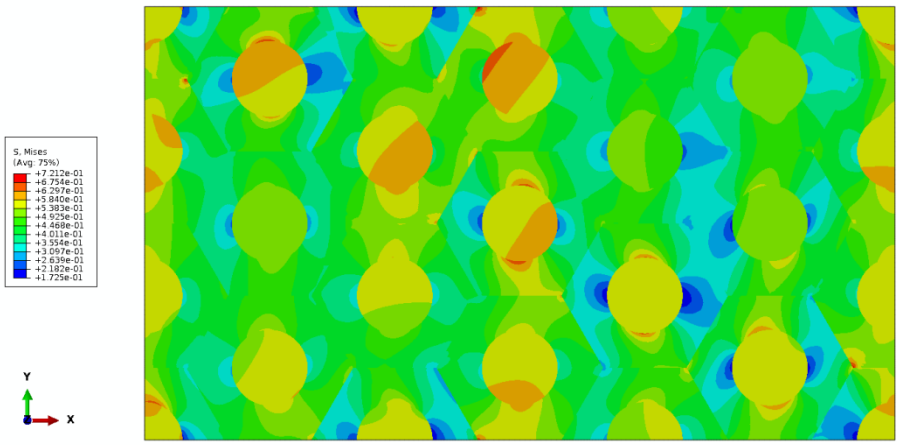

Figure 4.6 Distribution of von Mises stress predicted for a model employing T-300 carbon fibers in the centers of the matrix grains (configuration Ia/1) subjected to longitudinal shear loading in the *x*-*z*-plane.

Whereas figuresFigure 4.1 to Figure 4.6 provide plots of the predicted distributions of the von Mises equivalent stress for all six linear elastic load cases for configuration Ia, i.e., carbon fibers positioned at the centers of the grains, only the stress fields corresponding to transverse normal loading are presented in the following figures for some of the other configurations covered by the present work.

Figure 4.7 displays the distributions of the von Mises stress under transverse tensile loading pertaining to configuration IIa, T-300 carbon fibers positioned at the triple points of the matrix grains. The results are broadly comparable to those shown in figures Figure 4.1 and Figure 4.2. The differences in the stress levels between the individual inhomogeneities appear to be somewhat more pronounced and the stress distributions in the grains less diffuse, however.

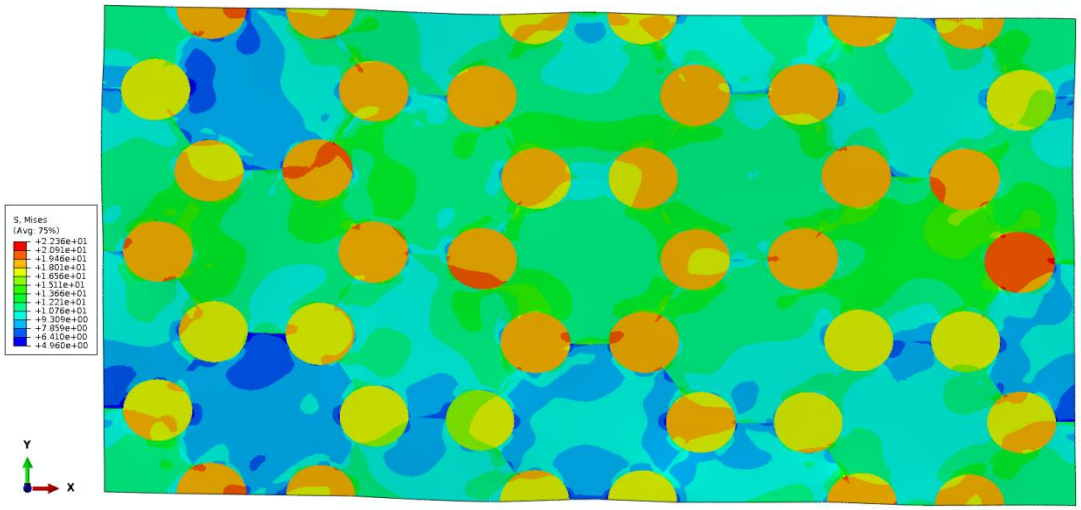

Figure 4.7 Distribution of von Mises stress predicted for a model employing T-300 carbon fibers at the triple points of the matrix grains (configuration IIa/1) subjected to transverse uniaxial tensile loading in the *x*-direction.

Figure 4.8, which pertains to configuration IIb and thus to P-100 carbon fibers at the triple points, in contrast, shows a qualitatively different picture. Due to the small transverse Young's modulus of these fibers, compare table 4, the elastic contrast under transverse shear is low and the equivalent stresses in fibers and matrix do not differ strongly.

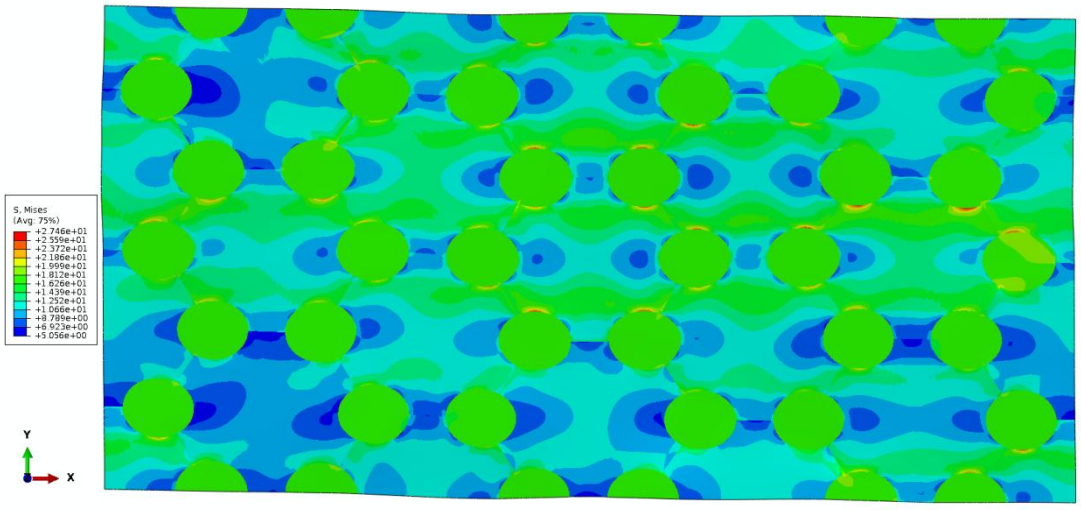

Figure 4.8 Distribution of von Mises stress predicted for a model employing P-100 carbon fibers at the triple points of the matrix grains (configuration IIb/1) subjected to transverse uniaxial tensile loading in the *x*-direction.

The Nextel 312 fibers are isotropic and, accordingly, show a much higher Young's modulus in the transverse plane than does the matrix. Consequently, Figure 4.9, shows a pattern characteristic for a high contrast situation which, in fact, is fairly similar to Figure 4.7.

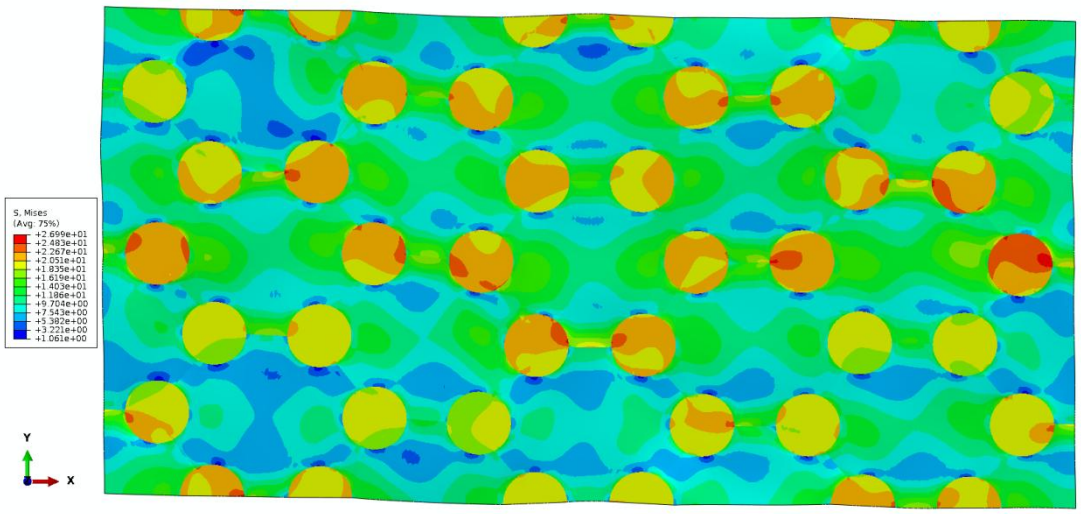

Figure 4.9 Distribution of von Mises stress predicted for a model employing Nextel 312 oxidic fibers at the triple points of the matrix grains (configuration IIc/1) subjected to transverse uniaxial tensile loading in the *x*-direction.

Figures Figure 4.10 and Figure 4.11 depict situations in which the inhomogeneities are either considerably more compliant (configuration IId) than the matrix or show so little stiffness that their behavior approaches that of pores (configuration IIe), respectively. As a consequence, the stresses in the inhomogeneities are predicted to be very low (Figure 4.10) or vanish entirely (Figure 4.11), the distributions of the equivalent stresses in the matrix being quite similar in the two cases. As expected the maximum stresses in the matrix occur at the boundaries of the voids. In Figure 4.11 the deformed shapes of the pseudo-voids can be seen to deviate considerable from the circles being present in the undeformed configuration.

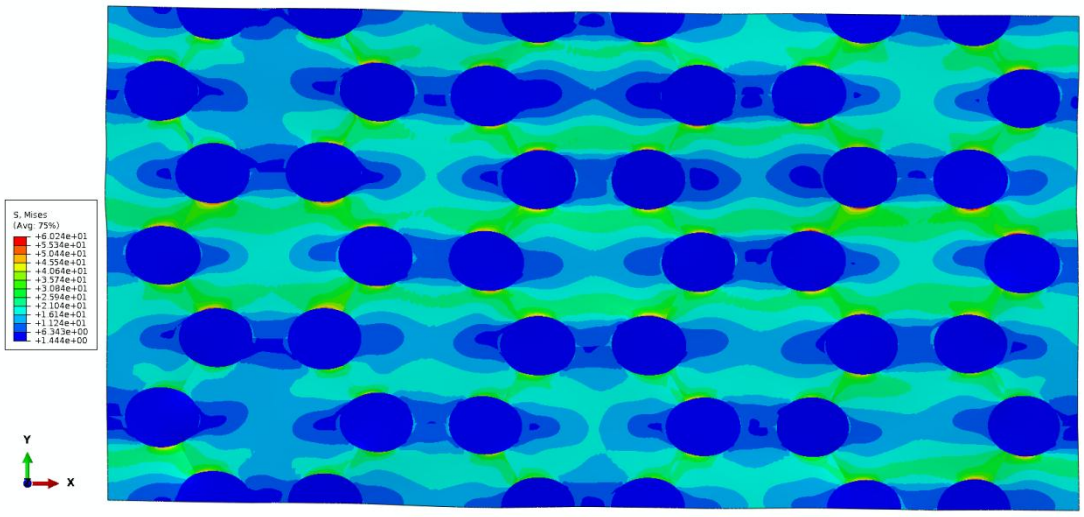

Figure 4.10 Distribution of von Mises stress predicted for a model employing hypothetical compliant inhomogeneities at the triple points of the matrix grains (configuration IId/1) subjected to transverse uniaxial tensile loading in the *x*-direction.

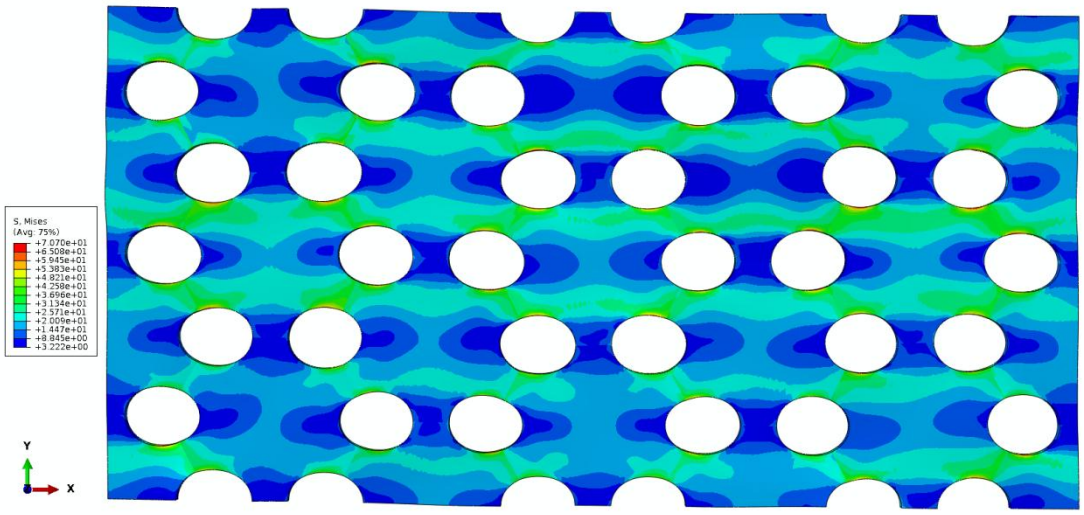

Figure 4.11 Distribution of von Mises stress predicted for a model containing quasi-pores at the triple points of the matrix grains (configuration IIe/1) subjected to transverse uniaxial tensile loading in the *x*-direction.

FiguresFigure 4.12 and Figure 4.13 display the distributions of the von Mises stress predicted for T-300 fibers embedded in the homogenized, ensemble averaged matrix (configuration Ia/0E) and in the homogenized, ensemble averaged and isotropized matrix (configuration Ia/0EI). Due to the absence of perturbations from the

inhomogeneous matrix grains, the highly regular pattern characteristic of hexagonal arrangements of fibers in an isotropic matrix is obtained, with relatively small stress fluctuations in the matrix and even smaller ones in the fibers. Effects of isotropization cannot be resolved within the fringe levels used here. The absence of grain-level perturbations also leads to a perfectly rectangular deformed shape of the unit cell. The stress fields predicted for fibers at the positions of the triple points that are embedded in the homogenized, ensemble averaged matrix (configuration Ib/0E) are presented in Figure 4.14. Again, the perfect regularity and small amplitudes of the field fluctuations as well as the rectangular shape of the deformed unit cell are evident.

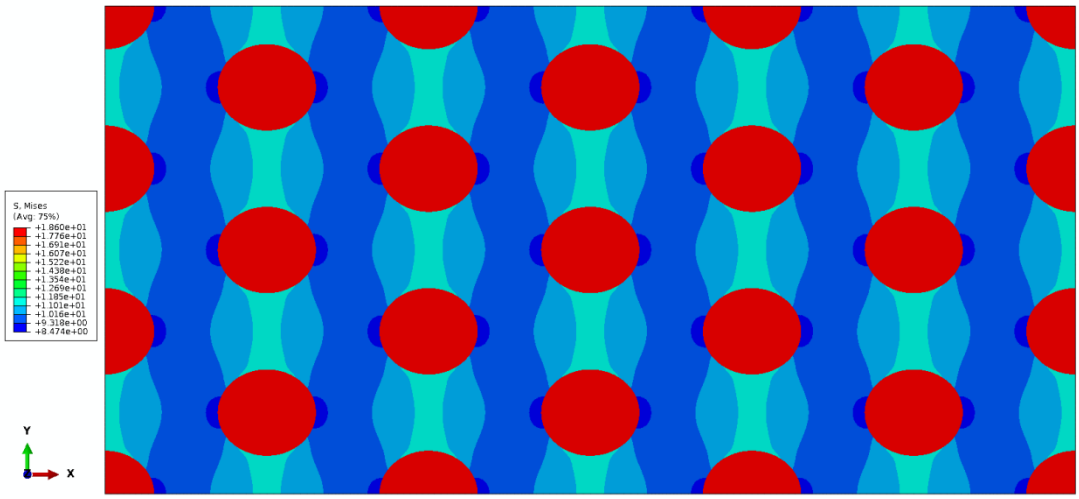

Figure 4.12 Distribution of von Mises stress predicted for a model employing T-300 carbon fibers embedded in the homogenized matrix material at the positions of the grain centers (configuration Ia/0E) subjected to transverse uniaxial tensile loading in the *x*-direction.

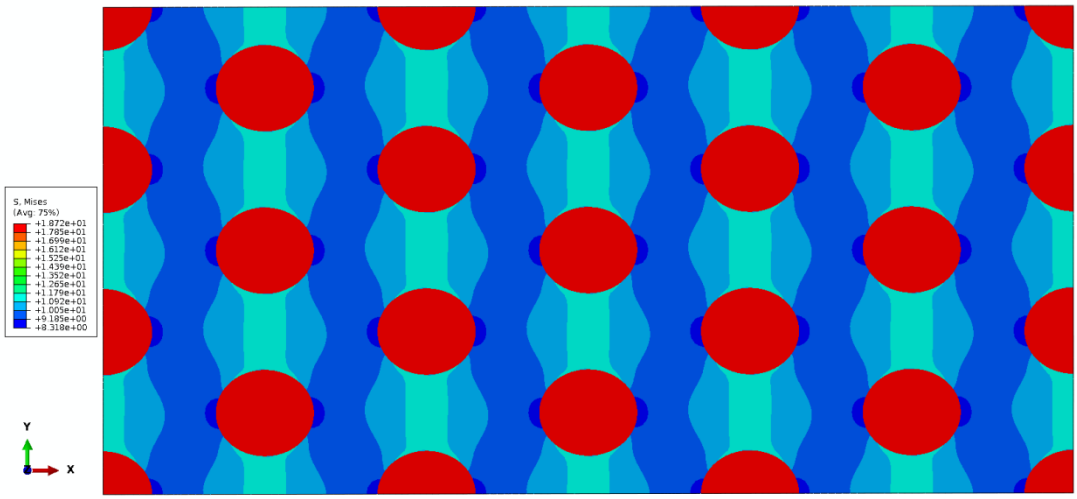

Figure 4.13 Distribution of von Mises stress predicted for a model employing T-300 carbon fibers embedded in the homogenized matrix material at the positions of the grain centers (configuration Ia/0EI) subjected to transverse uniaxial tensile loading in the *x*-direction.

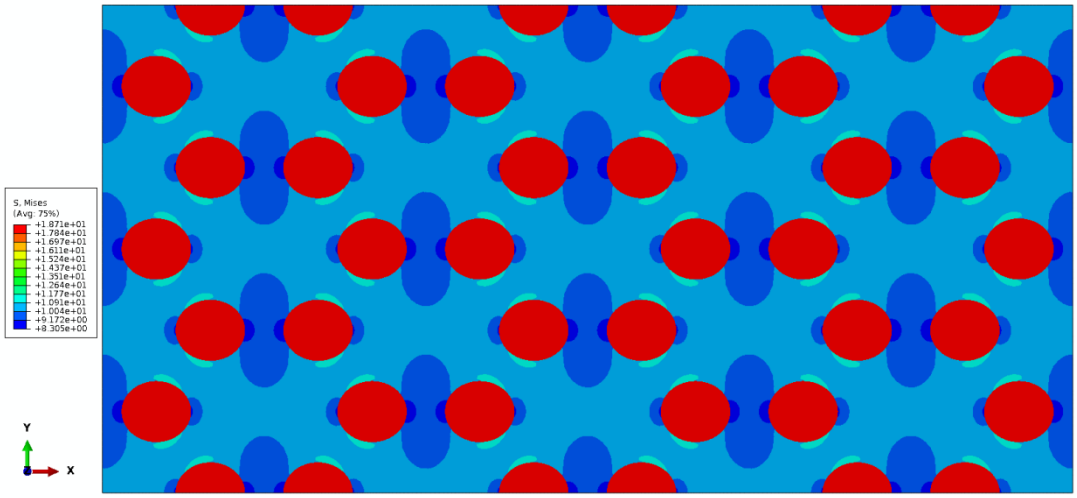

Figure 4.14 Distribution of von Mises stress predicted for a model employing T-300 carbon fibers embedded in the homogenized matrix material at the positions of the triple points (configuration IIa/0E) subjected to transverse uniaxial tensile loading in the *x*-direction.

Finally, Figure 4.15 shows results obtained for the unreinforced, inhomogeneous matrix (configuration 0) subjected to transverse tensile loading. The stress distributions are dominated by the effects of the different stiffnesses caused by the different orientations of the cubic material in the individual grains, with the highest stresses occurring at grain boundaries and triple points.

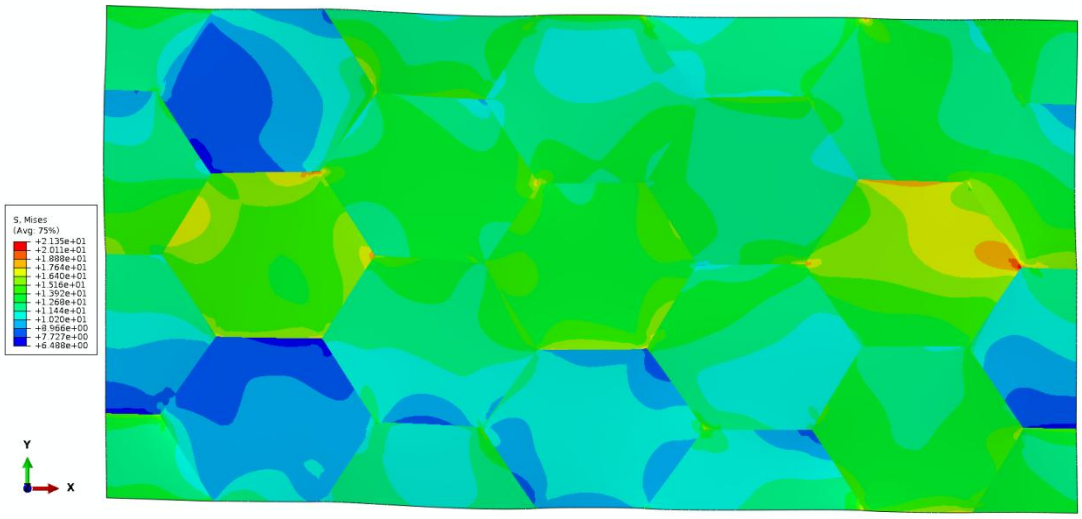

Figure 4.15 Distribution of von Mises stress predicted for a model consisting of matrix grains only (configuration 0) subjected to transverse uniaxial tensile loading in the *x*-direction.

Chapter 5
Conclusions

The main goal of this present work was to present the analysis of differences in elastic responses obtained by periodic homogenization, i.e., differences between one-step homogenization and two-step homogenization procedures applied to inhomogeneities - continuous, aligned fibers - in a matrix with grain structure, where the matrix grains and the fibers were chosen to show similar length scales. Such configurations were studied for five different elastic behaviors of the inhomogeneities, ranging from stiffer to more compliant behavior. In addition, the ranges of the von Mises and the first principal stresses were evaluated for two homogenization runs, which show the stiffest and most compliant fibers.

The relative differences between the single-step and two-step macroscopic elasticity tensor results for **configuration Ia** (T-300 carbon fibers) are less than 6% for the tensor elements connected to transversally isotropic behavior. The effective elasticity tensors of **configuration Ib** (P-100 carbon fibers) are, qualitatively, quite similar to the predictions obtained for **configuration Ia**. The Nextel fibers (**configuration Ic**) lead to a less anisotropic behavior than the carbon fibers, the relative difference between one-step and two-step homogenization exceeding 6% in the axial shear component. The hypothetical compliant inhomogeneities (**configuration Id**) lead to an increased influence of the matrix behavior on the overall elastic response, the maximum relative difference between the two sets of homogenization results reaches 8%, and the components of the one-step tensor are smaller than the ones of the two-step tensor. For **configuration Ie** (which approximates voids in the matrix), the maximum difference between the two homogenization strategies exceeds 9%.

Configuration IIa macroscopic elasticity tensors agree well with the ones given in **configuration Ia**. This agreement is closer for the results of two-step homogenization than for the one-step predictions. The elastic tensors of the unit cells for **configuration**

IIb compared to the ones obtained for the **Ib** models show a trend towards lower stiffness for the former model. The results obtained for the **configuration IIc** geometry (with the Nextel fibers) show a qualitatively very similar behavior to the predictions given in **Ic** case, although with slightly different numerical values. The effective elasticity tensors for **configuration IId** show qualitatively similar behavior to **configuration Id**. Differences in the values of the effective elasticity tensor components for **IIe** case compared to the **Ie** case are evident, although not very big.

The data of the ranges of the predicted von Mises stresses and first principal stresses in fiber and matrix for both **configuration Ia** and **configuration Ie** shows a clear tendency to be much larger for one-step than for two-step homogenization. The inhomogeneous matrix behavior accounted for in the one-step models induces fluctuations in the stress fields in the fibers.

These values do not differ considerably for the two positions of the fibers considered, especially the results obtained by two-step homogenization. As in the case of **configuration Ia**, the one-step models for the **IIa** case predict higher fluctuations of the local fields. The predicted ranges of the local stress fields for **configuration IIe**, compared to the **Ie** case, present the same tendency as material combination (a).

Effective moduli evaluated with the isotropized matrix behavior either fall within the corresponding Hashin-Shtrikman bounds or closely approach the lower bound (composites reinforced by stiff fibers) or the upper bound (composites containing inhomogeneities more compliant than the matrix), which is, of course, the expected behavior The moduli corresponding to the closest transversally isotropic tensors to the one-step and two-step results obtained for the inhomogeneous matrix, however, mostly fall outside the bounds, the largest relative difference being 2,2%. All such predictions for the overall axial Young's moduli lie below the Hashin-Shtrikman bounds obtained with the isotropized matrix. The macroscopic transverse Young's and shear moduli obtained with the one-step models lie below the corresponding lower Hashin-Shtrikman bounds, whereas those extracted from the two-step models are above the upper bounds.

The agreement between the results of the comparison between the elastic moduli corresponding to the transversally isotropic tensors closest to the one-step and two-step obtained with the **Ib** and the **IIb** geometries is not quite as close as for the material

combination (a), differences exceed 3% in the cases of the transverse Young's and shear moduli. The two-step results obtained with the isotropized matrix behavior show more marked violations of the Hashin-Shtrikman bounds.

The relative difference for **configuration IIc** between the one-step and two-step results reaches 5% for the axial shear moduli. The numerical results for isotropized matrix behavior all fall within the Hashin-Shtrikman bounds.

As to material combination (d), the Hashin-Shtrikman bounds are rather slack, and the numerical predictions obtained with the isotropized matrix behavior are close to the upper bounds. The predictions for the transverse Young's and shear moduli are lower, the relative differences being of the order 5%. Interestingly, the differences in the effective axial moduli are much smaller.

Finally, material combination (e), which approaches one of the limiting cases in terms of elastic contrast, gives rise to the highest differences between unit cells and bounds, which approach 5% for the transverse Young's moduli and reach 7% for the transverse shear moduli. It is also the only case for which differences between the one-step and two-step predictions for the axial Young's modulus exceed 1%.

As to future lines of investigation, future work could be based on more complex geometries, such as particle composites instead of the fiber reinforcement used in this work. Different material symmetries of the matrix grains could be used and non-linear material behavior, such as crystal plasticity of the matrix grains, might be studied.

Appendix A
Identifiers of Results

In this chapter, the notation used for identifying individual results is presented and explained, in order to facilitate references to each configuration and material used and to each procedure and run carried out. At the end of the chapter two examples for the use of the notation are given.

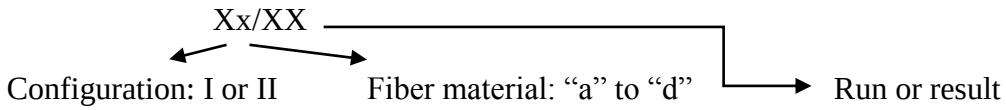

Configurations:	
Configuration I:	Matrix formed of columnar hexahedral grains with inhomogeneities (fibers) set in the centers of the matrix grains.
Configuration II:	Matrix formed of columnar hexahedral grains with inhomogeneities (fibers) set at the triple points of the grains.

Fiber materials:
a: T-300 carbon fibers.
b: P-100 carbon fibers.
c: Nextel 312 oxidic fibers
d:hypothetical compliant inhomogeneities
e: quasi-pores.

Homogenization runs (models):	**Results (types):**
0: inhomogeneous matrix formed of grains alone. 20 runs. **1**: inhomogeneous matrix with fibers (single step homogenization). 20 runs per fiber material. **2**: uniform, homogenized matrix with fibers (two-step homogenization). 1 run per fiber material. **2I**: isotropized matrix with fibers (two-step homogenization). 1 run per fiber material.	**0E**: ensemble averaged homogenized elasticity tensor for matrix. **1E**: ensemble averaged single-step homogenized elasticity tensor for composite. **2E**: elasticity tensor obtained by two-step homogenization using ensemble averaged, homogenized **0E** matrix. **2EI**: elasticity tensor obtained by two-step homogenization using closest isotropic elastic behavior to ensemble averaged, homogenized **0E** matrix.

Here E represents the ensemble averaged homogenized elasticity tensor and EI the tensor obtained by isotropizing this result, i.e., by finding the closest transversally isotropic elasticity tensor to the ensemble averaged homogenized tensor.

The 20 sets of grain orientations explained in section 3.4 give rise to 20 homogenization runs, as defined at the start of Chapter 3. These 20 runs pertain to the inhomogeneous matrix without fibers and give rise to 20 homogenized elasticity tensors, denoted as **Model 0**. The ensemble average of these 20 homogenized tensors is called the **Type 0E** result. This ensemble averaged homogenized elasticity tensor which forms the basis for **Model 2** runs.

Analyzing the same 20 sets of grain orientations, but now with fibers embedded in the grains, gives rise to 20 homogenization runs per configuration and per fiber material, (**a**) to (**e**). The resulting ten sets of 20 elasticity tensors each are referred to as **Model 1**. From each of the ten sets of data of 20 runs each, one ensemble averaged single-step homogenized elasticity tensor is obtained, constituting the **Type 1E** results. For distinguishing these ten sets of data the notation **Xa/1E** to **Xe/1E** is used, where the

letters **a** to **e** stand for the fiber materials, **X**can take the values **I** or **II**, depending on the position of the fibers within the matrix grains (at the grain centers or the triple points).

Model 2 runs employ the homogenized matrix **0E**, embed the fibers in it and then carry out the second homogenization step. The ten effective elasticity tensors resulting from this two-step homogenization procedure are the **Type 2E**results. In this case the notation is **Xa/2E** to **Xe/2E**, for fiber materials (**a**) to (**e**), with **X** again standing for configurations **I** or **II**.

Type 2EI results are obtained in analogy to the **Type 2E** results, but by employing the "isotropized" ensemble averaged homogenized matrix behavior rather than the ensemble averaged homogenized tensor. Again, results are given for the five types fibers, (**a**) to (**e**), and the two available configurations, **I** and **II**.

Finally, two examples of this notation are given.

Results marked as **Ia/1E**can be decoded as pertaining to **Configuration I**(matrix formed of columnar hexahedral grains with inhomogeneities (fibers) set in the center of the matrix grains), fiber material **a**(T-300 carbon fibers) and result type **1E**(ensemble averaged single-step homogenized elasticity tensor of the composite).

Results with the designator **IIc/2EI**describe**Configuration II** (matrix formed of columnar hexahedral grains with inhomogeneities (fibers) set at the triple points of the grains), fiber material **c**(Nextel 312 oxidic fibers) and result type **2EI** (second step of two-step a homogenization model using the closest isotropic elasticity tensor obtained from the **0E** ensemble averaged, homogenized matrix data).

References

[1] D. Miracle and S. Donaldson, Introduction to Composites, ASM International, Metals Park, OH, 2001.

[2] J. Vinson and R. Sierakowski, The Behavior or Structures Composed of Composite Materials, Dordrecht: Kluwer Academic Publishers, 2002.

[3] Z. Hashin, Theory of Mechanical Behavior of Heterogeneous Media, Philadelphia, P.A.: University of Pennsylvania, 1963.

[4] M. Hyer, Stress Analysis of Fiber-Reinforced Composite Materials, New York, N.Y.: McGraw-Hill Higher Education, 1998.

[5] J. Zeman, Analysis of Composite Materials with Random Microstructure, Prague, Czech Republic: Klokner Institute, Czech Technical University in Prague, 2003.

[6] 3DS, ABAQUS/Standard User's Manual v6.12, Providence, RI, USA: Dassault Systèmes Simulia Corp..

[7] PSF, Python Software Foundation, Beaverton, OR, USA.

[8] D. Pahr, Medtool 3.6 for LINUX, Vienna, Austria: Institute of Lightweight Design and Structural Biomechanics. Vienna University of Technology, 2006-2013.

[9] 3DS, ABAQUS/Analysis Theory Manual v6.12, Providence, RI, USA: Dassault Systèmes Simulia Corp..

[10] H. Böhm, A short introduction to basic aspects of continuum micromechanics., Vienna, Austria: Institute of Lightweight Design and Structural Biomechanics. Vienna University of Technology, 1998, 2013.

[11] R. Hill, Elastic properties of reinforced solids: Some theoretical principles, J.Mech.Phys.Sol.; 11:357–372, 1963.

[12] S. Forest, G. Cailletaud, D. Jeulin, F. Feyel, I. Galliet, V. Mounoury and S. Quilici, Introduction au calcul de microstructures, Méc.Indust., 3:439–456, 2002.

[13] Z. Hashin, Analysis of composite materials - A survey., J.Appl.Mech., 50:481–505, 1983.

[14] R. Hill, Theory of mechanical properties of fibre-strengthened materials: I. Elastic behavior, J.Mech.Phys.Sol., 12:199-212, 1964.

[15] G. Milton, The Theory of Composites., Cambridge: Cambridge University Press, 2002.

[16] J. Nye., Physical Properties of Crystals, Their Representation by Tensors and Matrices, Clarendon, Oxford, 1957.

[17] J. Michel, H. Moulinec and P. Suquet, Effective properties of composite materials with periodic microstructure: A computational approach., Comput.Meth.Appl.Mech.Engng., 172:109–143, 1999.

[18] J. Michel, H. Moulinec and P. Suquet, Composites à microstructure périodique, Paris: In M. Bornert, T. Bretheau, and P. Gilormini, editors, Homogénéisation en mécanique des matériaux 1. Matériaux aléatoires élastiques et milieux périodiques, pages 57–94, Editions Hermès, 2001.

[19] H. Böhm and D. Pahr, . Assessment of mixed uniform boundary conditions for predicting the mechanical behavior of elastic and inelastic discontinuously reinforced composites., Comput.Model.Engng.Sci., 34:117–136, 2008.

[20] F. El Houdaigui, S. Forest, A. Gourgues and D. Jeulin, On the size of the representative volume element for isotropic elastic copper, Dordrecht: In Y.L. Bai and Q.S. Zheng, editors, IUTAM Symposium on Mechanical Behavior and Micro-Mechanics of Nanostructured Materials, pages 171–180, 2007.

[21] D. Adams and D. Crane, Finite element micromechanical analysis of a unidirectional composite including longitudinal shear loading., Comput.Struct., 18:1153–1165, 1984.

[22] N. Sørensen, A planar type analysis for the elastic-plastic behaviour of continuous fibre-reinforced metal-matrix composites under longitudinal shearing and combined loading., Int.J.Sol.Struct., 29:867–877, 1992.

[23] H. Pettermann and S. Suresh, A comprehensive unit cell model: A study of coupled effects in piezoelectric 1–3 composites., Int.J.Sol.Struct., 37:5447–5464, 2000.

[24] H. Böhm and F. Rammerstorfer, Fiber arrangement effects on the microscale stresses of continuously reinforced MMCs., Kluwer Academic Publisher: In R. Pyrz, editor, Microstructure–Property Interactionsin Composite Materials, pages 51–62, Dordrecht, 1995.

[25] T. Nakamura and S. Suresh, Effects of thermal residual stresses and fiber packing on deformation of metal-matrix composites, Acta metall.mater., 41:1665–1681, 1993.

[26] H. Moulinec and P. Suquet, A numerical method for computing the overall response ofnonlinear composites with complex microstructure., Comput.Meth.Appl.Mech.Engng.,157:69–94, 1997.

[27] A. Gusev, P. Hine and I. Ward, Fiber packing and elastic properties of a transversely random unidirectional glass/epoxy composite., Compos.Sci.Technol., 60:535–541, 2000.

[28] J. Zeman and M. Ŝejnoha, From random microstructures to representative volume elements., Modell.Simul.Mater.Sci.Engng., 15:325–S335, 2007.

[29] A. N. Norris, "The isotropic material closest to a given anisotropic material," *Journal of Mechanics of Materials and Structures*, vol. 1, no. 2, pp. 223-228, 2006.

[30] M. Moakher, "On the averaging of symmetric positive-definite tensors," *Journal of Elasticity*, vol. 82, pp. 273-296, 2006.

[31] V. Arsigny, P. Fillard, X. Pennec and N. Ayache, "Fast and simple calculus on the tensors in the Log-Euclidean framework," *8th Int. Conf. on Medical Image Computing and Computer-Assisted Intervention (MICCAI)*, Vols. I (Eds. J.S. Duncan, G.Gerig), pp. 115-122, Springer-Verlag, Heidelberg, 2005.

[32] D. Gazis, I. Tadjbakhsh and R. Toupin, "The elastic tensor of given symmetry nearest to an anisotropic elastic tensor," *Acta Crystallographica*, vol. 16, pp. 917-922, 1963.

[33] F. Cavallini, "The best isotropic approximation of an anisotropic Hooke's law," *Bolletino di Geofisica Teorica ed Applicata,* vol. 16, pp. 1-18, 1999.

[34] M. Moakher and A. Norris, "The closest elastic tensor of arbitrary symmetry to an elastic tensor of lower symmetry," *Journal of Elasticity,* vol. 85, pp. 215-263, 2006.

[35] M. Bornert, Morphologiemicrostructurale et comportementmécanique; caractérisationséxperimentales, approches par bornes et estimations autocohérentesgéneralisées, Doctoral thesis, Ecole des Ponts et Chaussées, Paris, 1996.

[36] Z. Hashin, "Analysis of composite materials - A survey.," *J.Appl.Mech.,* no. 50, p. 481–505, 1983.

[37] Z. Hashin and S. Shtrikman, "On Some Variational Principles in Anisotropic and Nonhomogeneous Elasticity," *J.Mech.Phys.Sol.,* no. 10, pp. 335-342, 1962.